DEVELOPMENT OF MAGNETIC LABELS FOR MAGNETIC IMMUNOASSAYS: TOWARDS MULTIPLEXED DETECTION OF PANCREATIC CANCER MARKERS USING GIANT-MAGNETORESISTIVE SENSOR

by

Jooneon Park

A dissertation submitted to the faculty of
The University of Utah
in partial fulfillment of the requirements for the degree of

Doctor of Philosophy

Department of Chemical Engineering

The University of Utah

August 2017

The University of Utah Graduate School

STATEMENT OF DISSERTATION APPROVAL

The dissertation of **Jooneon Park**

has been approved by the following supervisory committee members:

Marc D. Porter	, Chair	**05/23/2017** Date Approved
Edward Trujillo	, Member	**05/23/2017** Date Approved
Mikhail Skliar	, Member	**05/23/2017** Date Approved
Swomitra Mohanty	, Member	**05/23/2017** Date Approved
Ling Zang	, Member	**05/23/2017** Date Approved

and by **Milind Deo** , Chair/Dean of

the Department/College/School of **Chemical Engineering**

and by David Kieda, Dean of The Graduate School.

ABSTRACT

For the last two decades, our research group has focused on developing nanotechnology-based diagnostic platforms for disease detection. One of our main diagnostic platforms is magnetic immunoassay based on giant magnetoresistance (GMR) readout. Due to high sensitivity and rapid data retrieval of the GMR readout, GMR-based immunoassays enable a low level of rapid detection of disease markers and have the potential for multiplexing (*i.e.*, detecting multiple analytes simultaneously). As part of an effort to develop a GMR-based multiplexing test, this dissertation focuses on the development of magnetic labels for use in magnetic immunoassays. Thus, the body of this dissertation includes: (1) synthesis of magnetic nanoparticles (MNPs) with high magnetic moments; (2) emulsion-based bottom-up assembly approach to design new magnetic materials; (3) surface functionalization of MNPs and biomolecule conjugation for use as magnetic labels; and (4) development of magnetic immunoassays for the detection of potential pancreatic cancer markers using our GMR sensor.

Firstly, silica encapsulation of ferrimagnetic nanocubes with high magnetic moments (***m***) is described. These results not only demonstrate the synthesis of high-***m*** MNPs uniform in size and shape, but also stabilization of the MNPs with high ***m*** via silica coating. Secondly, the fabrication of colloidal assembly of MNPs is discussed with the investigation of their magnetic properties. This chapter shows that assembly of MNPs into

a larger magnetic bead can not only change their magnetic properties, but also be an efficient way to design new materials for specific applications. Next, surface coating and biomolecule conjugation of the colloidally assembled magnetic beads are investigated to prepare magnetic labels. These results indicate that magnetic labels based on colloidally assembled magnetic beads are superior to commercially available magnetic labels. The last chapter is focused on the development of magnetic immunoassays for the simultaneous detection of pancreatic cancer markers based on our magnetic label and GMR sensor. The results show the potential of a GMR-based diagnostic platform in rapid and sensitive detection of disease marker, as well as multiplexing. With these results, this dissertation aims to the development of magnetic labels for GMR-based magnetic immunoassays towards simultaneous detection of multiple disease markers.

TABLE OF CONTENTS

LIST OF TABLES

LIST OF FIGURES

ABBREVIATIONS

AMR ..... anisotropic magnetoresistance
BLAST ..... basic local alignment search tool
BSA ..... bovine serum albumin
c ..... speed of light
core@shell ..... core-shell
CA ..... citric acid
CA 19-9 ..... carbohydrate antigen 19-9
CEA ..... carcinoembryonic antigen
CEACAM-1 ..... carcinoembryonic antigen-related cell adhesion molecule 1
CMOS ..... complementary metal oxide semiconductor
Coll-MB ..... colloidally assembled magnetic bead
CT ..... computerized axial tomography
$\delta m/\delta \boldsymbol{m}$ ..... delta-M plot
$\boldsymbol{D}$ ..... diameter
D_s ..... critical size for single-domain state
D_p ..... critical size for superparamagnetism
$\boldsymbol{D_{h,int}}$ ..... intensity-weighted hydrodynamic size
DCD ..... direct current demagnetization
DI H_2O ..... deionized water
DLS ..... dynamic light scattering
DMSA ..... dimercaptosuccinic acid
DMSO ..... dimethyl sulfoxide
DSP ..... dithiobis(succinimidyl propionate)
DTAB ..... dodecyltrimethylammonium bromide
E_a ..... anisotropy energy
E_H ..... Zeeman energy
e ..... charge of electron
EDC ..... 1-ethyl-3-(3-dimethylaminopropyl)carbodiimide
EDS ..... energy dispersive X-ray spectroscopy
EDX ..... energy dispersive X-ray spectroscopy
ELISA ..... enzyme linked immunosorbent assay
EtOH ..... ethanol
Fe_3O_4 ..... magnetite
$Fe(acac)_3$ ..... iron acetylacetonate
FITC ..... fluorescein isothiocyanate
FMNP ..... ferro-/ferrimagnetic nanoparticle

γ-Fe_2O_3 ..... maghemite
GMR ..... giant magnetoresistance
ħ ..... reduced Plank's constant
$\boldsymbol{H}$ ..... magnetic field
$\boldsymbol{H_{app}}$ ..... applied magnetic field
$\boldsymbol{H_c}$ ..... coercivity
ICDD ..... international center for diffraction data
ICP-MS ..... inductively coupled plasma mass spectroscopy
IOMB ..... iron oxide magnetic bead
IOMB@PVP ..... polyvinylpyrrolidone-coated iron oxide magnetic bead
IONP ..... iron oxide nanoparticle
IR ..... infrared spectroscopy
IRM ..... isothermal remanent magnetization
k_B ..... Boltzmann constant
K ..... anisotropy constant
K ..... Kelvin
LbL ..... layer-by-layer
LoD ..... limit of detection
μ_B ..... Bohr magneton
µMBs ..... microbead
$\boldsymbol{m}_{particle}$ ..... magnetic moment per particle
$\boldsymbol{m}$ ..... magnetic moment
$\boldsymbol{M}$ ..... magnetization
$\boldsymbol{M_s}$ ..... saturation magnetization
$\boldsymbol{M_r}$ ..... remanent magnetization
MES ..... 2-(N-morpholino)ethanesulfonic acid
MR ..... magnetoresistance
MMP-7 ..... matrix metalloproteinase-7
MNP ..... magnetic nanoparticle
MRE ..... molecular recognition element
MWCO ..... molecular weight cutoff
NaCl ..... sodium chloride
NCCN ..... national comprehensive cancer network
NH_4OH ..... ammonium hydroxide
NIH ..... national institute of health
OPN ..... osteopontin
pM ..... picomolar
PAA ..... polyacrylic acid
PAAm ..... polyallyl amine
PBS ..... phosphate-buffered saline
PDAC ..... pancreatic ductal adenocarcinoma
PEI ..... polyethyleneimine
PSS ..... polystyrene sulfonate
PVA ..... polyvinyl alcohol
PVP ..... polyvinylpyrrolidone
ρ ..... density

rh ..... recombinant human
σ ..... specific magnetization
$\boldsymbol{S}$ ..... surface area
SEM ..... scanning electron microscopy
SPMNP ..... superparamagnetic nanoparticle
sulfo-NHS ..... N-hydroxysuflosuccinimide
θ ..... angle
T ..... temperature
T_B ..... blocking temperature
TEM ..... transmission electron microscopy
TIMP-1 ..... tissue inhibitor of metalloproteinase 1
U_E ..... electrophoretic mobility
V ..... volume
VSM ..... vibrating sample magnetometry
χ_{irr} ..... irreversible susceptibility
XRD ..... X-ray diffraction
ζ-potential ..... zeta-potential
ZFC/FC ..... zero-field cooled/field cooled
ZFNC ..... zinc ferrite nanocube
ZFNC@SiO_2 ..... silica-coated zinc ferrite nanocube
ZFMB ..... zinc ferrite magnetic bead
ZFMB@PVP ..... polyvinylpyrrolidone-coated zinc ferrite magnetic bead
ZFMB@PVP@PAA ..... polyacrylic acid-coated zinc ferrite magnetic bead
ZFMB@PVP@PAA@SA ..... streptavidinated zinc ferrite magnetic bead
ZFNP ..... zinc ferrite nanoparticle
$Zn(acac)_2$ ..... zinc acetylacetonate

ACKNOWLEDGEMENTS

Most of all, I would like to thank my advisor, Marc D. Porter, for accepting me as his graduate student, hiring me, educating me, not kicking me out of the group, and officiating my wedding. It is ineffable how much I appreciate Marc and the things that were given in Marc's group. Second, I want to express my gratitude to the Porter group members (Lexi, China, Jason, Nick, Alex, Colin, Lars, Bev, Jen, and Mike) for mostly sharing the misery of graduate school, a little bit of fruitful discussions (Haha!), and many fun times. Also, I 'obrigado' to Elias Ribeiro da Silva for enduring me as a roommate. To my families in Korea, I am grateful for their emotional and financial support.

Last but the most, I am thankful to my loved ones, Pooreun and Theodore. My wife and I first met in the beautiful spring of March 2012. Since then, we have been together, had our little Theodore, and became a family.

To my lovely wife, thank you for all of your hard work and sorry that you had to become the one who sacrificed your life for me and Teddy. If you were not with me, I would not have been able to get to this point. Love you and hope that we together can make it to the end.

To my little one, there are only two things that I want from you. First, do not dare to serve in the Korean military. Second, never go to graduate school. Love you and hope that you can find a lot of things that make your life joyful and happy.

CHAPTER 1

INTRODUCTION

1.1 Overview

Early detection of cancer is an important strategy for public health. Frequently, early diagnosis of cancer increases the chances for effective treatment, which can improve outcomes and/or increase the life expectancy/quality of a patient after the treatment. Diagnosis of cancer in its early stage requires screening of a healthy population and the recognition of disease markers early in disease progression. In the first stages of cancer, a number of markers indicative of a cancer can be present and the level of the cancer markers present in a patient sample is usually low. Therefore, a diagnostic tool capable of simultaneous detection of multiple disease markers as well as with a high analytical sensitivity is required for early diagnosis of cancer.

One of the most common *in-vitro* diagnostic testing platforms for disease diagnosis is the solid-phase immunoassay. Solid-phase immunoassays utilize the selective and specific targeting function of antibodies to antigens that indicate the presence of a disease. However, these immunoassays are often designed to detect a single analyte and, as a consequence, can require a large sample volume and extensive labor in order to simultaneously screen multiple antigens, which can limit widespread usage due to an

increase in test costs. In addition, the existing solid-phase immunoassays usually require sophisticated instrumentation and highly skilled technicians, both of which can prove challenging in resource-limited settings. Therefore, the development of immunoassays with a high sensitivity, low cost, and multiplexing capability is of great interest in the bioanalytical arena and clinical diagnostics.

Giant-magnetoresistive (GMR) sensors, which had been used as a readout mechanism in computer hard drives, are small, sensitive, and have high read rates. The last decade has seen a large growth in the use of GMR sensors as a quantitative tool for disease detection by combining immunoassays with magnetic labels. In this vein, this dissertation describes the development of a GMR-based diagnostic tool for the detection of potential pancreatic cancer markers. The work presented includes: (1) the preparation of new types of magnetic labels, and (2) the development of multiplexed immunoassays for the detection of potential pancreatic cancer markers by using these magnetic labels.

This Introduction provides background materials relate to the topics addressed throughout the dissertation, including solid-phase immunoassays, magnetic nanoparticles, magnetism, GMR sensors, and pancreatic cancer. The main body of this dissertation consists of four original research chapters. Chapter 2 describes a method to deposit a uniform silica layer on ferrimagnetic zinc ferrite nanocubes enabled layer-by-layer deposition of polyelectrolyte. The results of magnetic characterizations in each synthesis step are also presented. Chapter 3 investigates the magnetic properties of colloidally assembled zinc ferrite magnetic beads. Chapter 4 discusses the synthetic procedures used to build magnetic labels based on colloidally assembled magnetic beads and their application in GMR-based immunoassays. Chapter 5 extends the utilization of the

magnetic labels developed in Chapter 4 in the simultaneous detection of potential pancreatic cancer markers in buffer and serum. This dissertation concludes with a perspective on potential importance of development and optimization of magnetic labels for solid-phase immunoassays and on future directions in the early diagnosis of pancreatic cancer based on solid-phase immunoassays and GMR sensors.

1.2 Solid-phase Immunoassays

In the 1930s, Heidelberger and colleagues made major contributions to immunochemical studies of antigen-antibody reactions.[1-4] They showed that antigen-antibody reactions take place in accordance with a set of predictable rules grounded in biochemical interactions. They also demonstrated that the quantity of antigen in a sample can be accurately determined by using an antigen-antibody reaction. These principles received tremendous attention and allowed the use of antigen-antibody binding as quantitative tools in immunochemistry and clinical chemistry.

The work by Yalow, Berson, and Ekins in the late 1950s opened up the age of radioimmunoassays.[5-6] The first radioimmunoassay used a competitive format, in which the analyte of interest and a radioisotope-labeled derivative of the analyte were mixed and applied to a finite amount of antibody. As the concentration of the analyte increases, more of the analyte binds to the antibody, decreasing the ratio of antibody-bound radioisotope-labeled analyte to free radioisotope-labeled analyte. Then, the radioactivity of the unbound analyte in the supernatant is used to quantify analyte concentration in the sample. Competitive binding is concentration dependent and the signal output is inversely correlated to the amount of analyte in the sample.

Since then, there has been a number of significant improvements in assay configuration, reagents, and detection tools. The development of monoclonal antibody production allowed new immunoassay designs with improved sensitivity and specificity.[7] The first two-site immunoassay (*i.e.*, sandwich immunoassay) was introduced in 1971.[8] A schematic illustration of a sandwich immunoassay is shown in Figure 1.1. In this assay, capture antibodies are tethered on a surface via adsorption or covalent bonding. In the next steps, analytes specific to the capture antibody bind to the capture antibodies, and secondary antibodies, which may or may not be modified with a label for signal transduction, tag the bound analytes. Finally, the response from the surface-bound labels is used in quantitative analysis of analyte-antibody binding events.

Efforts to replace radioisotopic materials with alternatives have been made to avoid possible health risks, stability problems, and other difficulties in handling radioisotopes. Alternatives include enzymatic labels with chromogenic and fluorogenic substrates,[9] and fluorescent, chemiluminescent, and bioluminescent molecules.[10-12] The utilization of other solid surfaces (*e.g.*, gold and carbon materials) was a major improvement as well.

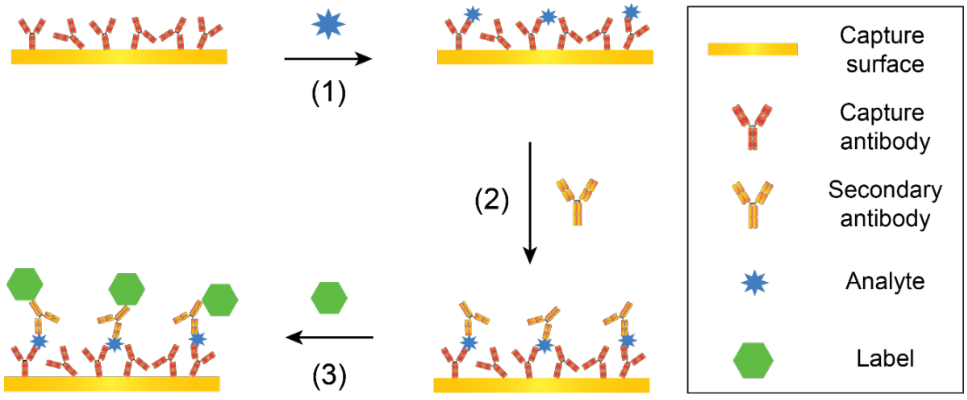

Figure 1.1 Schematic diagram for a sandwich immunoassay: (1) analyte binding to capture antibody; (2) secondary antibody binding to the capture analyte; and (3) labeling.

Immunoassays with colorimetric readout method, *e.g.* enzyme-linked immunosorbent assay (ELISA), are the gold standard in today's *in-vitro* diagnostics arena. However, nanotechnology-based detection methods and nanoparticle labels have begun to meet the demand for diagnostic tools with a high speed, sensitivity, improved levels of detection, and higher throughput. Single-molecule enzyme-linked immunosorbent assay (a.k.a., digital ELISA) can detect single protein molecules at sub-femtomolar concentrations.[13] Immunoassays using surface-enhanced Raman scattering readout and gold nanoparticle labels have also redefined detection.[14-16] Giant-magnetoresistive sensors use magnetic nanoparticles as labels and are a promising alternative for the simultaneous detection of multiple markers with low analytical sensitivity.[17-18] Emission-based detection is highly sensitive and takes advantage of the photostability and narrow emission bands of quantum dot and lanthanide-derived nanoparticle labels. The more traditional organic dye labels in assays suffer from photobleaching and broad emission bands which can hinder their usage in multiplexed assays.[19] Each of these techniques exhibits great promise for the next generation of diagnostic technologies for use in clinical, environmental, and food testing arenas.

The last few decades have witnessed a number of breakthroughs in the field of immunoassays regarding assay configuration, labeling strategies, and new instrumentation. Some on-going and future efforts in this area include the development of: (1) preanalytical treatments for the detection of analytes in serum and patient samples; (2) multiplexed immunoassays for the detection of a panel of analytes; (3) biosensors suitable for use in field-deployable settings and chip-scale detection; and (4) assays with even lower limits of detection, rapid turnaround time, and reduced cost. Therefore, it is expected that

immunoassays will continue to be developed and be used as *in-vitro* diagnostic tools in the coming decades.

1.3 Synthesis of Magnetic Nanoparticles

Magnetic nanoparticles (MNPs) are a class of nanoparticle that can be manipulated by an external magnetic field. Numerous MNPs have been synthesized with a range of composition, like iron oxides (Fe_3O_4 and γ-Fe_2O_3), ferrites ($Mg_xFe_{3-x}O_4$, $Zn_xFe_{3-x}O_4$, and $Co_xFe_{3-x}O_4$), metals (Fe and Co), and metal alloys (FePt, NiCo, and FeCo).[20] There are a few popular synthetic methods for producing MNPs, including coprecipitation,[21] thermal decomposition,[22] hydrothermal synthesis,[23] and microemulsion.[24] These methods have been developed and fine-tuned in order to generate MNPs with high magnetic moments as well as a high level of uniformity in size and shape. Table 1.1 lists the advantages and disadvantages of the different synthetic routes. At present, MNPs prepared using coprecipitation and thermal decomposition have been the most extensively studied of the materials, both at a fundamental level as several types of applications. The microemulsion method can also produce MNPs with different morphologies, but is not as scalable as other routes. While hydrothermal and gas-phase methods have not been heavily explored, those routes can potentially be effective methods for the synthesis of high-quality MNPs. To date, thermal decomposition has proven to be the best option to synthesize MNPs uniform in size and shape. Thermal decomposition enables the synthesis of MNPs with excellent control over size and shape (a standard deviation of size typically less than 10%). With thermal decomposition (Figure 1.2A), MNPs are synthesized by decomposing organo-metallic precursors in organic media with surface-capping agents (*e.g.*, fatty acids) at a

Table 1.1 Comparison of different synthetic routes for MNPs.

Synthetic method	Synthesis condition	Reaction Temperature	Solvent	Surface-capping Agent	Size control	Shape control	Reference
Co-precipitation	ambient	20−90 °C	water	not needed	poor	poor	[21, 25]
Thermal decomposition	inert	100−350 °C	organic compound	needed	very good	very good	[22]
Hydrothermal	high pressure	150─250 °C	water and ethylene glycol	needed	very good	very good	[26-27]
Gas-phase	high temperature	Flame	─	not needed	poor	good	[28]

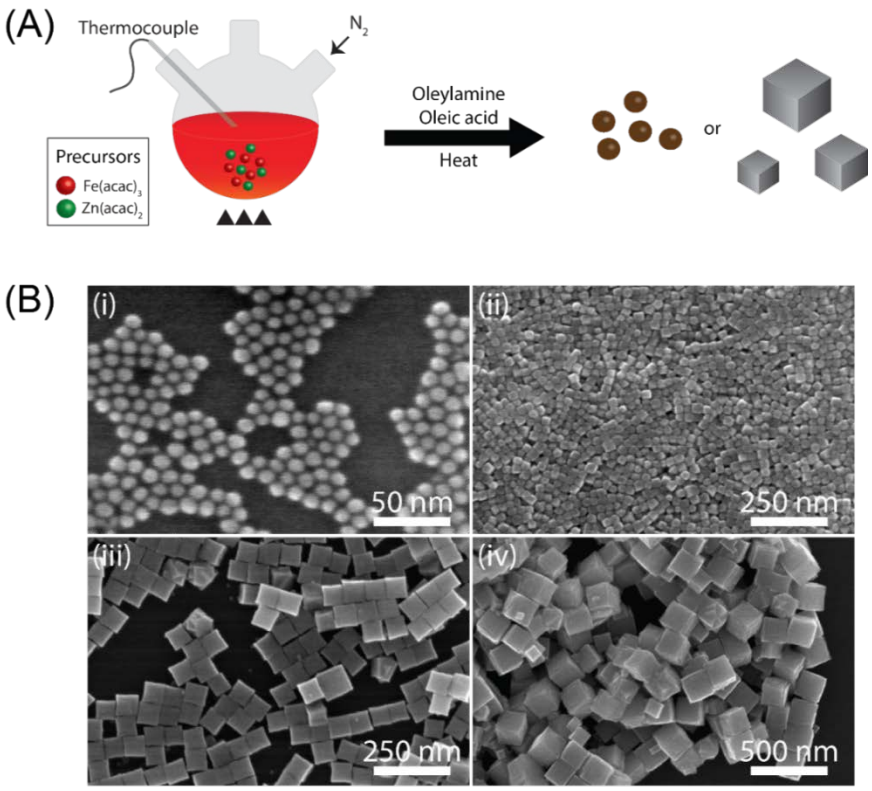

Figure 1.2 Synthesis of MNPs. (A) Schematic illustration of thermal decomposition. (B) Electron micrographs of zinc ferrite nanoparticles synthesized via thermal decomposition: (i) spherical and (ii-iv) cubic MNPs of different sizes.

high temperature (250 – 350 °C), as shown in Figure 1.2A. Organo-metallic precursors include metal acetylacetonates [$M(acac)_n$; M = Fe, Mn, Co, Zn, and Ni; n = 2 or 3] and metal carbonyls (*e.g.*, $Fe(CO)_5$ and $Co_2(CO)_8$). Fatty acids and hydrocarbons with terminal groups (*e.g.*, carboxylic acids and amines) are often used as surface-capping agents. Because of the long hydrocarbon chains in the surface-capping agents, the as-synthesized MNPs can only be dispersed in nonpolar solvents. As shown in Figure 1.2, MNPs with different sizes and shapes can be produced by changing precursors, solvents, and/or surface-capping agents. These materials must then be surface modified to meet the hydrophilicity required for biomedical applications.

1.4 Concepts in Magnetism and Measurement of Magnetic Parameters

There are several different systems currently used to define magnetic quantities. Table 1.2 summarizes cgs and SI systems. One of the most fundamental concepts in magnetism is a magnetic field (***H***). ***H*** is generated when an electrical charge is in motion. ***H*** at any given point is represented by a vector field, which has both a direction and a strength. When ***H*** is produced in a volume of space, there is an energy gradient in the volume and, therefore, a force is produced. This force can be detected by the torque on a magnetic dipole like a bar magnet. The magnetic moment (***m***) of a magnet or electron equals the torque applied on the magnet or electron by an external ***H***. Consider two bar magnets adjacent to each other. The total ***m*** of the two magnets is the vector sum of magnetic moments of the individual magnets. In this case, the total ***m*** is doubled by an increase in the volume (*V*). However, the ***m*** per volume has not changed. This volume-normalized ***m*** is called the magnetization (***M***), and is written simply as follows.

$$\boldsymbol{M} = \frac{\boldsymbol{m}}{V} \tag{1.1}$$

Table 1.2 Unit systems in magnetism.

Quantity	Symbol	cgs	SI	Conversion factor
Field	***H***	oersted (Oe)	$A \cdot m^{-1}$	10^{-4}
Magnetic moment	***m***	emu	$A \cdot m^{2}$	10^{-3}
Magnetization	***M***	emu/cm^{3}	$A \cdot m^{-1}$	10^{3}
Specific magnetization	$\boldsymbol{\sigma}$	emu/g	$A \cdot m^{2}/kg$	1

Sometimes, it is convenient to define the value of the magnetization per unit mass. This mass-normalized magnetization is called the specific magnetization (σ) and is written as:

$$\sigma = \frac{\boldsymbol{m}}{V\rho} = \frac{\boldsymbol{M}}{\rho} \tag{1.2}$$

where ρ is the density of the material. Throughout this dissertation, the convention of volume magnetization ($\boldsymbol{M}$) is used interchangeably with specific magnetization (σ).

When it comes to nanomaterials, there are several parameters that quantify the important magnetic characteristics of nanomaterials: (1) saturation magnetization; (2) remanent magnetization; and (3) coercivity. These magnetic components can be determined using a field-dependent magnetization curve (*i.e.*, magnetic hysteresis curve), as shown in Figure 1.3. In ferro-/ferrimagnetic materials, $\boldsymbol{M}$ increases with $\boldsymbol{H}$. At a

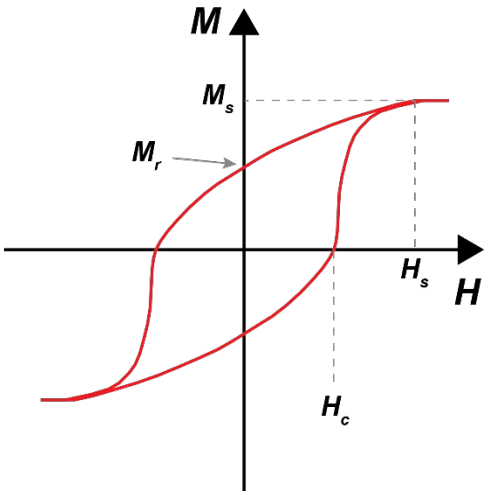

Figure 1.3 Schematic illustration of hysteresis curve of a ferromagnetic material. The hysteresis curve represents the change in magnetization ($\boldsymbol{M}$) as a function of an external magnetic field ($\boldsymbol{H}$). This figure was adapted from reference 29.

sufficiently large field, $\boldsymbol{M}$ becomes independent of $\boldsymbol{H}$. That is, $\boldsymbol{M}$ for the materials has reached its saturation magnetization ($\boldsymbol{M_s}$). Next, as $\boldsymbol{H}$ decreases, $\boldsymbol{M}$ decreases. The value of $\boldsymbol{M}$ at $\boldsymbol{H}$ = 0 is called the remanent magnetization ($\boldsymbol{M_r}$). The field strength required to reduce $\boldsymbol{M}$ to zero is called the coercivity ($\boldsymbol{H_c}$), and is defined by the $-x$ and $+x$ intercepts of the curve.

1.5 Types of Magnetism

All substances are magnetic, but a few are magnetically much stronger than others. The magnetic moment of a substance results entirely from the motion of electrons in atoms. The nucleus also has an $\boldsymbol{m}$, but it is insignificant with respect to the $\boldsymbol{m}$ of an electron. Magnetism arises from two motions of the electrons: (1) orbital motion; and (2) spin. The magnetic moment of spin motion is equal to that of electron motion in the first Bohr orbital, and, as represented in Equation 1.3, is called 'the Bohr magneton', μ_B:

$$\mu_B = \frac{e\hbar}{2mc} = 0.927 \times 10^{-20} emu = 9.27 \times 10^{-24}\, A \cdot m^2 \qquad (1.3)$$

where e is charge of an electron, c is speed of light, and ħ is reduced Plank's constant.

Each electron in an atom has its own spin and orbital motion. The magnetic moments of an electron associated with spin and orbital motion are parallel to its axis of spin and normal to the plane of its orbital, respectively. Because these magnetic moments are vector quantities, a magnetic moment in an atom is the vector sum of all possible moments. Thus, the magnetic moments of all the electrons can cancel out, which results in the atom exhibiting no net magnetic moment (*i.e.*, diamagnetism) or the atom can retain a

net magnetic moment due to partial cancellation of the moments. The materials composed of the atoms with net magnetic moments exhibit para-, ferro-, ferri-, or antiferromagnetism.

Magnetism in a substance can be classified into one of four categories: (1) diamagnetism; (2) paramagnetism; (3) antiferromagnetism; and (4) ferro/ferrigmagnetism. These differences arise from the interaction between atomic moments in a substance. Atomic moments in diamagnetic materials are zero due to the absence of unpaired electrons. While there are no interactions in paramagnetic materials, strong interactions between atomic moments are present in ferromagnetic, ferrimagnetic, and antiferromagnetic materials.

Ferromagnetic materials, such as iron, nickel, or cobalt, have large magnetic moments, due to strong magnetic interactions between atoms.[29-30] For example, the $\boldsymbol{M}$ of iron is ~1700 emu/cm^3 at 50 Oe, while $\boldsymbol{M}$ for a typical paramagnetic material will be ~10^{-3} emu/cm^3 at the same field.[29] In other words, ferromagnetism is at least ~100,000× stronger than paramagnetism. This can be attributed to the fact that, unlike paramagnetic substances, the interaction of the atomic moments in ferromagnetic materials is very strong due to the quantum mechanical effect known as direct exchange interaction. Below the Curie temperature, *i.e.*, the temperature at which ferromagnets become paramagnets, all atomic moments in a ferromagnet become aligned (Figure 1.4A) and the strong exchange forces between atoms can spontaneously magnetize the ferromagnet even in the absence of a magnetic field.

Similar to ferromagnetism, ferrimagnetic substances exhibit a spontaneous magnetization below the Curie temperature.[31] Ferrimagnets are typically ionic compounds and oxides of iron and other metals (*e.g.*, nickel, cobalt, and manganese), often called

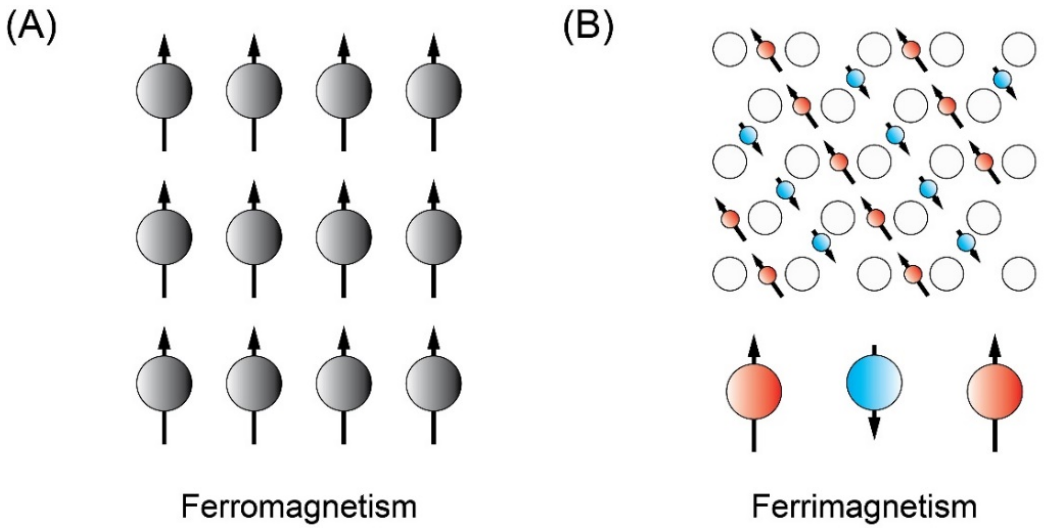

Figure 1.4 Schematic illustration of the atomic magnetic moments in (A) ferromagnetic and (B) ferrimagnetic substances. Atomic moments in a ferromagnetic are aligned in a parallel fashion. However, in a ferrimagnet, two atomic moments in the different sublattices are aligned in an antiparallel manner. Due to the uneven atomic moments, ferrimagnets can be spontaneously magnetized and show a net strong magnetization. This illustration was modified based on reference 29.

ferrites. There are two types of magnetic ferrites with different crystal structures: (1) hexagonal; and (2) cubic. Barium and strontium ferrites ($BaO{\cdot}6Fe_2O_3$ and $SrO{\cdot}6Fe_2O_3$) are examples of ferrites with a hexagonal crystal structure. The general formula for cubic ferrites is MFe_2O_4, where M is a divalent metal ion like Mn, Ni, Fe, or Co. As mentioned, ferrites are ionic compounds and their magnetic properties depend on the exchange interactions between magnetic ions in the structure, as illustrated in Figure 1.4B.

Figure 1.5 shows the crystal structure of cubic ferrites composed of closed packed oxygen ions and two sublattice sites, tetrahedral (A) and octahedral (B), that can be occupied by metal ions.[32] The exchange interactions (*i.e.*, superexchange interactions) of the magnetic metal ions are mediated by oxygen ions. Note that the oxygen ion (O^{2-}) in ferrites does not have a net magnetic moment. Since the exchange forces of atoms between

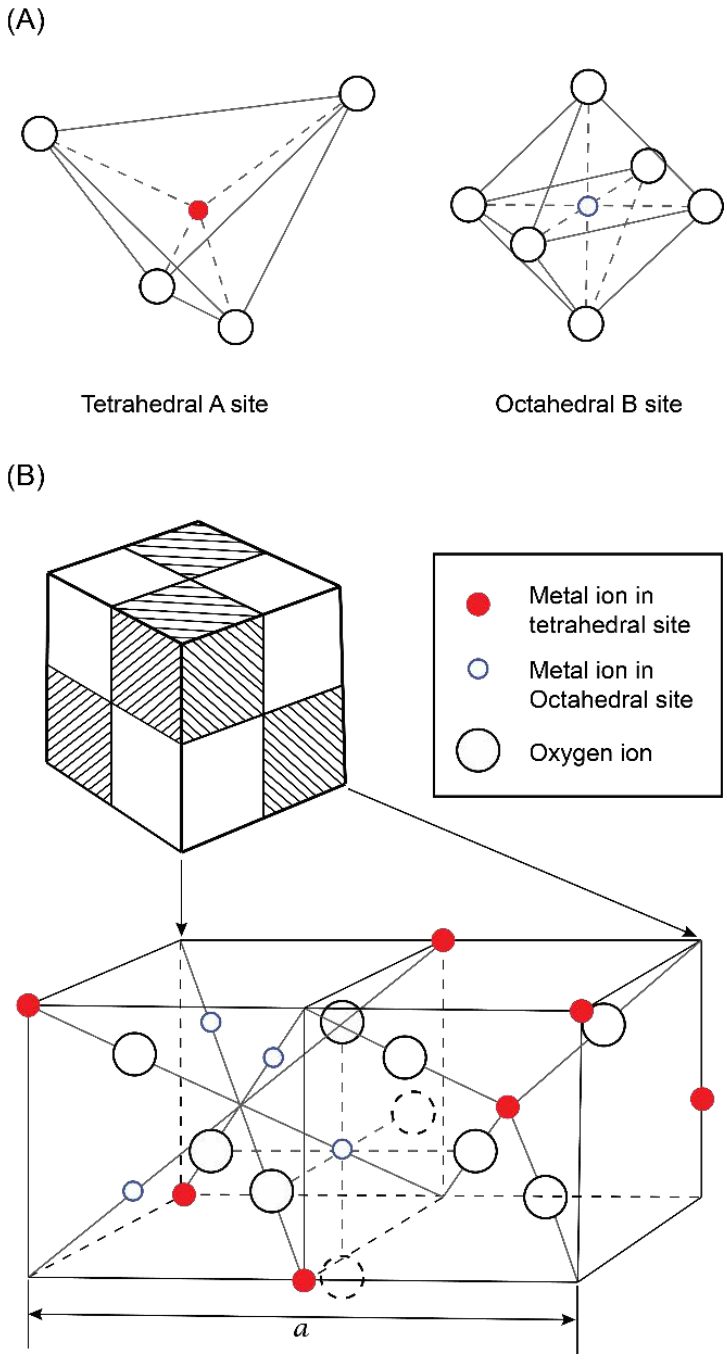

Figure 1.5 Spinel crystal structure of a cubic ferrite with a general formulation ($M^{2+}Z_2^{3+}O_4^{2-}$). (A) Two sublattices of the spinel structure (*i.e.*, tetrahedral and octahedral sites), occupied with metal ions. (B) The cubic crystal system with oxygen anions (O^{2-}) in a cubic close-packed lattice, and cations (M^{2+} and Z^{3+}) occupying two interstices in the lattice. Note that this figure was adopted and modified from reference 29.

A and B sites are negative, the spontaneous magnetization direction of ions in A sites is opposite to that of ions in B sites. This causes partial cancellation of magnetization. Therefore, ferrites have a net spontaneous magnetization.

The existence of magnetic domains in a ferromagnet, another important concept in magnetism, was introduced by Pierre Weiss in 1906.[29] A magnetic domain is defined as a region that has a spontaneous magnetization in one direction due to the parallel alignment of the individual atomic moments within the domain. It should be noted, however, that the magnetizations of different domains can be randomly with respect to each other, resulting in a net magnetization of zero.

Magnetic domain structures are closely related to the magnetic behavior of ferromagnetic materials (*e.g.*, iron, nickel, cobalt, and alloys), and ferrimagnetic materials (*e.g.*, ferrites). Multiple domains can exist in a ferromagnetic material and the domains are separated by domain walls (a.k.a., the Bloch wall).[33] Domain walls are the interfacial region between two domains and the magnetization direction in one domain coherently rotates to the direction in a neighboring domain in the boundary. The reason why a ferromagnet divides into various domains, rather than having the magnetization in one direction throughout the material, is to minimize its internal energy (*i.e.*, magnetostatic energy). The size of domain is governed by the balance of several energies within the material, including the exchange energy, crystal anisotropic energy, demagnetizing energy, and domain wall energy.[29, 34]

Frenkel and Doefman predicted that a particle of ferromagnetic materials below the linear dimensions of 10^{-5} cm would have a single magnetic domain and, therefore, must be permanently magnetized.[35] As the size of a ferromagnetic particle decreases, more

energy is required to create domain walls than the total magnetostatic energy of a single-domain particle. Therefore, there is a critical size (D_s) for which the single-domain state is favored and the magnetization direction of a single-domain particle is invariant throughout the magnet.

1.6 Magnetism in Nanoscale

In bulk magnetic materials, the magnetic properties depend on composition, crystallographic structure, magnetic anisotropic energy, structural defects, and a number of other factors.[29, 36] However, when the size scale of the particle approaches the nanoscale, other parameters such as size and shape can have a strong impact on magnetic properties. When the measured value of a physical property is dependent on the size of the material, the property is said to exhibit a 'size effect'. Among magnetic properties, Hc has a pronounced size effect (Figure 1.6). As the particle size decreases in a multi-domain

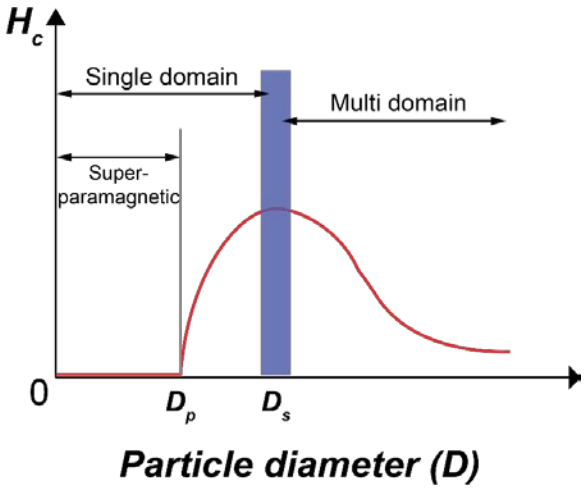

Figure 1.6 Schematic illustration of variation of coercivity ($\boldsymbol{H_c}$) as a function of particle diameter. D_p is a critical diameter of MNPs, at which the transition of superparamagnetism to ferro-/ferrimagnetism occurs. This figure was adapted from reference 29.

region, $\boldsymbol{H_c}$ typically increases and reaches a maximum. At this point, the transition from a multi-domain to single-domain state occurs. Upon further reduction in particle size below D_s, $\boldsymbol{H_c}$ decreases to zero.

If we consider a single-domain particle with a volume (V) and uniaxial anisotropy (*i.e.*, only one easy axis), the energy of the magnetic particle is then the sum of anisotropy energy (E_a) and the Zeeman energy (E_H), and can be written as follows,

$$E = E_a + E_H = KV \sin^2 \theta - mH\cos\delta \tag{1.4}$$

where K is the anisotropy constant, θ is the angle between the direction of $\boldsymbol{m}$ and the easy axis, and δ is the angle between $\boldsymbol{m}$ and $\boldsymbol{H}$ (Figure 1.7A). As the size of MNPs decreases below a certain critical size (D_p), all of the atomic magnetic spins become aligned in the same direction and behave like a single magnetic moment. In this regime, single-domain MNPs have a spontaneous magnetization in an energetically favorable direction (*i.e.*, in the

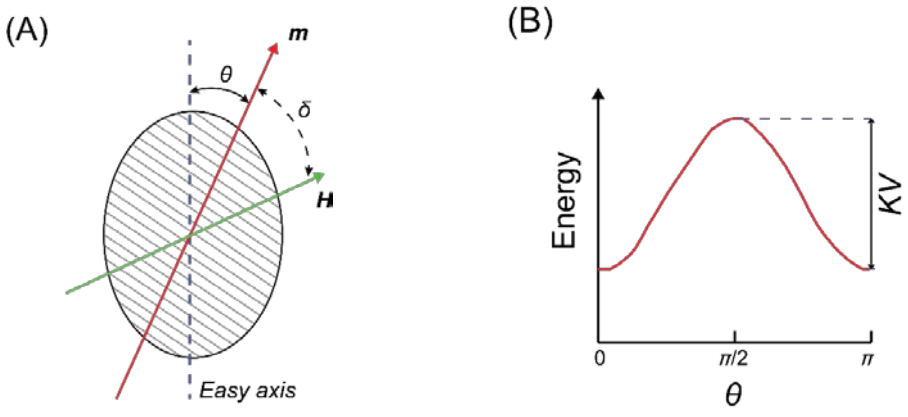

Figure 1.7 Magnetic anisotropy of a MNP. (A) Single-domain particle with uniaxial anisotropy, and (B) Dependence of energy of a particle with an uniaxial anisotropy on the angle between the magnetic moment and the easy axis in the absence of $\boldsymbol{H}$. This figure was modified from reference 37.

easy axis). The two opposite orientations with 180° along the easy axis are separated by the anisotropic energy barrier shown in Figure 1.7B. When a particle is small enough, the energy barrier (ΔE) of the particle decreases and, therefore, the thermal energy of the particle is sufficient to rapidly change the magnetization direction of the particle. Such a fluctuation leads to a net magnetization of zero at room temperature. This behavior is called superparamagnetism.[29, 37] Due to the special characteristics of superparamagnetic nanoparticles (*i.e.*, $\boldsymbol{M_r}$ and $\boldsymbol{H_c}$ are zero while having a high magnetic moment compared to paramagnetic materials), superparamagnetic nanoparticles have been extensively used in nanomedicine, magnetic resonance imaging contrast agents, biosensors, and bioseparations.

1.7 Giant Magnetoresistance (GMR)

Magnetoresistance (MR) is the change in resistance of metallic materials due to the presence or absence of an external magnetic field ($\boldsymbol{H_{app}}$). This arises from the fact that the trajectory of an electron moving such a material can be altered by $\boldsymbol{H_{app}}$. All metals exhibit a certain degree of MR, typically with a change in resistivity of less than 1%. However, Baibich et al. reported in 1988 that a structure comprised of alternating nanometrically thin layers of magnetic (*e.g.*, iron) and non-magnetic (*e.g.*, chromium) materials can undergo a change in MR up to 80%.[38] This large change in MR is referred to as giant magnetoresistance (GMR). Two requirements must be met for GMR to occur: (1) the relative orientation of the magnetization in adjacent magnetic metal layers can change; and (2) the thickness of the multilayer must be less than the mean free path of an electron.[39]

The GMR effect occurs due to spin-dependent scattering and transmission of conduction electrons in the interfaces between ferromagnetic and non-magnetic layers as shown in

Figure 1.8.[39] The magnitude of change in the resistance is a function of the thickness of each layer.[38, 40] Figure 1.8A shows a schematic visualization of the transport of conduction electrons in the GMR multilayer (thicker ferromagnetic iron layers with thinner non-magnetic chromium spacers). In the absence of $\boldsymbol{H_{app}}$, antiferromagnetic coupling between adjacent magnetic layers holds through the entire multilayer, which results in a high resistance due to high scattering potentials and the suppression of short circuit effect.[38]

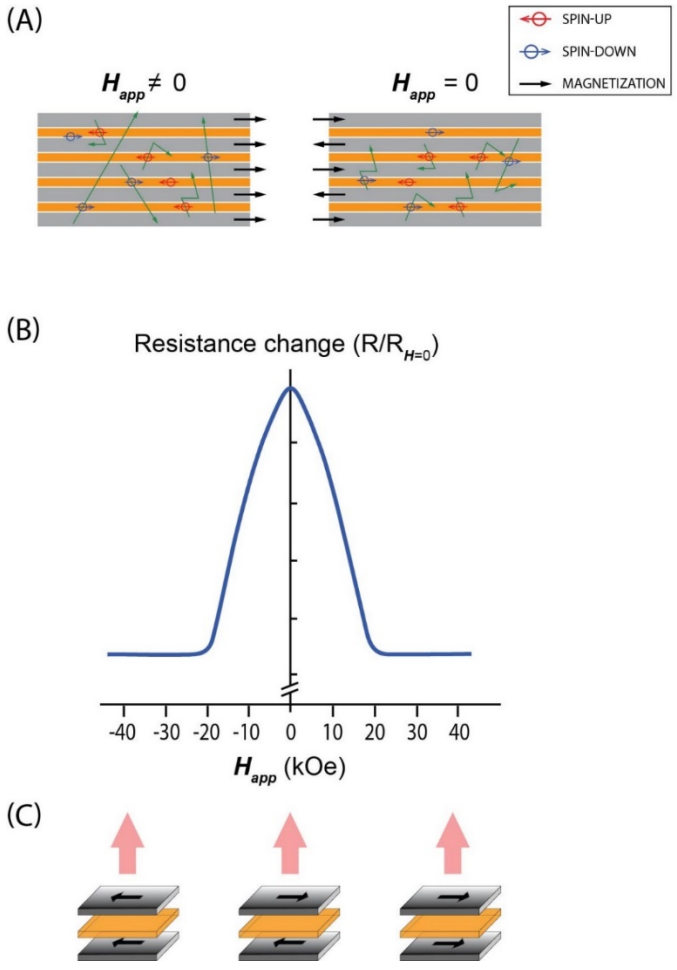

Figure 1.8 Giant-magnetoresistance. (A) Schematic visualization of spin-dependent transport of conduction electrons in the multilayers of ferromagnetic and non-magnetic materials. (B) Magnetoresistance change as a function of $\boldsymbol{H_{app}}$ in a multilayer. (C) Schematic illustration of magnetic layers separated by a non-magnetic layer, depicting the relative magnetization orientations.

Under $\boldsymbol{H_{app}}$, the magnetization in the ferromagnetic layers aligns in a parallel fashion, which leads to reduction in interface scattering and increase in transmission of the spin-down electrons. Therefore, the resistivity in the multilayer decreases in the presence of $\boldsymbol{H_{app}}$.

1.8 Magnetoresistive Sensors

The discovery of GMR has fueled breakthroughs not only in the magnetic data storage industry (e.*g.*, GMR sensors as read heads for data retrieval from the hard-disk drives), but also in bioanalytical sensors. There are several types of magnetoresistive-based sensors developed so far, including those based on spin valve, magnetic tunneling junction, Hall effect, anisotropic magnetoresistance (AMR), and GMR multilayers.[41] In all cases, MR output (*i.e.*, read an electrical voltage change) arises from changes in the local magnetic field in close proximity to the sensing area.

For bioanalytical applications, GMR sensors are commonly used as a readout tool in association with a sandwich immunoassay format, in which molecular targets are captured using specific interaction of molecular recognition elements on the sensor surface and then tagged with magnetic labels as described in Figure 1.9. The early work with GMRs used micron-sized magnetic labels and demonstrated the ability to detect the individual labels.[42-43] In the following years, the use of MNPs as labels overcame limitations of the micron-sized labels (*e.g.*, ballistic deposition of labels and screening the neighboring binding sites) and permitted very sensitive detection of proteins in GMR array sensors.[17, 44-45] In addition, GMR sensor arrays have been used for real-time monitoring of protein-protein interactions and for parallel detection of multiple biomarkers with each

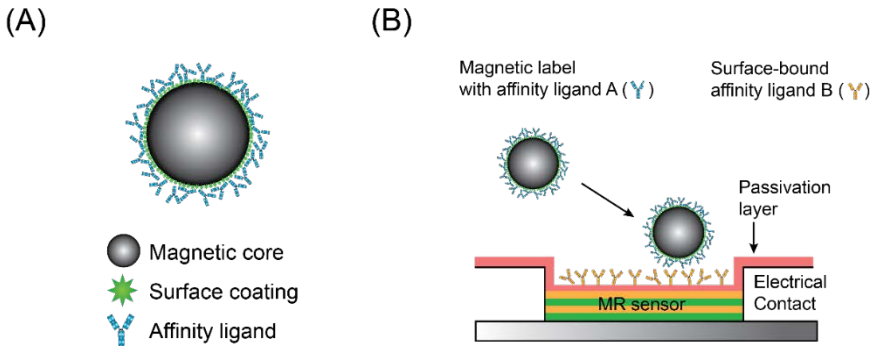

Figure 1.9 MR sensor platform. (A) Schematic illustration of magnetic labels composed of magnetic core, surface coating, and affinity ligand. (B) Simplified scheme for magnetically labeled biomolecule detection in MR sensor. The magnetic field from the magnetic moment of the label bound on the sensor surface changes the resistance of the sensor, which results in a voltage change (ΔV) at a constant current.

sensor modified with various antibodies.[46-48] The GMR arrays were further advanced for the field-deployable setting by placing two chips side-by-side: a GMR sensor array and a complementary metal oxide semiconductor (CMOS) chip for signal processing.[49]

1.9 Pancreatic Adenocarcinoma

Pancreatic Adenocarcinoma (*i.e.*, pancreatic cancer) is the most common type of cancer of the pancreas. Although pancreatic cancer is the tenth most prevalent cancer in the United States, it is the fourth leading cause of cancer death in men and women at 5-year survival rate of ~8%.[50-51] As opposed to the steady increase in survival rates for many of cancers, there has been little improvement with pancreatic cancer.[50-51] It is estimated that pancreatic cancer will become the second leading cause of cancer death in the United States by 2020.[52] The high mortality rate of pancreatic cancer stems mainly from: (1) its asymptomatic presentation in early stages of progression; (2) its common symptoms (*e.g.*, painless jaundice and abdominal or back pain); and (3) its lack of a single biomarker with

high sensitivity and specificity. As a result, pancreatic cancer is usually diagnosed too late in its progression for effective treatment (*e.g.*, surgical removal).[53] In addition, pancreatic cancer spreads widely to distant sites in its early stages and is resistant to most of the treatments available to date.[54] Current diagnostic work-up for pancreatic cancer includes computerized axial tomography (*i.e.*, CT scan), endoscopic retrograde cholangiopancreatography with stent placement, pancreas and liver biopsy, and diagnostic laparotomy.[54] Unfortunately, there is no simple *in-vitro* diagnostic tool available for the diagnosis of pancreatic cancer.

Firpo et al. have proposed in a series of comprehensive literature studies that a potential marker panel for pancreatic cancer includes 162 proteins and a diagnostic test screening a panel of 7 possible pancreatic cancer markers may reach an accuracy greater than 99% for diagnosis of pancreatic cancer.[55] It has also been reported that screening pancreatic cancer markers in a panel improved diagnostic accuracy over a single marker detection.[56-57] Therefore, a multiplexing diagnostic tool that can routinely screen a panel of biomarkers is needed. Among the many potential pancreatic cancer biomarkers, the strongest includes: osteopontin (OPN) [58]; tissue inhibitor of metalloproteinase 1 (TIMP-1) [59]; carcinoembryonic antigen (CEA)[60]; carbohydrate antigen 19-9 (CA 19-9)[61]; carcinoembryonic antigen-related cell adhesion molecule 1 (CEACAM-1)[62]; and matrix metalloproteinase-7 (MMP-7).[63] These biomarkers are over-expressed in the onset and prognosis of pancreatic cancer,[53, 64] and represent an intriguing set of starting points in the development of solid-phase immunoassays for the early detection of pancreatic cancer.

1.10 Dissertation summary

The following chapters of this dissertation are expansions of the materials discussed above. The main emphases of this dissertation are the synthesis, characterization, and biomolecule conjugation of magnetic labels, and their application in immunoassays for the detection of potential pancreatic cancer markers. Chapter 2 presents a method to encapsulate individual ferrimagnetic zinc ferrite nanocubes using a silica layer. The silica coating of individual magnetic nanocubes is only realized when multiple polyelectrolyte layers are deposited on the nanocubes prior to silica encapsulation in order to reduce strong magnetic interparticle couplings. Chapter 3 discusses the synthesis and magnetic characterization of colloidally assembled zinc ferrite magnetic beads. Since the magnetic properties of magnetic particles are dependent on magnetic interactions as well as other physical properties, this chapter aims to elucidate the difference in magnetic properties between seed particles and colloidally assembled magnetic beads. Chapter 4 focuses mainly on applying the colloidally assembled zinc ferrite magnetic beads to GMR-based immunoassays. The detailed procedures to fabricate magnetic labels are discussed and the performance of in-house magnetic labels is compared to the commercially available magnetic beads. Chapter 5 furthers the work in Chapter 4 through the development and optimization of multiplexed GMR-based immunoassays for the detection of potential pancreatic cancer markers. Furthermore, the efforts to develop multiplex immunoassays in serum, using our GMR sensor and our magnetic labels, are elaborated. In summary, this dissertation describes the efforts for the development of an *in-vitro* diagnostic tool for the early diagnosis of pancreatic cancer based on the usage of magnetic labels and GMR sensors.

1.11 References

(1) Heidelberger, M., *Bacteriol. Rev.* **1939,** *3*, 49.

(2) Heidelberger, M.; Kendall, F. E., *J. Exp. Med.* **1935,** *62*, 467.

(3) Kabat, E. A.; Heidelberger, M., *J. Exp. Med.* **1937,** *66*, 229-250.

(4) Stokinger, H. E.; Heidelberger, M., *J. Exp. Med.* **1937,** *66*, 251-272.

(5) Ekins, R., *Clin. Chim. Acta* **1960,** *5*, 453-459.

(6) Yalow, R. S.; Berson, S. A., *Nature* **1959,** *184*, 1648-1649.

(7) Köhler, G.; Milstein, C., *Nature* **1975,** *256*, 495-497.

(8) Wide, L., Solid Phase Antigen-Antibody Systems. In *Radioimmunoassay Methods*, Kirkham, K. E.; Hunter, W. M., Eds. Churchill Livingstone, Edinburgh: 1971, pp 405-412.

(9) Engvall, E.; Perlmann, P., *Immunochemistry* **1971,** *8*, 871-874.

(10) Hemmila, I., *Applications of Fluorescence in Immunoassays*. Wiley: 1991; p 360.

(11) Kricka, L. J., *Clin. Chem.* **1991,** *37*, 1472-1481.

(12) Wienhausen, G.; DeLuca, M., *Anal. Biochem.* **1982,** *127*, 380-388.

(13) Rissin, D. M.; Kan, C. W.; Campbell, T. G.; Howes, S. C.; Fournier, D. R.; Song, L.; Piech, T.; Patel, P. P.; Chang, L.; Rivnak, A. J., *Nat. Biotechnol.* **2010,** *28*, 595-599.

(14) Dasary, S. S.; Singh, A. K.; Senapati, D.; Yu, H.; Ray, P. C., *J. Am. Chem. Soc.* **2009,** *131*, 13806-13812.

(15) Ni, J.; Lipert, R. J.; Dawson, G. B.; Porter, M. D., *Anal. Chem.* **1999,** *71*, 4903-4908.

(16) Porter, M. D.; Lipert, R. J.; Siperko, L. M.; Wang, G.; Narayanan, R., *Chem. Soc. Rev.* **2008,** *37*, 1001-1011.

(17) Gaster, R. S.; Hall, D. A.; Nielsen, C. H.; Osterfeld, S. J.; Yu, H.; Mach, K. E.; Wilson, R. J.; Murmann, B.; Liao, J. C.; Gambhir, S. S., *Nat. Med.* **2009,** *15*, 1327-1332.

(18) Srinivasan, B.; Li, Y.; Jing, Y.; Xu, Y.; Yao, X.; Xing, C.; Wang, J. P., *Angew.*

Chem. Int. Ed. **2009,** *48*, 2764-2767.

(19) Laurentius, L. B.; Owens, N. A.; Park, J.; Crawford, A. C.; Porter, M. D., *Expert Rev. Mol. Diagn.* **2016,** *16*, 883-895.

(20) Lu, A. H.; Salabas, E. e. L.; Schüth, F., *Angew. Chem. Int. Ed.* **2007,** *46*, 1222-1244.

(21) Kim, Y. I.; Kim, D.; Lee, C. S., *Phys. B* **2003,** *337*, 42-51.

(22) Park, J.; An, K.; Hwang, Y.; Park, J.-G.; Noh, H.-J.; Kim, J.-Y.; Park, J.-H.; Hwang, N.-M.; Hyeon, T., *Nat. Mater.* **2004,** *3*, 891-895.

(23) Giri, S.; Samanta, S.; Maji, S.; Ganguli, S.; Bhaumik, A., *J. Magn. Magn. Mater.* **2005,** *285*, 296-302.

(24) Carpenter, E. E.; Seip, C. T.; O'Connor, C. J., *J. Appl. Phys.* **1999,** *85*, 5184-5186.

(25) Tartaj, P.; del Puerto Morales, M.; Veintemillas-Verdaguer, S.; González-Carreño, T.; Serna, C. J., *J. Phys. D: Appl. Phys.* **2003,** *36*, R182.

(26) Sreeja, V.; Joy, P., *Mater. Res. Bull.* **2007,** *42*, 1570-1576.

(27) Ge, S.; Shi, X.; Sun, K.; Li, C.; Baker Jr, J. R.; Holl, M. M. B.; Orr, B. G., *J. Phys. Chem. C* **2009,** *113*, 13593–13599.

(28) Grass, R. N.; Stark, W. J., *J. Mater. Chem.* **2006,** *16*, 1825-1830.

(29) Cullity, B. D.; Graham, C. D., *Introduction to Magnetic Materials*. John Wiley & Sons: 2011.

(30) Weiss, P., *Comptes Rendus* **1906,** *143*, 1136.

(31) Neel, L., *Ann. Phys* **1948,** *3*, 137-198.

(32) Cornell, R. M.; Schwertmann, U., *The Iron Oxides: Structure, Properties, Reactions, Occurrences and Uses*. John Wiley & Sons: 2003.

(33) Bloch, F., *Z. Phys.* **1932,** *74*, 295-335.

(34) Liu, Y.; Sellmyer, D. J.; Shindo, D., *Handbook of Advanced Magnetic Materials: Vol 1. Nanostructural Effects. Vol 2. Characterization and Simulation. Vol 3. Fabrication and Processing. Vol 4. Properties and Applications*. Springer Science & Business Media: 2008.

(35) Frenkel, J.; Dorfman, J., *Nature* **1930,** *126*, 274-275.

(36) Jun, Y.-w.; Seo, J.-w.; Cheon, J., *Acc. Chem. Res.* **2008,** *41*, 179-189.

(37) Bean, C.; Livingston, J., *J. Appl. Phys.* **1959,** *30*, S120-S129.

(38) Baibich, M. N.; Broto, J. M.; Fert, A.; Van Dau, F. N.; Petroff, F.; Etienne, P.; Creuzet, G.; Friederich, A.; Chazelas, J., *Phys. Rev. Lett.* **1988,** *61*, 2472.

(39) Fert, A., *Rev. Mod. Phys.* **2008,** *80*, 1517.

(40) White, R. L., *IEEE Trans. Magn.* **1992,** *28*, 2482-2487.

(41) Freitas, P.; Ferreira, R.; Cardoso, S.; Cardoso, F., *J. Phys.: Condens. Matter* **2007,** *19*, 165221.

(42) Graham, D.; Ferreira, H.; Bernardo, J.; Freitas, P.; Cabral, J., *J. Appl. Phys.* **2002,** *91*, 7786-7788.

(43) Tondra, M.; Porter, M.; Lipert, R. J., *J. Vac. Sci. Technol., A* **2000,** *18*, 1125-1129.

(44) Gaster, R. S.; Xu, L.; Han, S.-J.; Wilson, R. J.; Hall, D. A.; Osterfeld, S. J.; Yu, H.; Wang, S. X., *Nat. Nanotechnol.* **2011,** *6*, 314-320.

(45) Osterfeld, S. J.; Yu, H.; Gaster, R. S.; Caramuta, S.; Xu, L.; Han, S.-J.; Hall, D. A.; Wilson, R. J.; Sun, S.; White, R. L., *Proc. Natl. Acad. Sci.* **2008,** *105*, 20637-20640.

(46) Gaster, R. S.; Hall, D. A.; Wang, S. X., *Nano Lett.* **2010,** *11*, 2579-2583.

(47) Lee, J.-R.; Bechstein, D. J.; Ooi, C. C.; Patel, A.; Gaster, R. S.; Ng, E.; Gonzalez, L. C.; Wang, S. X., *Nat. Commun.* **2016,** *7*.

(48) Lee, J.-R.; Haddon, D. J.; Wand, H. E.; Price, J. V.; Diep, V. K.; Hall, D. A.; Petri, M.; Baechler, E. C.; Balboni, I. M.; Utz, P. J., *Sci. Rep.* **2016,** *6*, 27623.

(49) Lee, J.-R.; Choi, J.; Shultz, T. O.; Wang, S. X., *Anal. Chem.* **2016,** *88*, 7457-7461.

(50) Siegel, R.; Naishadham, D.; Jemal, A., *CA Cancer J. Clin.* **2012,** *62*, 10-29.

(51) Siegel, R. L.; Miller, K. D.; Jemal, A., *CA Cancer J. Clin.* **2016,** *66*, 7-30.

(52) Chari, S. T.; Kelly, K.; Hollingsworth, M. A.; Thayer, S. P.; Ahlquist, D. A.; Andersen, D. K.; Batra, S. K.; Brentnall, T. A.; Canto, M.; Cleeter, D. F., *Pancreas* **2015,** *44*, 693.

(53) Poruk, K. E.; Firpo, M. A.; Adler, D. G.; Mulvihill, S. J., *Ann. Surg.* **2013,** *257*, 17.

(54) Li, D.; Xie, K.; Wolff, R.; Abbruzzese, J. L., *The Lancet* **2004,** *363*, 1049-1057.

(55) Firpo, M. A.; Boucher, K. M.; Mulvihill, S. J., *Theor. Biol. Med. Modell.* **2014,** *11*, 1.

(56) Firpo, M. A.; Gay, D. Z.; Granger, S. R.; Scaife, C. L.; DiSario, J. A.; Boucher, K. M.; Mulvihill, S. J., *World J. Surg.* **2009,** *33*, 716-722.

(57) Zhou, W.; Sokoll, L. J.; Bruzek, D. J.; Zhang, L.; Velculescu, V. E.; Goldin, S. B.; Hruban, R. H.; Kern, S. E.; Hamilton, S. R.; Chan, D. W., *Cancer Epidemiol. Biomarkers Prev.* **1998,** *7*, 109-112.

(58) Koopmann, J.; Fedarko, N. S.; Jain, A.; Maitra, A.; Iacobuzio-Donahue, C.; Rahman, A.; Hruban, R. H.; Yeo, C. J.; Goggins, M., *Cancer Epidemiol. Biomarkers Prev.* **2004,** *13*, 487-491.

(59) Bramhall, S. R.; Neoptolemos, J. P.; Stamp, G. W.; Lemoine, N. R., *J. Pathol.* **1997,** *182*, 347-355.

(60) Steinberg, W. M.; Gelfand, R.; Anderson, K. K.; Glenn, J.; Kurtzman, S. H.; Sindelar, W. F.; Toskes, P. P., *Gastroenterology* **1986,** *90*, 343-349.

(61) E Poruk, K.; Z Gay, D.; Brown, K.; D Mulvihill, J.; M Boucher, K.; L Scaife, C.; A Firpo, M.; J Mulvihill, S., *Curr. Mol. Med.* **2013,** *13*, 340-351.

(62) Ballehaninna, U. K.; Chamberlain, R. S., *Tumor Biol.* **2013,** *34*, 3279-3292.

(63) Fukuda, A.; Wang, S. C.; Morris, J. P.; Folias, A. E.; Liou, A.; Kim, G. E.; Akira, S.; Boucher, K. M.; Firpo, M. A.; Mulvihill, S. J., *Cancer Cell* **2011,** *19*, 441-455.

(64) Poruk, K. E.; Firpo, M. A.; Scaife, C. L.; Adler, D. G.; Emerson, L. L.; Boucher, K. M.; Mulvihill, S. J., *Pancreas* **2013,** *42*, 193.

CHAPTER 2

SILICA ENCAPSULATION OF FERRIMAGNETIC ZINC FERRITE NANOCUBES ENABLED BY LAYER-BY-LAYER POLYELECTROLYTE DEPOSITION

2.1 Introduction

The synthesis and preparation of magnetic nanoparticles (MNPs) with large magnetic dipole moments, ***m***, have been gaining traction in a variety of technologies, including those focused on magnetic recording media,[1] biological[2] and environmental separations,[3] chemical catalysis,[4] nanomedicine,[5] ferrofluid applications,[6] magnetic resonance imaging (MRI) contrast reagents,[7] and biosensors.[8, 9] However, one of the shortcomings of high ***m*** MNPs is their tendency to spontaneously aggregate. Approaches to prevent MNP aggregation include creating a shell around the MNPs,[10] fabricating synthetic antiferromagnetic nanoparticles,[3, 11] or decreasing the MNP size until

superparamagnetic behavior is observed.[12] Superparamagnetism (at 298 K) occurs in single-domain ferro- and ferrimagnetic nanoparticles of sufficiently small size that their magnetic dipole undergoes random thermal fluctuations in the absence of an external magnetic field (***H***); this situation results in the absence of an observable moment.[13] Despite the advantage of zero residual magnetism afforded by superparamagnetic nanoparticles (SPMNPs), the diminution in MNP size results in a commensurate decrease in ***m***, which can limit utility. For example, the signal-to-noise ratio of a magnetic biosensor is proportional to ***m***, and MNPs with large ***m*** are generally required in magnetic drug delivery and cell separation. SPMNPs are also not suitable for permanent magnetic storage media, which require ferro- or ferrimagnetic nanoparticles (FMNPs) with nonzero coercivity ($\boldsymbol{H_C}$) and remanent magnetization ($\boldsymbol{M_R}$).

In addition to tailoring MNP size to counteract magnetic interparticle attraction, several particle-coating strategies have been used with similar results. Simple surface-ligand exchange has been used to effectively stabilize SPMNP dispersions.[14-16] However, ligand-exchange does not mitigate the aggregation of FMNPs. In these cases, polymeric coatings have been employed to avoid magnetically induced aggregation during and after synthesis. The charged or polar groups of the polymer stabilize moderate ***m*** MNPs via electrostatic repulsion and the physical coating limits particle-particle approach distance.[17-19] In instances of large ***m*** FMNPs, extraordinarily strong electrostatic repulsion or an increase in the MNP-MNP closest-approach induced by thicker polymeric coatings is necessary to produce a stable FMNP colloid.[17-19] The effectiveness of these polymeric coatings, however, is generally limited to FMNPs smaller than 50 nm in size.

Another means to overcome magnetic-induced aggregation is to encapsulate MNPs

in a shell of gold, graphite, or silica creating a core-shell architecture (core@shell).[15] This form of encapsulation has several advantages over other coating strategies: 1) it can increase the MNP-MNP closest approach distance thereby reducing interparticle interactions; 2) it protects the magnetic core from dissolution; and 3) it can be modified with molecular recognition elements (*e.g.*, antibodies, nucleic acids) by established linking chemistries. Among those coating materials, silica is biocompatible and can further enhance colloidal stability in aqueous media since the terminal hydroxyl groups are ionized at the pH of physiologically relevant matrices.[20] Although the application of silica coatings on small FMNPs has been reported,[1] there are few reports detailing the encapsulation of large FMNPs with high $\boldsymbol{m}$. In these scenarios, silica encapsulation often leads to aggregates of particles embedded in a silica matrix.[21-23] However, Kolhatkar et al. have reported that FeCo ferromagnetic nanocubes (>150 nm in size) with a high saturation magnetization, $\boldsymbol{M_s}$, could be coated with silica after stabilizing with a layer of polyvinylpyrrolidone (PVP),[10] and Marcelo et al. described the stabilization of hydrophobic Fe_3O_4 ferrimagnetic nanocubes (>70 nm in size) in water by coating the particles with silica under sonication after citric acid ligand-exchange.[24] While it appears that these intermediary coating procedures were sufficient to stabilize the particles prior to silica encapsulation, it is not clear that a high yield of single-core, silica-coated MNPs was realized. In our experience, these methods are not effective in stabilizing >100 nm zinc ferrite nanocubes with $\boldsymbol{M_s}$ ~100 emu/g.

Herein, we report a novel method for the production of discrete, silica-coated ferrimagnetic zinc ferrite nanocubes (ZFNCs). High-moment ($\boldsymbol{m}$~10-13 emu/particle at $\boldsymbol{H}$ = 150 Oe) ZFNC seeds (~130 nm) were first prepared via thermal decomposition in benzyl

ether and oleic acid. The resulting hydrophobic oleic acid surface-molecules of as-synthesized ZFNCs were replaced with a hydrophilic ligand and transferred to aqueous media. To further increase the suspension stability of the seed ZFNCs, a total of six layers of two alternating polyelectrolytes, polyallylamine (PAAm) and polystyrene sulfonate (PSS), were deposited by a layer-by-layer (LbL) process. The LbL-stabilized ZFNCs were then encapsulated with silica, resulting in primarily discrete silica-coated ZFNC (ZFNC@SiO_2) particles. The ZFNC@SiO_2 particles were characterized by electron microscopy, energy dispersive X-ray spectroscopy, powder X-ray diffraction, dynamic light scattering, infrared spectroscopy, and vibrating sample magnetometry.

2.2 Experimental Section

2.2.1 Materials

Iron acetylacetonate ($Fe(acac)_3$, 99%), zinc acetyl-acetonate ($Zn(acac)_2$, 95%), benzyl ether (99%), tetraethyl orthosilicate (TEOS, 95%), dimercaptosuccinic acid (DMSA, 99%) and poly(sodium-p-styrene sulfonate) (PSS, linear, M_w ~70,000 g/mol) were purchased from Acros organics (USA). Polyethyleneimine (PEI, branched, M_w ~25,000 g/mol) and citric acid (CA, 99%) were received from Sigma-Aldrich (USA). Polyallylamine hydrochloride (PAAm, linear, 120,000<M_w<200,000 g/mol), oleic acid (90%) and ammonium hydroxide (NH_4OH, 30%) were purchased from Alfa Aesar (USA). Ethanol (EtOH, 200 proof) was acquired from Decon Lab (USA). Dimethyl sulfoxide (DMSO, 99%) and toluene (99%) were obtained from Fisher Scientific (USA). All chemicals were used as-received without further purification.

2.2.2 Synthesis of Magnetic Nanoparticles

The synthesis of cubic ferrimagnetic nanoparticles was adapted from the procedure of Noh et al.[25] Typically, 0.353 g $Fe(acac)_3$ and 0.395 g $Zn(acac)_2$ were added to a mixture of 1.2 mL oleic acid and 10.0 mL benzyl ether. This solution was heated under nitrogen at a rate of 15 ˚C/min to 290 ˚C and then refluxed for 30 min. After cooling to room temperature, 20 mL of EtOH was added to precipitate cubic zinc ferrite particles. The sample was then centrifuged at 10,190×*g* for 10 min and the supernatant was discarded. This washing procedure was repeated two more times. The MNPs were finally resuspended in 10 mL of toluene.

2.2.3 Ligand-exchange of Magnetic Nanoparticles

Surface functionalization with a hydrophilic exchange ligand (*i.e.*, CA, DMSA, and PEI) was used to transform the as-prepared hydrophobic ZFNCs to a hydrophilic state for subsequent suspension in water. A 10 mL aliquot of ligand solution (ligand concentration ~70 mg/mL in DMSO) was added to the MNP suspension, followed by a 3-h sonication at 60 ˚C and agitation on a rocking table for 16 h. The hydrophilic, ligand-coated MNPs were next washed three times with 10 mL EtOH and resuspended in 18.2 MΩ-cm deionized water (DI H_2O). The final concentration of the ligand-exchanged MNPs was ~5 mg/mL.

2.2.4 Layer-by-layer (LbL) Deposition of Polyelectrolytes

Prior to LbL deposition, 1.0 mL of the PEI-coated zinc ferrite particles (~5 mg) was diluted to 10 mL with DI H_2O. This step was followed by the addition of 5.0 mL aqueous PSS (10 mg/mL) and a 1-h sonication. Next, the excess PSS was centrifuged (10,190×*g*,

10 min) and the supernatant was removed. The MNPs were then resuspended in 10 mL DI H_2O and a 200 μL aliquot was removed for characterization. This process was repeated two more times. A subsequent layer of PAAm was formed using the same procedure with an aqueous solution of PAAm (10 mg/mL). These two deposition steps were repeated until the desired number of polyelectrolyte layers were deposited; typically six polyelectrolyte layers were deposited prior to silica coating. The terminal PAAm layer possessed a net positive surface charge ($-NH_3^+$) in DI H_2O (pH = 6.5). The resulting MNPs were resuspended in DI H_2O to a final concentration of ~5 mg/mL.

2.2.5 Silica Coating

Silica was deposited on the polyelectrolyte-coated zinc ferrite seed particles by a modified Stöber method.[26] Briefly, 1.0 mL of the LbL-coated MNP suspension (~5 mg in DI H_2O) was added to 10 mL EtOH, followed by the sequential addition of 0.65 mL DI H_2O and 1.0 mL TEOS solution (25 μL/mL in EtOH) at room temperature. The magnetic suspension was sonicated for 90 min after which 0.98 mL NH_4OH was added drop-wise to the suspension with continued sonication. Then, another 1.0 mL of TEOS solution was added drop-wise, which was followed by a 90-min sonication, and then agitation on a rocker plate for 18 h. The silica-coated MNPs were isolated after three centrifugation (10,190×*g*, 10 min) steps in EtOH and a final resuspension in 10 mL DI H_2O. The overall process is depicted in Figure 2.1.

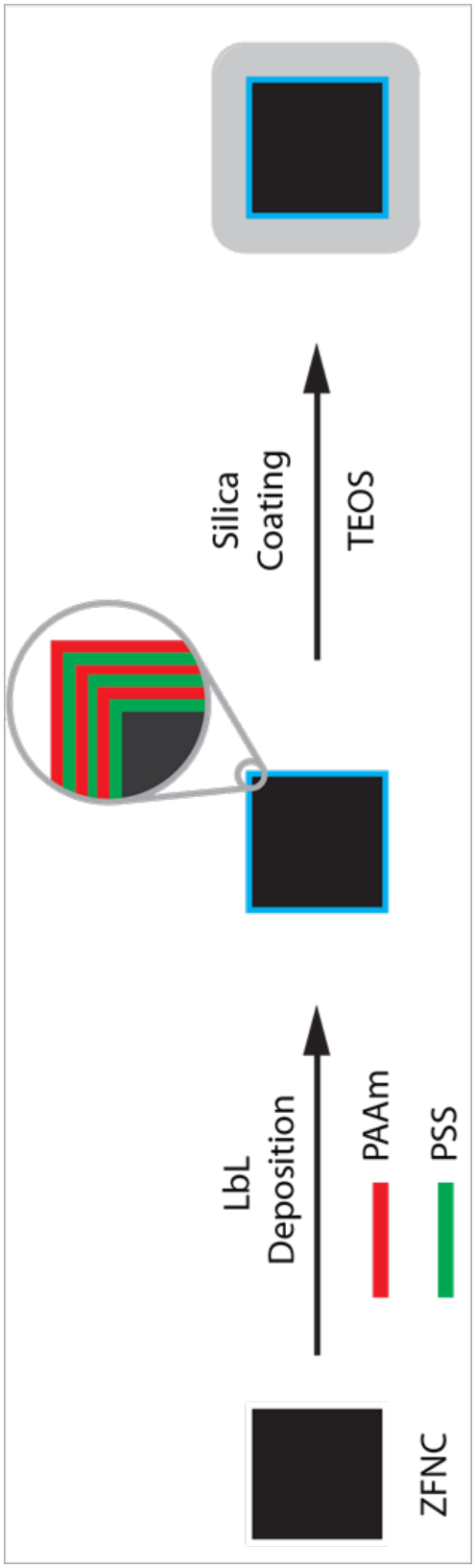

Figure 2.1 Synthesis of core-shell ZFNC@SiO_2 particles.

2.2.6 Electron Microscopy

Field-emission scanning electron microscopy (FESEM) was performed with a Hitachi S-4800 equipped with an energy dispersive X-ray (EDX, INCA, Oxford Instruments) spectroscopy module. In general, MNP samples for imaging and EDX analysis were prepared by pipetting 20 μL aqueous particle suspension onto a 1×1 cm^2 silicon chip that was allowed to dry at ambient temperature. Images were obtained at an acceleration voltage of 15 kV.

For transmission electron microscopy (TEM), a JEM-2800 S/TEM instrument (JEOL, Japan) was used at 200 kV with the magnetic samples dropcast on a 3-mm carbon-coated copper grid. EDX mapping data was collected with a 1 nm probe at a 512×512 pixel density, ~0.5 nm/pixel.

2.2.7 X-ray Diffraction (XRD) Analysis

The crystallinity of the MNPs was determined by powder X-ray diffraction (XRD, Rigaku, D/max-2200V, Japan). XRD was carried out with Cu Kα radiation (λ = 0.154059 nm) and operated at 40 kV and 30 mA. The diffractograms were obtained with a 2θ step of 0.02˚ at 0.5 s/step from 15˚-100˚. Three sample libraries, the International Centre for Diffraction Data (ICDD), the RUFF Project Database,[27] and the National Bureau of Standards X-ray diffraction powder pattern monograph,[28] were used for identification of samples.

2.2.8 Infrared (IR) Spectroscopy

IR transmission spectra were collected using a Nicolet Magna 850 Fourier transform IR spectrometer equipped with a liquid nitrogen-cooled mercury cadmium telluride detector. Spectra were collected in a nitrogen atmosphere using 512 scans at a resolution of 0.198 cm^{-1} with p-polarized light. The MNP samples were prepared as 1% particle (w/w) dispersions in KBr.

2.2.9 Dynamic Light Scattering (DLS)

The zeta (ζ)-potential and hydrodynamic sizes of particle samples were measured using a Zetasizer Nano (Malvern Instruments, U.K.) with a disposable folded capillary cell. The particles were diluted to 0.1 wt % in DI H_2O. Nanoparticle suspensions were sonicated for 2 min before being injected into the cell and left to equilibrate for 2 min prior to measurement. The specific conditions for DLS measurement are described in the Supporting Information.

2.2.10 Vibrating Sample Magnetometry (VSM)

Magnetic hysteresis curves, isothermal remanent magnetization (IRM), and dc demagnetization (DCD) remanence measurements were carried out using a vibrating sample magnetometer (VSM EZ7, MicroSense, Lowell, MA) operated at 298 K. For the measurements, MNPs were mounted on a piece of Kapton tape which was folded in half and gently compressed in a pellet press to fix the particles to the tape and remove trapped air. Another piece of the tape without the MNPs served as the blank. The signal of the blank was subtracted from the sample signal. The particular procedures for IRM and DCD

measurements are provided in the Supporting Information.

Throughout this work, we have adopted the convention of using the term magnetization, $\boldsymbol{M}$, interchangeably with mass magnetic moment, $\boldsymbol{\sigma}$. However, by definition, $\boldsymbol{M}$ has units of emu/cm^3 and $\boldsymbol{\sigma}$ has units of emu/g.

2.3 Results and Discussion

Monodispersed ZFNC seed particles were synthesized by thermal decomposition of zinc and iron acetylacetonates.[25] Shown in Figure 2.2A is a representative SEM image of the as-synthesized ZFNCs and their size distribution. These cube-shaped particles have an average edge length of ~130 nm and their faces appear rough, which is usually found with particles larger than 100 nm and is most likely due to crystalline defects and step edges. The as-synthesized particles are composed of Fe, O, and Zn and have an empirical formula of $[Zn_{0.41}Fe_{0.59}]Fe_2O_4$ determined by EDX (Figure A.1). The X-ray powder diffractogram for the ZFNCs (Figure A.2) shows that the particles are crystalline with characteristic diffraction peaks of magnetite (Fe_3O_4, ICDD No. 01-086-0510 and RRUFF Database No. R080025) and zinc ferrite ($ZnFe_2O_4$, NBS Monograph[29] and RRUFF Database No. R070137).

The ZFNCs then underwent a ligand-exchange process to replace the hydrophobic surface group, oleic acid,[30] with a hydrophilic species. We chose to study CA, DMSA, and branched PEI based on their previously demonstrated effectiveness as ligand-exchange agents.[31] The ζ-potential values, which are an indication of surface charge and, therefore, colloidal stability, measured for the CA-, DMSA-, and PEI-coated ZFNCs were –6.5 ± 3.6, –15.9 ± 4.6, and +52.7 ± 4.4 mV, respectively, in DI H_2O. The negative values for the first

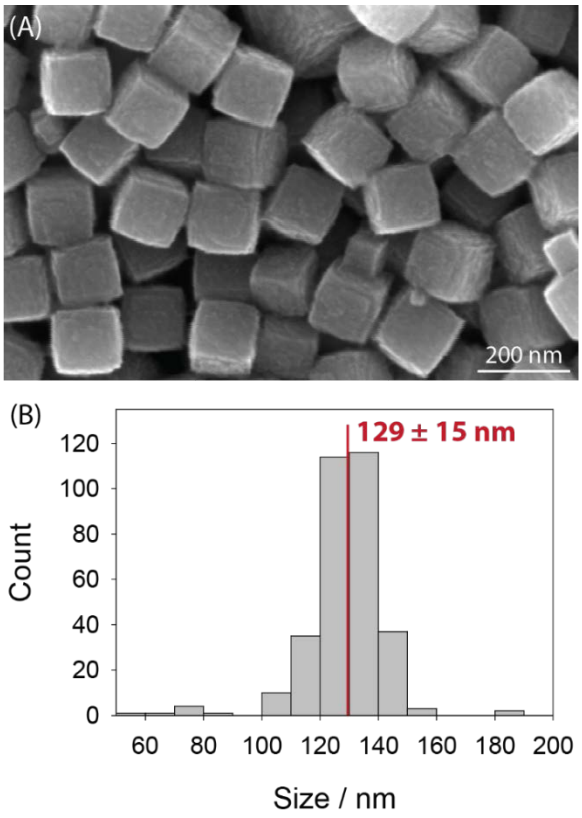

Figure 2.2 (A) Representative scanning electron micrograph of as-synthesized ZFNCs. (B) Histogram of the edge length of as-synthesized ZFNCs.

two systems are consistent with the deprotonation of the carboxylic acid groups of CA and DMSA, whereas the positive value for the third system follows the expectation for protonation of the PEI amine groups. Of the three ligand-exchanged ZFNCs, only the PEI-coated ZFNCs appear to have an absolute ζ-potential indicative of stable colloids ($|\zeta| > 30$ mV). Indeed, when the CA- and DMSA-coated ZFNCs were suspended in DI H_2O, they precipitated within 10 min. The PEI-coated ZFNCs, however, remained suspended in DI H_2O for a few hours. The colloidal stability due to PEI, compared to CA and DMSA, is believed to arise from: 1) the multivalent adsorption of the polymer, leading to stronger particle-polymer interactions compared to the adsorption of

mono- or divalent ligands,[32, 33] and 2) an increase in MNP-MNP separation due to PEI-induced steric hindrance and electrostatic repulsion of the profuse protonated amine groups. We note that the ligand-exchange procedures appeared to have no effect on the morphology of seed ZNFCs, which was investigated by SEM.

Once the ZFNCs were stabilized with PEI and effectively dispersed in aqueous media, silica encapsulation was attempted to create a potentially more suitable species for bioanalytical applications. Coating nanoparticles that possess a nonzero remanent magnetization with silica or metals can be problematic due to their tendency to aggregate, which is brought on by strong interparticle magnetic dipole-dipole interactions; indeed, there are only a few reports detailing the successful encapsulation of these particles.[10, 24, 33] Shown in Figure 2.3 are SEM micrographs of the CA-, DMSA-, and PEI-modified ZFNCs after silica coating. While a one-step ligand-exchange successfully altered the surface properties of our ZFNCs (*i.e.*, from hydrophobic to hydrophilic), the particles tended to aggregate into linear chains during silica encapsulation. Individual ZFNC@SiO_2 particles were not observed; rather, linear aggregates of ZFNCs embedded in a silica matrix were formed. It is important to note that the high ζ-potential of the PEI-coated ZFNCs, indicating strong electrostatic repulsion between PEI-modified ZFNCs, did not prevent the seed ZFNCs from aggregating during the silica coating procedure.

Linear or face-to-face assemblies of different MNPs are frequently observed in dispersions or silica matrices.[34-36] The mechanism of MNP aggregation can involve several phenomena including Brownian motion (thermal energy), magnetostatic and electrostatic forces, and van der Waals interactions.[37] We believe that the linear arrangement of ZFNCs arises primarily from interparticle magnetic dipole-dipole interactions. In other words, the

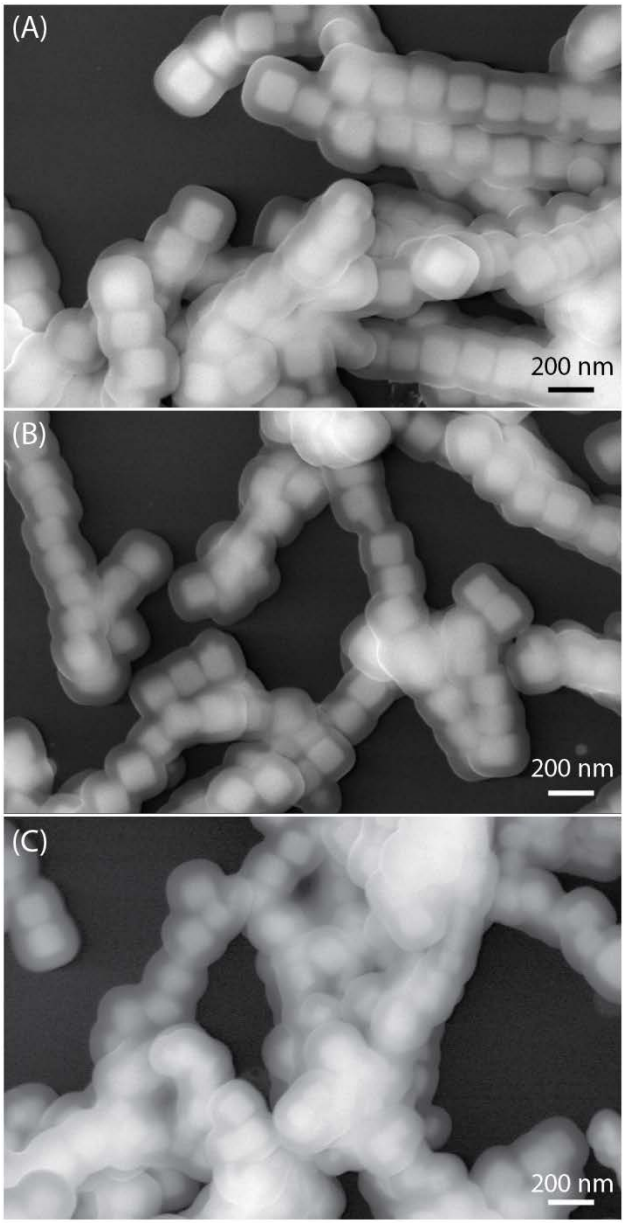

Figure 2.3 Scanning electron micrographs of the linear arrangement of ZFNCs in silica matrices. The as-synthesized ZFNCs were ligand-exchanged with (A) CA, (B) DMSA, and (C) branched PEI before the silica coating step.

magnetic dipole-dipole interaction between the nanocubes leading to the observed anisotropic structures (*e.g.*, linear chains, flux-closure rings, etc.) is stronger than Brownian forces, van der Waals interactions, or electrostatic forces that are typically responsible for isotropic aggregation.[38]

To prevent linear chain formation of the ZFNC seeds, a series of polyelectrolyte layers were applied to the seed ZFNCs using an LbL technique. The LbL deposition of polyelectrolytes is a versatile method used to create robust, polymeric multilayer structures.[39-42] In principle, fabrication of polyelectrolyte multilayers utilizes electrostatic interactions between oppositely charged polyelectrolytes, which enables cyclic deposition of oppositely charged polyelectrolytes. As a consequence, LbL deposition enables one not only to control the thickness of multilayers in nanometer scale, but also to take advantage of the polyelectrolyte charge. Of the potential polyelectrolytes, we opted to assess the utility of PSS and PAAm, which contain sulfonate and amine groups, respectively. As the PEI-coated seed ZFNCs were positively charged, PSS was deposited as the first polyelectrolyte, followed by the deposition of PAAm. We repeated this cycle until six polyelectrolyte layers were deposited. The deposition of each polyelectrolyte layer was characterized by ζ-potential and IR (Figure 2.4). The charge reversal between PSS layers (odd numbered) and PAAm terminal layers (even numbered) in Figure 2.4A indicates that the sequential deposition of polyelectrolytes was successful. The IR spectra shown in Figure 2.4B follow the stepwise formation of ZNFC@SiO_2, starting with the PEI-coated ZFNCs (black line).

All three spectra have strong bands around 580 cm^{-1}, which are associated with Fe-O lattice vibrations.[43] The features at 1560 and 1630 cm^{-1} in the PEI-coated ZFNC

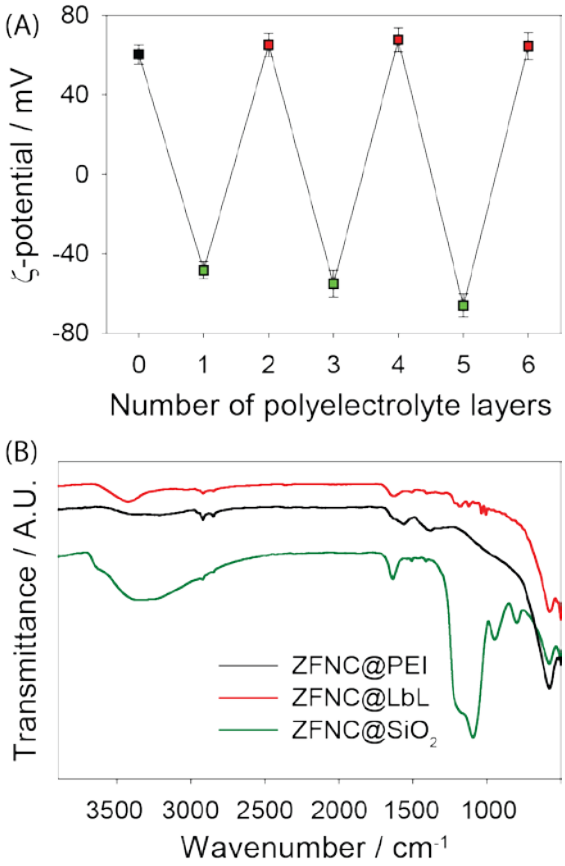

Figure 2.4 (A) ζ-potential measurements showing surface charge reversal of the ZFNC seeds in the course of LbL deposition of PSS (odd layer number) and PAAm (even layer number). (B) IR spectra of the particles after PEI ligand-exchange, LbL deposition of PSS and PAAm, and silica encapsulation. Note that the particle sample of ZFNC@LbL used in the IR study had six polyelectrolyte layers.

sample are due to the NH and NH_2 deformation in PEI, and the broad band from 3200 to 3425 cm^{-1} is assigned to the N-H stretching vibration.[44] These spectral features confirm the presence of PEI after ligand-exchange. After depositing the six polyelectrolyte layers (red line), sharp bands at 1007 and 1037 cm^{-1} are observed and attributed to the S=O sy mmetrical stretching vibration and an aromatic in-plane vibration of PSS, respectively.[45] There is also a band around 1630 cm^{-1}, which is a bending mode of the primary amine in the PAAm layers.[46] The progression of spectral features support the successful deposition

of PSS and PAAm polyelectrolyte layers on the ZFNC@PEI particles.

Discrete ZFNC@SiO_2 particles were subsequently formed using a modified Stöber procedure. The thickness of the silica layer was ~30 nm and the particles retained their cubic morphology (Figure 2.5). The discrete nature of the ZFNC@SiO_2 particles is observed by noting the distance between particles is twice the thickness of the silica shell. The IR spectrum of the silica-coated ZFNCs (green line in Figure 2.4B) shows a broad, strong band at 1100 cm^{-1}, which arises from the asymmetric vibration of Si-O bonds. Strong asymmetric and symmetric vibrations of Si-OH and Si-O are observed at 950 and 795 cm^{-1}, respectively.[47] A broad band at 3500 cm^{-1} and a slightly weaker band around 1600 cm^{-1} are attributed to O-H stretching and bending vibrations, respectively; these two bands are likely from surface hydroxyl (–OH) groups of silica and adsorbed water.[48] The measured ζ-potential of ZFNC@SiO_2 particles in DI H_2O was –63.1 ± 7.0 mV, indicating that the surface (–OH) groups are deprotonated, which is consistent with pI of silica (~pH

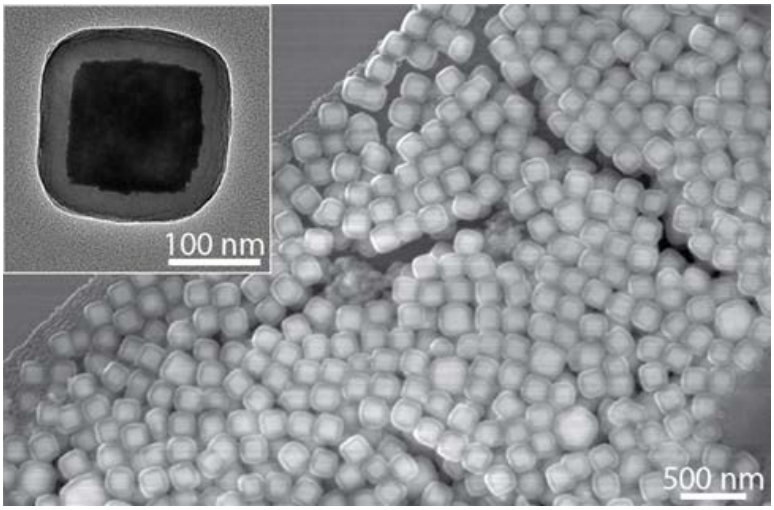

Figure 2.5 Electron micrograph of the ZFNC@SiO_2 particles assisted via LbL deposition. The discrete nature of the ZFNC@SiO_2 particles is shown in the representative SEM image and bright field TEM image (inset).

2).[20] It should be noted that the XRD peaks of the silica-coated ZNFCs closely resemble the Bragg reflections of the seed ZFNCs (Figure A.2), indicating that the silica shell is amorphous and the crystallinity of the magnetic core is not affected by encapsulation.

The particle size progression of the PEI-, polyelectrolyte-, and silica-coated ZFNCs was also followed by DLS (Figure A.3) and compared to the SEM micrograph analysis (Table A.1). The average size of particle increases with synthesis step. The hydrodynamic size based on intensity distribution ($\boldsymbol{D_{h,int}}$) of the PEI-coated ZFNCs was ~225 nm prior to LbL deposition. After the sequential deposition of six polyelectrolyte layers and silica coating, $\boldsymbol{D_{h,int}}$ increased to 297 nm and 360 nm, respectively. Considering a sphere is the only object whose size can be correctly described by a single dimension in DLS, the $\boldsymbol{D_{h,int}}$ of a cube is roughly interpreted as the maximum corner-to-corner dimension of that cube ($\sqrt{3}$ longer than a cube edge).[49] Therefore, the hydrodynamic size intensity distributions of the ZFNC@SiO_2 from the DLS measurements are consistent with those determined from SEM (Table A.1).

EDX mapping analysis acquired during the course of TEM imaging provided chemical composition and elemental distribution information of discrete ZFNC@SiO_2 particles. Representative results are presented in Figure 2.6. The images indicate that Fe, Zn, and O are distributed throughout the particle core and the distribution of Si and S is weighted towards the encapsulating shell. It is important to note that polyelectrolyte layers deposited prior to silica encapsulation persist after silica coating. The S signal is presumed to be due to the presence of PSS between the core and the SiO_2 shell, which is clearly observed in Figure 2.6A — the composite of grayscale, Fe, Si, and S. The ability to capture intermediary components between the core and silica shell suggests that much smaller

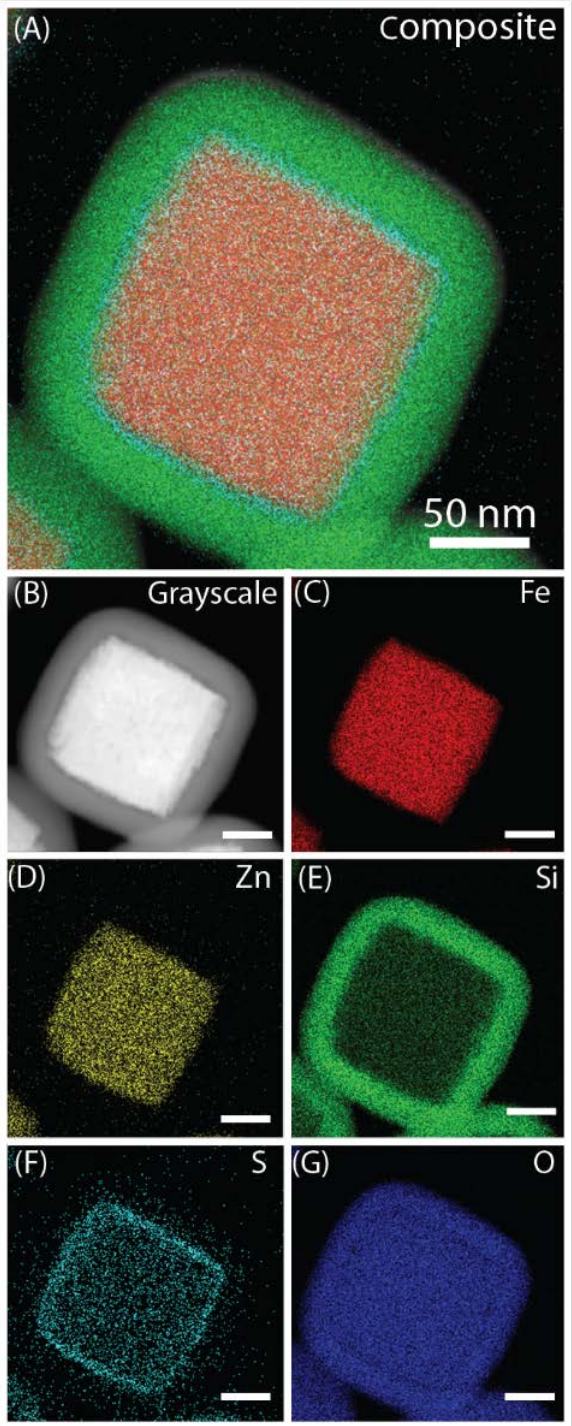

Figure 2.6 EDX images depicting elemental distribution of (C) Fe, (D) Zn, (E) Si, (F) S, and (G) O. The figure shown in (A) is a composite of the grayscale TEM image (B) and Fe, Si, and S. Scale bar in each image is 50 nm.

nanoparticles, fluorophores, or other materials could potentially be incorporated within the polyelectrolyte layers, creating multifunctional silica-coated ferrimagnetic nanoparticles. For example, by incorporating quantum dots within the multilaye r polyelectrolyte structure, further development of multi-modal imaging and theranostic agents could be realized.[50]

To delineate the effect that the number of polyelectrolyte layers has on the formation of ZFNC@SiO_2 particles, we attempted to silica coat the seed particles with different numbers of polyelectrolyte layers. The number of polyelectrolyte layers is a critical parameter to keep the ferrimagnetic ZFNCs separated during the silica coating process. Shown in Figure 2.7A-D are silica-coated ZFNCs with zero, two, four, and six polyelectrolyte layers respectively. In general, as the number of polyelectrolyte coatings increases, the tendency to form linear chains or aggregates during silica encapsulation decreases. Very few single-core, ZFNC@SiO_2 particles were obtained when the seed ZFNCs were coated with only 0 or 2 polyelectrolyte layers. The seed ZFNCs with four polyelectrolyte layers demonstrated few single-core ZFNC@SiO_2 particles, and large aggregates still dominate. Once the ZFNCs are encapsulated with six or more polyelectrolyte layers, discrete ZFNC@SiO_2 particles are clearly evident. The SEM images in Figure 2.7D and Figure 2.5 show the gap distance between two seed particles is roughly twice as large as the silica layer thickness, indicative of discrete ZFNC@SiO_2. Furthermore, the DLS size distributions of the different ZFNC@SiO_2 samples are in good agreement with the SEM data in Figure 2.6. Only the silica-coated ZFNCs with six polyelectrolyte layers showed one prominent $\boldsymbol{D_{h,int}}$ peak (Figure A.4). As expected, the average hydrodynamic size of the ZFNC@SiO_2 particles decreases with increasing polyelectrolyte

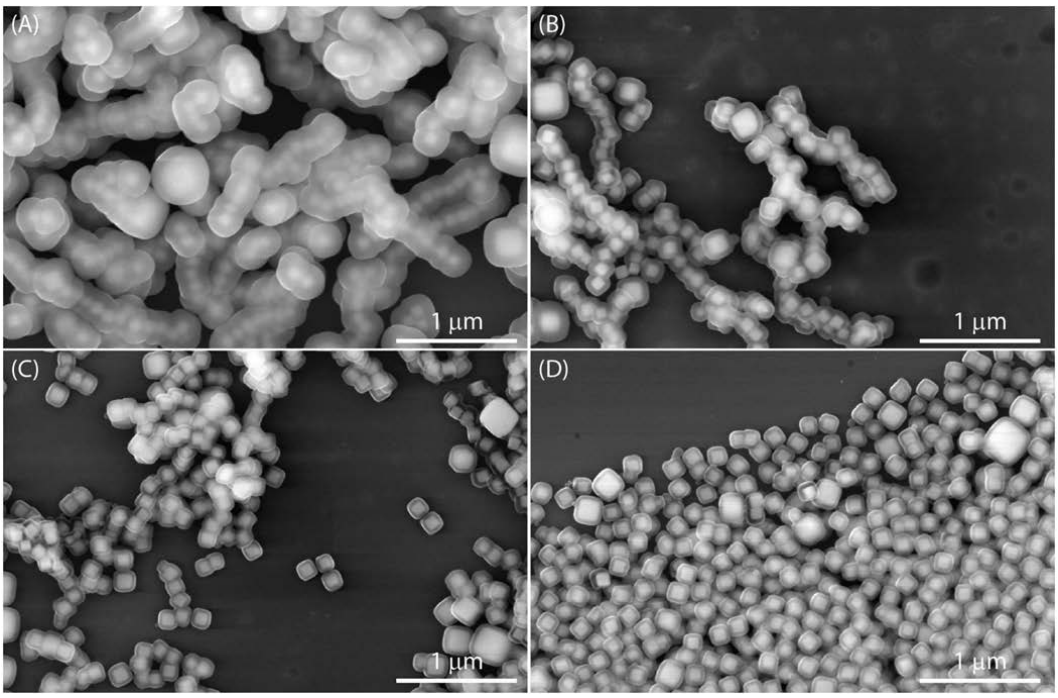

Figure 2.7 SEM images of silica-coated ZFNCs. The seed ZFNCs had different numbers of polyelectrolyte layers prior to silica encapsulation: (A) 0, (B) 2, (C) 4, and (D) 6 layers.

layer; a testament to aggregation remediation. The colloidal stability of the ZFNC@SiO_2 particles also increases with the number of polyelectrolyte layers applied. The ZFNC@SiO_2 particles with six polyelectrolyte layers remained suspended for over 12 h in DI H_2O. However, the ZFNC@SiO_2 particles with 0 and 2 polyelectrolyte layers sedimented in less than 30 min in DI H_2O.

Together, the DLS and SEM data indicate that at least six polyelectrolyte layers are essential to stabilize the seed particles and ensure successful fabrication of discrete ZFNCs@SiO_2 particles. We believe that the success of LbL stabilization is due to an increase in the closest approach distance between the ZFNCs, and therefore a reduction in magnetic dipole-dipole interaction, and electrostatic repulsion brought on by the charge of the outermost layer of the LbL-coated seed ZFNCs.

To understand the ramifications that the coatings have on the resulting magnetic properties of the ZFNCs, a series of magnetometry experiments were performed. Shown in Figure 2.8 are representative magnetization curves of PEI- (black), LbL-coated ZFNCs(red), and ZFNC@SiO_2 (green). The measured values of $\boldsymbol{M_r}$ and $\boldsymbol{H_c}$ for the PEI-coated ZFNCs are 16.8 emu/g and 50.5 Oe, respectively, indicating that the ZFNCs are ferrimagnetic at room temperature. The value for $\boldsymbol{M_s}$ (this is the quotient of the measured sample moment to the total mass of particles in the sample) of the PEI-coated ZFNCs is 98.4 emu/g at 298 K. This value is higher than the reported $\boldsymbol{M_s}$ of magnetite nanoparticles (80-85 emu/g),[33, 51] which is consistent with the $\boldsymbol{M_s}$ enhancement of Zn-doped Fe_3O_4 nanoparticles.[52, 53] The magnetic moment of one ZFNCs (Table A.2) is estimated at 10^{-13} emu/particle ($\boldsymbol{H}$ = 150 Oe) and 10^{-12} emu/particle at fields sufficient to saturate the sample (15,000 Oe). These values are also higher than that reported for Fe_3O_4 and other commercial magnetic particles.[10, 54] However, $\boldsymbol{M_s}$ decreases with each coating step: 82.4

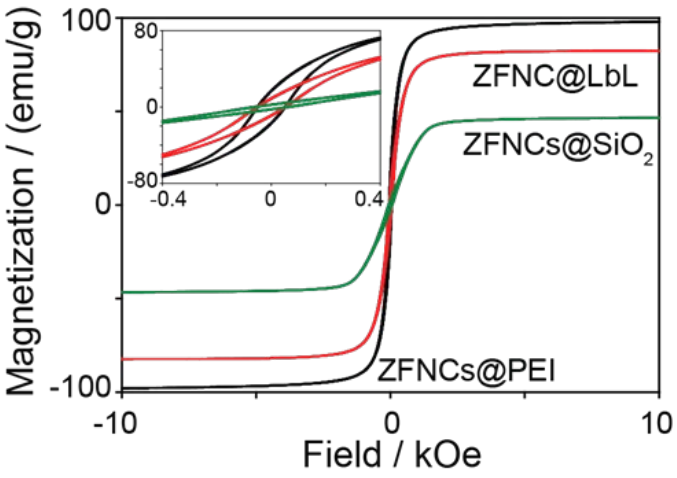

Figure 2.8 Hysteresis curves of the ZFNCs with different coatings; PEI (black), LbL (red), and silica (green). $\boldsymbol{H_c}$ increases (inset) with coating step: 50.5, 51.8, and 61.6 Oe.

emu/g after six polyelectrolyte coatings and 46.9 emu/g after silica coating. This decrease is due to the increased mass of the non-magnetic coatings. Despite the decrease of $\boldsymbol{M_s}$ after silica coating, both the ZFNCs and ZFNC@SiO_2 particles are easily collected from a 10-mL suspension using a 1-cm^3 neodymium magnet (~4,000 Gauss) in 10 s or 20 s, respectively. Commensurate with the decrease in $\boldsymbol{M_s}$, $\boldsymbol{H_c}$ increases slightly from 50.5 Oe to 51.8 Oe to 61.6 Oe when coated with PEI, LbL polyelectrolytes, and silica, respectively. We believe that the increase in $\boldsymbol{H_c}$ is a result of decreased magnetic dipole coupling. The polyelectrolyte and silica shells physically separate the core ZFNCs, which causes a reduction of the interaction field (magnetic dipole interactions decay as the cube of interparticle separation),[55] leading to an increase in $\boldsymbol{H_c}$. Morales et al. observed a similar coercivity enhancement when γ-Fe_2O_3 MNPs were dispersed in a silica matrix.[56] This observation is in agreement with the report by Che et al., in which they demonstrated that magnetization reversal is assisted by strong dipole coupling, which results in a decrease in $\boldsymbol{H_c}$.[57]

Particle-particle interactions can be assessed by remanence techniques (see Supporting Information). The quantitative validity of these approaches depends on several assumptions: the particles are assumed to be single-domain ferromagnetic particles with uniaxial anisotropy. Given the size of our ZFNPs, we anticipate the particles are comprised of multiple domains. However, remanence techniques, which are based on comparing the IRM curve to the DCD curve, can still provide qualitative interaction information in systems that deviate from the basic assumptions.

Shown in Figure 2.9A are Henkel plots of three particle samples: PEI-coated ZFNCs (open circles), polyelectrolyte-coated ZFNCs (open triangles), and ZFNC@SiO_2

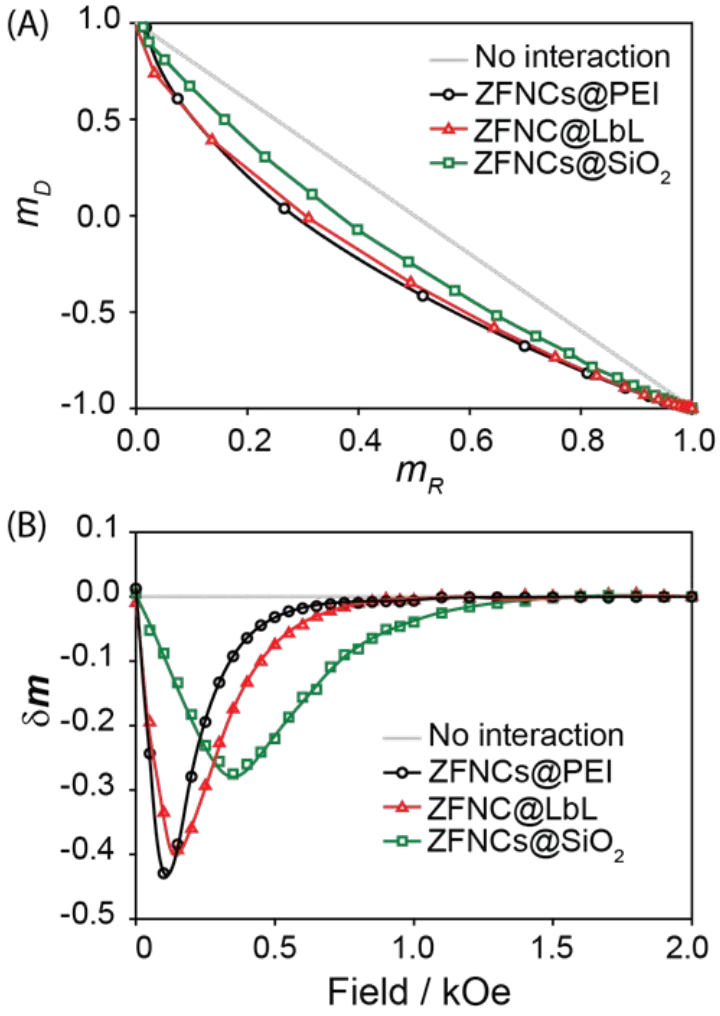

Figure 2.9 (A) Henkel and (B) δm plots produced from IRM and DCD measurements. The δm minima occur at 100, 150, and 350 Oe for the PEI-, LbL-, and silica-coated ZFNCs respectively

(open squares). All three MNPs demonstrate negative curvature from the Wohlfarth line (gray line in Figure 2.9A), with the magnitude of curvature decreasing from ZFNC@PEI to ZFNC@LbL to ZFNC@SiO_2. The negative deviation from the Wohlfarth line originates from magnetic dipole-dipole interactions.[58] As the interaction increases, the magnitude of deviation increases. Thus, the magnetic dipole-dipole interaction of the PEI-coated particles is reduced by LbL-polyelectrolyte coating and the interaction is further lessened by silica encapsulation.

A modified form of the Henkel representation, the δm plot, provides particle interaction information as a function of $\boldsymbol{H}$. Shown in Figure 2.9B are δm plots of the three ZFNC systems. A non-interacting assembly of single-domain ferromagnetic particles with uniaxial anisotropy has a $\delta m = 0$ at all $\boldsymbol{H}$. However, all three ZFNC systems demonstrate negative deviations from $\delta m = 0$. A field-shift of the minimum of the δm plot to larger values as a function of coating step is also observed. That is, δm for the PEI-coated ZFNCs reaches a more negative value than that of the other two samples and decays faster at lower fields. Since the interparticle distance between the PEI-coated ZFNCs is smaller than those of the multiple polyelectrolyte- and silica-coated ZFNCs, the strong dipole coupling interaction field of the PEI-coated ZFNCs aids the other ZFNCs in close proximity to reverse their magnetization at a lower applied field. Therefore, an ensemble of the PEI-coated ZFNCs demagnetizes faster than that of ZFNCs encapsulated by further coatings. This clearly indicates that the silica encapsulating layer separates ZFNCs and reduces their dipole-dipole interaction. Similar results for ferromagnetic FePt and silica-coated ferrimagnetic $CoFe_2O_4$ nanoparticle systems have been reported by others.[1, 18, 58, 59] The reduction of magnetic dipole coupling interactions by silica encapsulation is also consistent with the enhancement of the magnetic hardness (coercivity) of the ZFNCs@SiO_2.[60]

2.4 Conclusion

The drive to create silica-encapsulated MNPs stems not only from the fact that the shell acts to reduce magnetic-induced aggregation, but also that silica provides a surface amenable to *in vivo* use and is conducive to functionalization with molecular recognition moieties (*e.g.*, antibodies, peptides). However, the realization of silica-encapsulated, high

MNPs is challenging due to the strong interparticle attractive forces that exist during the coating procedure.

We have developed a method to deposit a uniform silica coating around high moment ($\boldsymbol{m}$~4×10^{-13} emu/particle at $\boldsymbol{H}$ = 150 Oe) ferrimagnetic zinc ferrite nanocubes (~130 nm). By depositing multiple polyelectrolyte layers around ZFNCs using an LbL process, a MNP suspension can be stabilized allowing the preparation of uniformly-coated individual ZFNC@SiO_2 particles. The polyelectrolyte multilayers increase the particle-particle closest approach distance and provide an increased surface charge, which in turn helps minimize dipole-induced aggregation. Our results indicate that successful creation of discrete core-shell nanocubes is realized only after depositing multiple polyelectrolyte layers. Without the intermediary polyelectrolyte layers, magnetic dipole-dipole interactions lead to the formation of linearly chained ferrimagnetic nanoparticles embedded in a silica matrix.

We foresee this encapsulation method being implemented to easily and routinely prepare discrete silica-coated ferrimagnetic nanoparticles for use in many biomedical applications.

2.5 Reference

(1) Dai, Q.; Lam, M.; Swanson, S.; Yu, R.-H. R.; Milliron, D. J.; Topuria, T.; Jubert, P.-O.; Nelson, A., *Langmuir* **2010,** *26,* 17546-51.

(2) He, J.; Huang, M.; Wang, D.; Zhang, Z.; Li, G., *J. Pharm. Biomed. Anal.* **2014**.

(3) Zhang, M.; Xie, X.; Wang, S. X.; Criddle, C. S. Magnetically Separable Synthetic Nanoparticles for Water Treatment. USPTO 14/032,033, **2013**.

(4) Yoon, T.-J.; Lee, W.; Oh, Y.-S.; Lee, J.-K., *New J. Chem.* **2003,** *27,* 227-229.

(5) Xu, C.; Sun, S., *Adv. Drug Delivery Rev.* **2013,** *65*, 732-743.

(6) Genc, S.; Derin, B., *Curr. Opin. Chem. Eng.* **2014,** *3*, 118-124.

(7) Balasubramaniam, S.; Kayandan, S.; Lin, Y.-N.; Kelly, D. F.; House, M. J.; Woodward, R. C.; St. Pierre, T. G.; Riffle, J. S.; Davis, R. M., *Langmuir* **2014,** *30*, 1580-1587.

(8) Millen, R. L.; Kawaguchi, T.; Granger, M. C.; Porter, M. D.; Tondra, M., *Anal. Chem.* **2005,** *77*, 6581-6587.

(9) Herrmann, I. K.; Schlegel, A.; Graf, R.; Schumacher, C. M.; Senn, N.; Hasler, M.; Gschwind, S.; Hirt, A.-M.; Günther, D.; Clavien, P.-A., *Nanoscale* **2013,** *5*, 8718-8723.

(10) Kolhatkar, A. G.; Nekrashevich, I.; Litvinov, D.; Willson, R. C.; Lee, T. R., *Chem. Mater.* **2013,** *25*, 1092-1097.

(11) Hu, W.; Wilson, R. J.; Koh, A.; Fu, A.; Faranesh, A. Z.; Earhart, C. M.; Osterfeld, S. J.; Han, S.-J.; Xu, L.; Guccione, S.; Sinclair, R.; Wang, S. X., *Adv. Mater.* **2008,** *20*, 1479-1483.

(12) Faraudo, J.; Andreu, J. S.; Camacho, J., *Soft Matter* **2013,** *9*, 6654-6664.

(13) Colombo, M.; Carregal-Romero, S.; Casula, M. F.; Gutiérrez, L.; Morales, M. P.; Böhm, I. B.; Heverhagen, J. T.; Prosperi, D.; Parak, W. J., *Chem. Soc. Rev.* **2012,** *41*, 4306-4334.

(14) Lattuada, M.; Hatton, T. A., *Langmuir* **2007,** *23*, 2158-68.

(15) Lu, A.-H.; Salabas, E. L.; Schüth, F., *Angew. Chem. Int. Ed.* **2007,** *46*, 1222-44.

(16) Cheon, J.; Jun, Y.-w.; Choi, J.-s. Water-Soluble Nanoparticles Stabilized with Multi-Functional Group Ligands and Method of Preparation Thereof. USPTO CA2576975 A1, **2013**.

(17) Zeltner, M.; Grass, R. N.; Schaetz, A.; Bubenhofer, S. B.; Luechinger, N. A.; Stark, W. J., *J. Mater. Chem.* **2012,** *22*, 12064-12071.

(18) Dai, Q.; Berman, D.; Virwani, K.; Frommer, J.; Jubert, P.-O.; Lam, M.; Topuria, T.; Imaino, W.; Nelson, A., *Nano Lett.* **2010,** *10*, 3216-3221.

(19) Marcelo, G.; Munoz-Bonilla, A.; Rodriguez-Hernandez, J.; Fernandez-Garcia, M., *Polym. Chem.* **2013,** *4*, 558-567.

(20) Parks, G., *Chem. Rev.* **1965,** *65*, 177-198.

(21) Thirumal, E.; Prabhu, D.; Chattopadhyay, K.; Ravichandran, V., *Phys. Status Solidi A* **2010,** *207*, 2505-2510.

(22) Falqui, A.; Corrias, A.; Gass, M.; Mountjoy, G., *Microsc. Microanal.* **2009,** *15*, 114-124.

(23) Carta, D.; Bullita, S.; Casula, M. F.; Casu, A.; Falqui, A.; Corrias, A., *ChemPlusChem* **2013,** *78*, 364-374.

(24) Marcelo, G.; Pérez, E.; Corrales, T.; Peinado, C., *J. Phys. Chem. C* **2011,** *115*, 25247-25256.

(25) Noh, S.-H.; Na, W.; Jang, J.-T.; Lee, J.-H.; Lee, E. J.; Moon, S. H.; Lim, Y.; Shin, J.-S.; Cheon, J., *Nano Lett.* **2012,** *12*, 3716-21.

(26) Stöber, W.; Fink, A.; Bohn, E., *J. Colloid Interface Sci.* **1968,** *26*, 62-69.

(27) Downs, R. T., The Rruff Project: An Integrated Study of the Chemistry, Crystallography, Raman and Infrared Spectroscopy of Minerals. In *Program and Abstracts of the 19th General Meeting of the International Mineralogical Association*, Kobe, Japan, **2006**.

(28) Swanson, H. E.; McMurdie, H. F.; Morris, M. C.; Evans, E. H.; Paretzkin, B., *Standard X-Ray Diffraction Powder Patterns, Nbs Monograph 25, Sections 5 and 9*. Institute for Materials Research, National Bureau of Standards: 1971.

(29) Swanson, H. E.; McMurdie, H. F.; Morris, M. C.; Evans, E. H., *Standard X-Ray Diffraction Powder Patterns, Nbs Monograph 25, Section 5*. Institute for Materials Research, National Bureau of Standards: 1967.

(30) Mourdikoudis, S.; Liz-Marzán, L., *Chem. Mater.* **2013,** *25*, 1465-1476.

(31) Fratila, R. M.; Mitchell, S. G.; Del Pino, P.; Grazu, V.; de la Fuente, J. M., *Langmuir* **2014**.

(32) Nann, T., *Chem. Commun.* **2005**, 1735-1736.

(33) Goon, I. Y.; Lai, L. M. H.; Lim, M.; Munroe, P.; Gooding, J. J.; Amal, R., *Chem. Mater.* **2009,** *21*, 673-681.

(34) Mørup, S.; Hansen, M. F.; Frandsen, C., *Beilstein J. Nanotech.* **2010,** *1*, 182-90.

(35) Martinez-Boubeta, C.; Simeonidis, K.; Makridis, A.; Angelakeris, M.; Iglesias, O.; Guardia, P.; Cabot, A.; Yedra, L.; Estradé, S.; Peiró, F., *Sci. Rep.* **2013,** *3*.

(36) Butter, K.; Bomans, P.; Frederik, P.; Vroege, G.; Philipse, A., *Nature Materials*

2003, *2*, 88-91.

(37) Szyndler, M. W.; Corn, R. M., *The Journal of Physical Chemistry Letters* **2012,** *3*, 2320-2325.

(38) Zhang, F.; Wang, C.-C., *J. Phys. Chem. C* **2008,** *112*, 15151-15156.

(39) Krogman, K.; Cohen, R.; Hammond, P.; Rubner, M.; Wang, B., *Bioinspir. Biomim.* **2013,** *8*, 045005.

(40) Caruso, F.; Spasova, M.; Susha, A.; Giersig, M.; Caruso, R. A., *Chem. Mater.* **2001,** *13*, 109-116.

(41) Caruso, F.; Lichtenfeld, H.; Giersig, M.; Möhwald, H., *J. Am. Chem. Soc.* **1998,** *120*, 8523-8524.

(42) Caruso, F.; Caruso, R. A.; Möhwald, H., *Science* **1998,** *282*, 1111-1114.

(43) Cornell, R.; Schwertmann, U., *The Iron Oxides: Structure, Properties, Reactions, Occurrences and Uses*. 2nd ed.; WILEY-VCH Verlag GmbH & Co. KGaA: Weinheim, 2003.

(44) Zhou, Y.; Tang, Z.; Shi, C.; Shi, S.; Qian, Z.; Zhou, S., *J. Mater. Sci. - Mater. Med.* **2012,** *23*, 2697-2708.

(45) Yu, J.; Yi, B.; Xing, D.; Liu, F.; Shao, Z.; Fu, Y.; Zhang, H., *Phys Chem Chem Phys* **2003,** *5*, 611-615.

(46) Beyer, S.; Bai, J.; Blocki, A. M.; Kantak, C.; Xue, Q.; Raghunath, M.; Trau, D., *Soft Matter* **2012,** *8*, 2760-2768.

(47) Martinez, J.; Ruiz, F.; Vorobiev, Y. V.; Pérez-Robles, F.; González-Hernández, J., *J. Chem. Phys.* **1998,** *109*, 7511-7514.

(48) McDonald, R. S., *J. Phys. Chem.* **1958,** *62*, 1168-1178.

(49) Malvern Instruments. Dynamic Light Scattering: An Introduction in 30 Minutes **2015**. http://www.malvern.com/en/support/resource-center/technical-notes/TN101104DynamicLightScatteringIntroduction.aspx.

(50) Lim, E.-K.; Kim, T.; Paik, S.; Haam, S.; Huh, Y.-M.; Lee, K., *Chem. Rev.* **2014**.

(51) Vereda, F.; de Vicente, J.; Morales, M. d. P.; Rull, F.; Hidalgo-Álvarez, R., *J. Phys. Chem. C* **2008,** *112*, 5843-5849.

(52) Jang, J.-t.; Nah, H.; Lee, J.-H.; Moon, S. H.; Kim, M. G.; Cheon, J., *Angew. Chem.*

Int. Ed. **2009,** *48*, 1234-8.

(53) Yang, Y.; Liu, X.; Yang, Y.; Xiao, W.; Li, Z.; Xue, D.; Li, F.; Ding, J., *J. Mater. Chem. C* **2013,** *1*, 2875.

(54) Wang, W.; Wang, Y.; Tu, L.; Feng, Y.; Klein, T.; Wang, J.-P., *Sci. Rep.* **2014,** *4*, 1-5.

(55) Lee, D. C.; Mikulec, F. V.; Pelaez, J. M.; Koo, B.; Korgel, B. A., *J. Phys. Chem. C* **2006,** *110*, 11160-11166.

(56) Morales, M.; Munoz-Aguado, M.; Garcıa-Palacios, J.; Lazaro, F.; Serna, C., *J. Magn. Magn. Mater.* **1998,** *183*, 232-240.

(57) Che, X.-d.; Neal Bertram, H., *J. Magn. Magn. Mater.* **1992,** *116*, 121-127.

(58) Laureti, S.; Varvaro, G.; Testa, A.; Fiorani, D.; Agostinelli, E.; Piccaluga, G.; Musinu, A.; Ardu, A.; Peddis, D., *Nanotechnology* **2010,** *21*, 315701.

(59) Zeng, H.; Li, J.; Wang, Z. L.; Liu, J. P.; Sun, S., **2002**.

(60) Blanco-Mantecon, M.; O'Grady, K., *J. Magn. Magn. Mater.* **2006,** *296*, 124-133.

CHAPTER 3

INFLUENCE OF NANOPARTICLE ARRANGEMENT ON MAGNETIC PROPERTIES: MAGNETIC INTERACTIONS AND ENERGY BARRIER ENHANCEMENT

3.1 Introduction

Recent progress in nanoparticle synthesis and the ensuing control of size and morphology have triggered strong interest in the properties of magnetic nanoparticles. In bulk materials, magnetic properties are controlled by composition, crystallographic structure, magnetic anisotropic energy, and structural defects.[1] Interestingly, when the size of these materials approaches the nanometer length scale, their magnetic properties can differ markedly from those of their larger (bulk) analogs due to the importance of size and shape at such small size scales. For example, bulk ferro-/ferrimagnetic materials can spontaneously magnetize, whereas a single-domain ferro-/ferrimagnetic nanoparticle can have a zero remanent magnetization ($\boldsymbol{M_r}$) and coercivity ($\boldsymbol{H_c}$) (*i.e.*, superparamagnetism) of zero after the removal of an external magnetic field ($\boldsymbol{H}$). Due to the large surface-to-volume ratio of nanoscale objects, shape associated with surface atoms can affect magnetic properties.[2-4] Noh et al. showed that spherical and cubic magnetic nanoparticles (MNPs)

with the same volume and composition have different saturation magnetization ($\boldsymbol{M_s}$) values, which resulted from the fact that the spherical MNPs have a higher percentage of disordered magnetic spins at the surface than the cubic MNPs.[3]

Beyond the nanoscale effect of size and shape, magnetic interactions can also affect their magnetic properties of MNPs. Magnetic interactions can include exchange coupling (*i.e.*, intraparticle interaction) and magnetic dipolar interaction (*i.e.*, interparticle interaction). Magnetic exchange coupling refers to interactions of magnetic spins between two adjacent magnetic layers.[5] Indeed, changes in magnetic properties due to the exchange coupling are often observed in core-shell (core@shell) nanoparticles. Magnetic exchange coupling between ferromagnetic and antiferromagnetic layers in core@shell nanoparticles can provide an extra source of anisotropy.[6-8] In another example, when partially oxidized cobalt nanoparticles (*i.e.*, Co@CoO) are cooled in the presence of a magnetic field, the hysteresis of the particles is no longer symmetrical about the origin, but is horizontally shifted along the applied field axis.[7] This unusual property of field-cooled Co@CoO particles arises from exchange coupling at the interface of ferromagnetic Co and antiferromagnetic CoO (a.k.a., exchange bias).

Controlling magnetic properties through interparticle dipolar interactions is of great interest in magnetic materials, including superlattices, nanoparticle assemblies, and nanocomposites.[9-14] In these materials, the surface coating on the magnetic material plays a significant role in manipulating the nature and strength of interparticle interactions. To control interparticle interactions, MNPs are often dispersed in a solid matrix, such as silica or epoxy, with different concentrations. These coatings (*e.g.*, organic molecules or inorganic protective layers) not only prevent the particles from aggregating, which reduces

exchange coupling interactions between surface atoms, but also increase the distance between particles, the changes of which manipulate the dipole-dipole interactions. The recent work by Dai et al. is an example of how particle-particle proximity can affect magnetization. Their work compared the magnetization of cobalt ferrite nanoparticles with those of the same particles after encapsulation with a silica coating. The data showed that the closer proximity between the uncoated particles and the resulting increase in dipole-dipole interactions caused a decrease in $\boldsymbol{H_c}$ due to assisted magnetization reversal.[15] A similar effect was observed for ferromagnetic FePt nanoparticles and silica-coated zinc ferrite nanocubes.[16-17] Cobalt nanoparticles incorporated into mesoporous silica aligned in a chain and produced a higher $\boldsymbol{H_c}$ than either noninteracting or randomly aggregated particles.[18] $\boldsymbol{H_c}$ of spherical γ-Fe_2O_3 particles decreased when dispersed in a silica matrix at low volume fraction, which corresponds to the predicted reduction in interparticle interaction.[19] As described above, the magnetic properties of MNPs are not only determined by physical properties (*i.e.*, size and shape), but also controlled by magnetic interactions (*i.e.*, exchange coupling and dipolar interactions). Therefore, understanding the influence of magnetic interactions on the magnetic properties of nanomaterials is fundamentally important, which eventually enables fine tuning of magnetic properties of the materials for a specific application.

Development of MNP assemblies using bottom-up approaches is an emerging field of research because it is a facile way to develop a new material whose properties can be designed by changing the arrangement of individual MNPs (*i.e.*, changing magnetic interactions).[1, 12, 20-21] The magnetic properties of MNP assembly are not only determined by size distribution and shape of individual MNPs, but also modified by the arrangement

of those particles. Peddis et al. reported that the formation of iso-oriented, spherical assemblies of cobalt ferrite nanoparticles induces an increase in $\boldsymbol{H_c}$ and $\boldsymbol{M_r}$, compared to the random aggregates of the nanoparticles.[22] Also, due to the collective magnetic behavior of MNP clusters/assemblies, they are more responsive to an external $\boldsymbol{H}$ than individually dispersed MNPs, which can potentially serve as contrast agents in *in-vivo* imaging and carriers for drug-delivery.[23-24]

The focus of this chapter is the investigation of the effect of arrangement of MNPs on their magnetic properties by comparing zinc ferrite nanoparticles (ZFNPs) and colloidally assembled magnetic beads (ZFMBs). To this end, ZFNPs (~11 nm) were synthesized using thermal decomposition. The ZFMBs (~170 nm) were created by assembling ZFNPs into a larger bead using an emulsion-based bottom-up assembly. First, the physical properties of ZFNPs and ZFMBs were carefully characterized for size, shape, and crystallinity using electron micrograph and X-ray diffractometry. Possible crystal structure deformation or oxidation of ZFNPs, which may occur in the assembling procedure, was investigated using Raman spectroscopy and high-resolution electron microscopy, because those transformations affect magnetic properties. Then, these particles were dispersed in epoxy matrices in order to spatially separate individual particles. The magnetic properties of ZFNPs and ZFMBs were investigated using various magnetic measurement techniques, including hysteresis curve, zero-field/field cooled magnetization, and remanence measurements. This chapter aims to understand the influence of the different arrangements of nanoparticles on magnetic properties, which can open interesting perspectives in controlling magnetic behavior via magnetic interactions, as well as in optimizing magnetic properties for a specific application via controlling nanoparticle

arrangement.

3.2 Experimental Section

3.2.1 Materials

Iron acetylacetonate ($Fe(acac)_3$), zinc acetylacetonate ($Zn(acac)_2$), oleylamine, ethylene glycol, benzyl ether, and chloroform were purchased from Acros organics (USA). Oleic acid was acquired from Alfa Aesar (USA). Poly(vinylpyrrolidone) (PVP, MW ~50 kDa) and dodecyltrimethylammonium bromide (DTAB) were obtained from Sigma Aldrich (USA). Ethanol (200 proof) was purchased from DeconLab (USA).

3.2.2 Synthesis of Zinc Ferrite Nanoparticles

Zinc ferrite nanoparticles (ZFNPs) were synthesized by thermal decomposition. Briefly, 1.3 mmol $Fe(acac)_3$, 0.3 mmol $Zn(acac)_2$, 2.1 mL of neat oleic acid, and 2.1 mL of oleylamine were added to 20 mL of benzyl ether and refluxed at 290 ˚C for 1 h in a nitrogen atmosphere. The as-synthesized particles were precipitated by the addition of ethanol, and then thoroughly rinsed with the mixture of hexane and acetone (1:3 v/v) by centrifugation (5500*g* for 30 min). The rinsing procedure was repeated twice. The particles were dried under vacuum and resuspended in chloroform at ~20 mg/mL.

3.2.3 Synthesis of Colloidal Assemblies of ZFNPs

The colloidal assemblies of ZFNPs (ZFMBs) were prepared using a microemulsion/evaporation technique. First, 1.0 mL DTAB solution (20 mg/mL) was added to 1.0 mL of the ZFNPs (~20 mg/mL in chloroform) in a 5 mL centrifuge tube and

vortexed for 5 min. Then, the emulsion was transferred to a round bottom flask and the chloroform was selectively removed by placing the flask in a water bath (40 °C) and purging with nitrogen. The resulting aqueous solution was injected into a flask containing 5 mL of PVP in ethylene glycol (110 mg/mL) under vigorous stirring. After stirring for 10 min at room temperature, the mixture was heated to 80 °C, refluxed for 6 h under an inert atmosphere, and was cooled to room temperature. Subsequently, the colloidal assemblies of ZFNPs were separated by centrifugation (5500g, 10 min) and the black precipitate was resuspended in 15 mL of ethanol. This centrifugation was repeated twice. Finally, the particles were resuspended in 10 mL of ethanol.

3.2.4 Characterization

3.2.4.1 Scanning (SEM) and transmission electron microscopy (TEM). SEM images were acquired using a Hitachi S-4800 (Japan), which was equipped with an energy dispersive X-ray spectroscopy module (EDS, INCA Inc.). Particle samples were drop casted onto a 1×1 cm silicon chip for SEM imaging and EDS analysis. TEM images were obtained using a JEM-2800 electron microscope (JEOL) operating at 200 kV. A drop of particle suspension was deposited on a lacey-carbon copper TEM grid and allowed to evaporate. All images were captured using a Gatan ORIUS CCD camera.

3.2.4.2 X-ray diffraction (XRD). Powder X-ray diffraction (Panalytical X'Pert X-ray diffractometer, Philips) was used for the determination of crystallinity and phases of the ZFNPs. Diffractogram was collected with Cu Kα radiation ($\lambda = 0.154$ nm) at 40 mA and 45 kV. These data were compared to the RRUFF database (https://rruff.info/) for identification.[25]

3.2.4.3 Inductively coupled plasma mass spectroscopy (ICP-MS). The molar ratio of Zn to Fe in the as-synthesized ZFNPs was determined by inductively coupled plasma mass spectrometer (Agilent 7500ce). The ZFNPs were dissolved in 3 mL HCl and 1 mL HNO_3 and diluted with 5% HNO_3. A calibration solution containing 200 ppm Fe and 10.0 ppm Zn was prepared using single element standard solutions (Inorganic Ventures). The sample and calibration solution were run together using a double-pass spray chamber, quartz injector, and platinum cones. The collision cell was flushed with He gas at a rate of 8 mL/min in order to minimize $^{40}Ar^{16}O$ interference at mass 56.

3.2.4.4 Raman spectroscopy. Raman spectra were collected using a DXR Raman microscope (Thermo Scientific). Particle samples were prepared by evaporating a droplet of the particle suspension onto a 1×1 cm gold chip. Spectra were collected using a laser with a wavelength of 633 nm, power of 7 mW (at sample), a 10 s exposure time, and a resolution of 1 cm^{-1}. Raman spectrum for Fe_3O_4 was obtained for comparison purposes from the RRUFF database (RRUFF ID# R080025).[25]

3.2.5 Magnetic Measurements

The magnetic characterization of samples was performed using a vibrating sample magnetometer (VSM, Microsense EZ7). Samples were prepared by immobilizing particles in a polymer matrix (*i.e.*, epoxy) to reduce the potential effects of dipolar interactions. All particle samples were dispersed in UV-curable epoxy matrices (less than 0.1 wt%), injected into a capsule, and allowed to cure completely under UV light for ~12 h.

3.2.5.1 Hysteresis curve measurement. Hysteresis curves were measured using a VSM at several temperatures (100, 150, 200, 250, and 298 K) with a field range of −15 kOe to +15 kOe. The magnetization curve from a blank sample (*i.e.*, epoxy matrix and capsule) was subtracted from the magnetization curve from the particle sample in order to obtain correct magnetic parameters.

3.2.5.2 ZFC/FC measurement. For the measurement of zero-field cooled/field cooled (ZFC/FC) magnetization curves, an applied field of 100 Oe was used. For the measurement of ZFC curves, the sample was first cooled to 80 K in the absence of an external $\boldsymbol{H}$, and the net magnetization was then measured with a temperature sweep rate of 3 K/min. Measurements of FC curves were carried out after the ZFC measurements. FC magnetizations were recorded while the sample was cooled from 300 to 80 K at 100 Oe.

3.2.5.3 Isothermal remanence magnetization (IRM)/Direct current demagnetization (DCD). Interparticle interactions were investigated by IRM and DCD. For IRM analysis, the samples were first brought to a demagnetized state by applying alternating magnetic fields with an AC demagnetization factor of 0.9. The next step applied a magnetic field of a given value and $\boldsymbol{M_r}$ was measured at $\boldsymbol{H}$ = 0. This cycle was repeated with increasing $\boldsymbol{H}$ (0 to +1,000 Oe). DCD measurements were performed in a similar fashion. For DCD analysis, the sample was first exposed to an $\boldsymbol{H}$ of –1,000 Oe and the $\boldsymbol{M_r}$ was recorded by increasing $\boldsymbol{H}$ in the opposite direction to +1,000 Oe. The data from IRM and DCD were used to create delta-$\boldsymbol{m}$ ($\delta\boldsymbol{m}$) plots and irreversible susceptibility ($\boldsymbol{\chi}_{irr}$), which is the first derivative of DCD measurement (*i.e.*, $\mathrm{d}M_{DCD}/dH$).

For non-interacting single-domain ferromagnetic particles with uniaxial anisotropy, the measured remanences from IRM ($M_{IRM}(H)$) and DCD ($M_{DCD}(H)$) are related to each

other by the Wohlfarth relation:[26]

$$m_d(H) = (1 - 2m_r(H)) \quad (3.1)$$

where m_d is the normalized remanent magnetization from the DCD measurement [$M_{DCD}(H)/M_{DCD}(H_{sat})$] and m_r is the normalized remanent magnetization from the IRM measurement [$M_{IRM}(H)/M_{IRM}(H_{sat})$]. The $\delta \boldsymbol{m}$ curve is defined as the difference between two normalized remanent magnetizations.[27]

$$\delta \boldsymbol{m} = m_d(H) - (1 - 2m_r(H)) \quad (3.2)$$

3.2.6 Particle Size Measurement

ImageJ, a public image processing program (National Institute of Health),[28] can be used to calculate area, pixel value statistics, distances, and angles of user-defined selections. For the calculation of an average diameter of ZFNPs, the boundaries of particles in a SEM image were defined using a default threshold. Then, the surface surface area (***S***) of each boundary was calculated. Assuming that particles are spherical, the ***S*** is converted into a diameter (***D***) using the equation for surface area of a circle ($\boldsymbol{D} = \sqrt{4\boldsymbol{S}/\pi}$). For the calculation of an average diameter of ZFMBs, the diameters of individual ZFMBs were measured by drawing a linear line in the center of the ZFMB.

3.3 Results and Discussion

The results from a series of morphological, structural, and compositional analyses of the two sets of particles are presented in Figure 3.1-3.4. Figure 3.1A shows an SEM micrograph for the ZFNPs. The image reveals that the ZFNPs have a faceted shape, with a size ranging from 6 to 17 nm. The average diameter from the measurement of a larger number of particles (n=550) was 11 ± 2 nm. A histogram of these data is given in Appendix B.

The TEM image and its accompanying lattice fringe pattern of ZFNP are shown in Figure 3.1B. The lattice fringe pattern confirms the crystalline nature of the ZFNPs. Moreover, the lattice spacing of 1.72 Å matches that for the (422) crystalline plane of magnetite (Fe_3O_4).[29] This result is supported by the XRD pattern for the ZFNPs in Figure 3.2A. The Bragg reflections for the ZFNPs (blue) are in close correspondence to those for the reflection data for Fe_3O_4 (red) with an inverse spinel structure.[30]

The Raman spectra in Figure 3.3 provide further evidence that the ZFNPs have the same crystal structure as Fe_3O_4. At ambient conditions, the Raman spectrum (unpolarized)

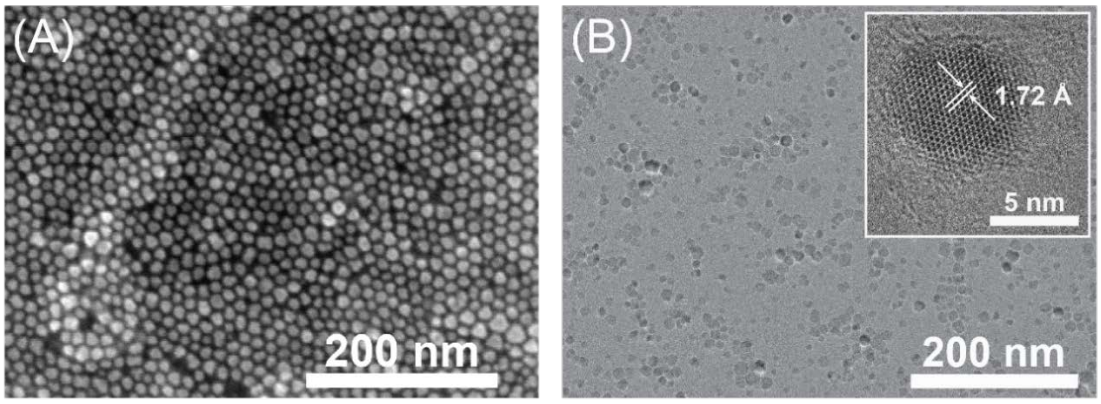

Figure 3.1 Synthesis and characterization of ZFNPs. (A) SEM and (B) TEM images of the as-synthesized ZFNPs. The inset in (B) is a high-resolution TEM image of a single ZFNP with a lattice fringe pattern.

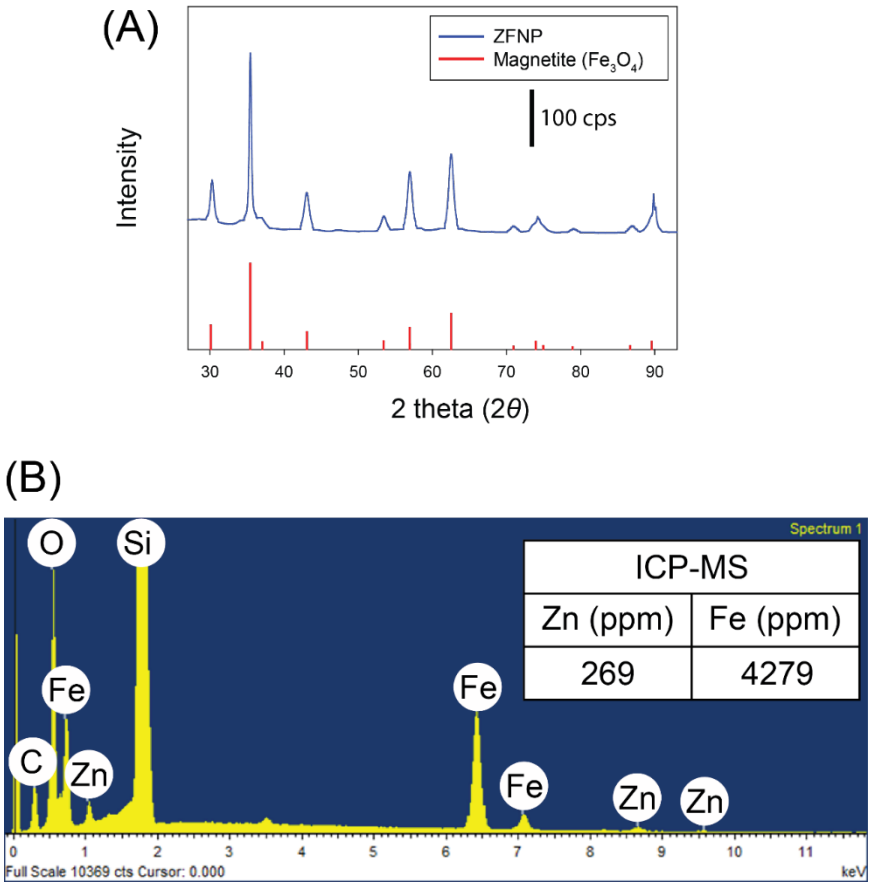

Figure 3.2 Elemental analysis of ZFNPs. (A) XRD pattern and (B) EDS spectrum of ZFNPs. The XRD pattern of ZFNPs matches to that of Fe_3O_4 obtained from the RRUFF database (ID# R080025). Note that a silicon peak at 1.74 keV arises from the substrate used for imaging. The determination of Zn and Fe content shown in the inset of (B) was obtained by ICP-MS.

of Fe_3O_4 typically shows three predicted phonon bands at 306, 538 and 669 cm^{-1}.[31] As evident in Figure 3.3, the as-synthesized ZFNPs exhibit three of these phonon bands assigned to symmetric bending of O with respect to Fe (E_g) at 321 cm^{-1}, asymmetric stretching of Fe and O (T_{2g}) at 549 cm^{-1}, and symmetric stretching of O along Fe−O bonds (A_{1g}) at 672 cm^{-1}.[31]

The presence of Zn in the ZFNPs was confirmed by EDS and ICP-MS. Figure 3.2B shows the EDS elemental analysis of the ZFNPs, and includes Zn peaks at 1.01 and 8.63

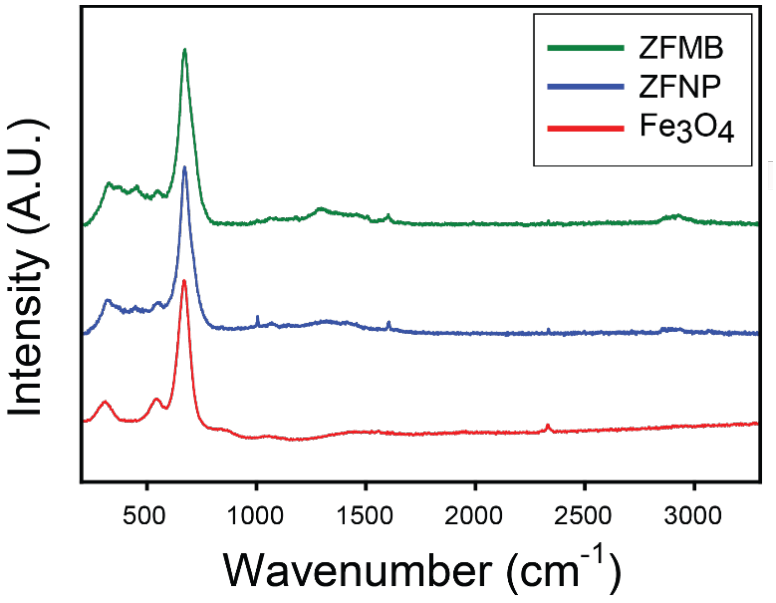

Figure 3.3 Raman spectra of the ZFNPs and ZFMBs. Note that Raman spectrum of Fe_3O_4 was obtained from the RRUFF database (magnetite, RRUFFID# R080025).

keV. These EDS data yield a mole ratio for Zn:Fe of 4.8 and 95.2. The Zn:Fe mole ratio was also measured by ICP-MS (see inset of Figure 3.2B) to be 5.1:94.9. The ZFNPs are therefore nonstoichiometric (*i.e.*, $Zn_xFe_{3-x}O_4$) with the composition of $Zn_{0.15}Fe_{2.85}O_4$. In the inverse spinel structure of Fe_3O_4, the oxygen atoms are arranged in a closely packed face-centered cubic structure. This results in two different sublattices for occupation of iron atoms (*i.e.*, Fe^{2+} and Fe^{3+}): (1) tetrahedral and (2) octahedral sites. In theory, the octahedral sites are shared by an equal number of Fe^{2+} and Fe^{3+} ions, while the tetrahedral sites are only occupied by Fe^{3+} ions.[30] Given the strong similarity of inverse spinel structure of our ZFNPs to that of Fe_3O_4, the zinc ions (Zn^{2+}) would therefore occupy the octahedral interstices.

Colloidal assemblies of ZFNPs (*i.e.*, ZFMB) were synthesized using the emulsion-based template method described earlier.[20-21] The SEM image in Figure 3.4A shows that

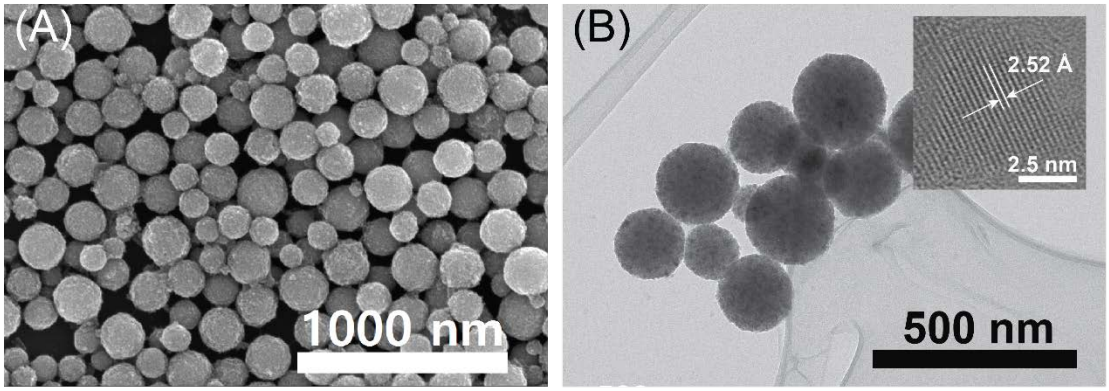

Figure 3.4 Synthesis and characterization of ZFMBs. (A) SEM image and (B) TEM image of the as-synthesized ZFMBs. The inset is a high-resolution TEM image of the ZFMBs, revealing a lattice spacing distance of ZFNPs in the ZFMB.

the as-synthesized ZFMBs have a spherical shape and an average diameter of 172 ± 42 nm (n=250). Moreover, Figure 3.4B reveals that a single ZFMB consists of a large number of ZFNPs assembled into a spherical bead, and a lattice *d*-spacing of 2.52 Å in the ZFMB sample corresponds to the (311) plane of the inverse spinel structure of Fe_3O_4.

Raman spectroscopy is an effective tool to distinguish different forms of iron oxides, such as magnetite (Fe_3O_4) and maghemite (γ-Fe_2O_3), and, therefore, was used to check for the possible oxidation of the surface atoms of ZFNPs and/or transformation of the crystallinity phase of ZFNPs due to the assembly process. As can be seen in Figure 3.3, the Raman spectrum of the ZFMBs is close to indistinguishable from that for the ZFNPs. That is, the same three phonon bands at 327, 549, and 672 cm^{-1} are evident in the spectrum of the ZFMBs and ZFNPs. In contrast, the Raman spectrum of γ-Fe_2O_3 (an oxidized form of Fe_3O_4) is characterized with three bands around 350, 500, and 700 cm^{-1}.[31-32] These signatures for γ-Fe_2O_3 are absent in the spectra of ZFNPs and ZFMBs in Figure 3.4. We therefore conclude that the assembly of ZFNPs into ZFMBs does not alter on the crystallinity and atomic structure of the ZFNPs.

To investigate the magnetic properties of ZFNPs and ZFMBs, a number of magnetic measurements were carried out via VSM. First, the hysteresis curves of ZFNPs and ZFMBs shown in Figure 3.5 were acquired at several temperatures (100, 150, 200, 250, and 298 K). These curves are used to compare the three key magnetic parameters ($\boldsymbol{M_s}$, $\boldsymbol{H_c}$, and $\boldsymbol{M_r}$) at different temperatures. At a sufficiently high temperature, the hysteresis curve of a magnetic material matches that of the Langevin function.[33] If the hysteresis curve follows the Langevin function, the magnetic material is paramagnetic (zero $\boldsymbol{H_c}$ and $\boldsymbol{M_r}$). When this functional dependence is observed in ferromagnetic or ferrimagnetic nanoparticles, it is called superparamagnetic. In Figure 3.5, both particle samples showed superparamagnetism with immeasurable values for $\boldsymbol{H_c}$ and $\boldsymbol{M_r}$ at room temperature. As temperature decreases, $\boldsymbol{M_s}$ for both ZFNPs and ZFMBs increase. This is due to a reduction in the extent of thermal agitation (k_BT) as temperature decreases. Thermal agitation randomly flips the magnetization of MNPs, preventing an alignment of magnetic moments. In other words, a decrease in temperature allows for a more extensive alignment of the

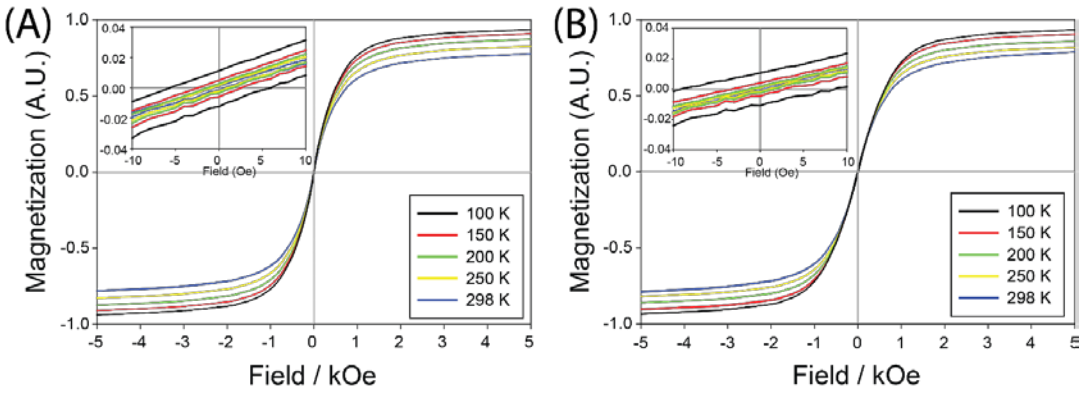

Figure 3.5 Temperature-dependent hysteresis curves of (A) ZFNPs and (B) ZFMBs. Note that $\boldsymbol{H_c}$ and $\boldsymbol{M_s}$ for both ZFNPs and ZFMBs increase with the decrease in temperature. Each magnetization curve was normalized using the highest $\boldsymbol{M_s}$ value for each particle, which was measured at 100 K.

magnetic moments of MNPs in the direction of $\boldsymbol{H}$, which leads to an increase in $\boldsymbol{M_s}$.

$\boldsymbol{H_c}$ is also affected by a change in temperature. As shown in Figure 3.6, $\boldsymbol{H_c}$ for both ZFNPs and ZFMBs decreases with an increase in temperature. [4, 34] This decrease in $\boldsymbol{H_c}$ is also due to the increase in thermal agitation (k_BT) that causes random changes in the orientation of magnetic moments in particles. The increase in k_BT with temperature results in an increase in the relaxation rate of magnetic moments and, consequently, an increase in the random orientation of the moments in a given measurement time interval. At low temperatures, however, the relaxation rate decreases and eventually becomes slower than the time of a measurement. This results in a magnetic hysteretic behavior (*i.e.*, the appearance of $\boldsymbol{H_c}$ and $\boldsymbol{M_r}$). Note that the relaxation process in our samples includes only the coherent rotation of magnetic moments (*i.e.*, Neel relaxation),[35] since the measured samples were fixed in epoxy matrices. It is interesting to see in Figure 3.6 that the $\boldsymbol{H_c}$ values of ZFMBs at T < 150 K are higher than those of the ZFNPs. We attribute this $\boldsymbol{H_c}$

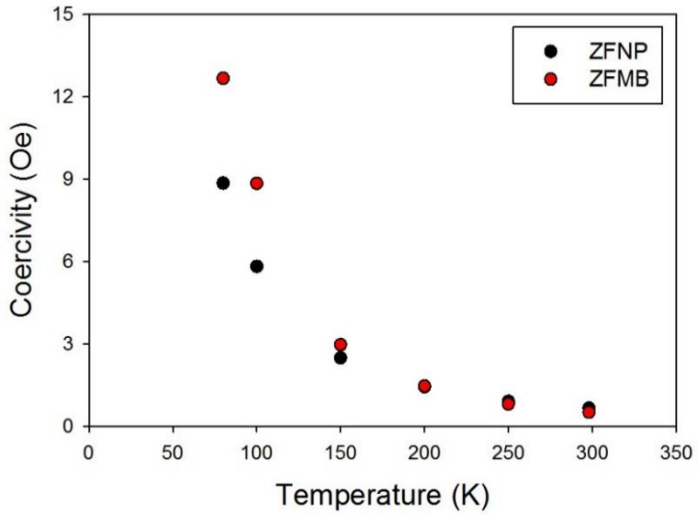

Figure 3.6 Temperature-dependent $\boldsymbol{H_c}$ of ZFNPs and ZFMBs, extracted from hysteresis curve measurements. Below 200 K, the difference in $\boldsymbol{H_c}$ between ZFNPs and ZFMBs increases with a decrease in temperature.

enhancement in the ZFMBs to strong magnetic dipolar interactions. The ZFNPs and ZFMBs are spatially distributed in epoxy matrices. However, a large number of ZFNPs in a single ZFMB is closely packed in a confined space, which leads to strong magnetic dipolar interactions between the ZFNPs in a ZFMB. It is known that magnetic dipolar interactions for nanoparticle assemblies are much greater than those of individual nanoparticles, and anisotropic magnetic dipolar interactions (*e.g.*, nanoparticles aligned in a chain or nanoparticles packed in cylindrical pores) result in a large enhancement in $\boldsymbol{H_c}$.[18, 36] In our case, since the oil phase (chloroform) was evaporated in a magnetically stirred water bath, it is possible that, during the evaporation step, the ZFNPs were weakly magnetized, which may have resulted in a preferential easy axis orientation and an increase in anisotropy.[37]

The blocking temperature (T_B) of ZFNPs and ZFMBs were obtained by ZFC/FC magnetization measurements. In the ZFC measurement, the particle samples are cooled in the absence of an external $\boldsymbol{H}$, which facilitates alignment of magnetic moments to their easy axis. This alignment is then fixed at a low temperature. As temperature is increased, the thermal energy releases the fixed (a.k.a., "blocked") magnetic moments from their initial alignments and, subsequently, allows those moments to align with the magnetic field. Therefore, the net magnetization at the beginning of the ZFC curve increases with temperature. Finally, the ZFC magnetization reaches a maximum and then undergoes a decrease with increase in temperature. This maximum temperature is defined as the "blocking" temperature, T_B .[38] As shown in Figure 3.7, the T_B of the ZFMBs (~215 K) is significantly higher than that of the ZFNPs (~106 K). This shift to a higher temperature implies that the anisotropy energy barrier for magnetization reversal in the ZFMBs is

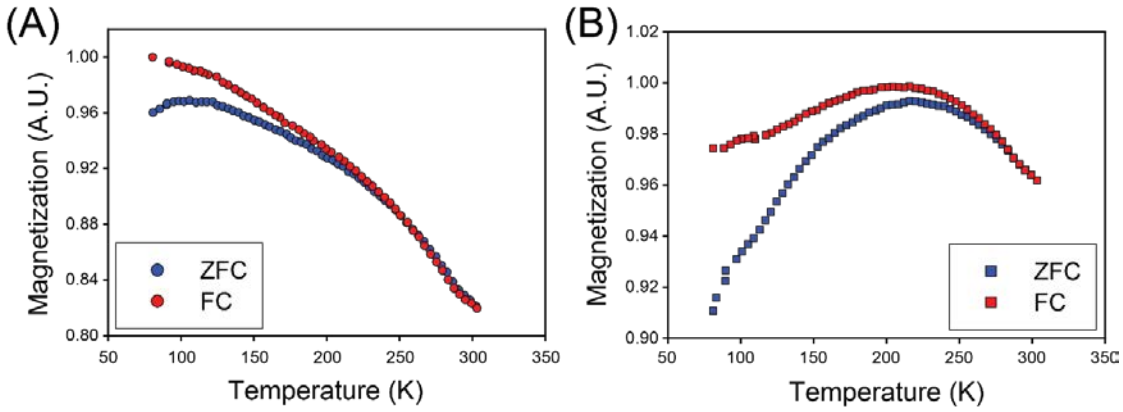

Figure 3.7 Zero-field cooled/field cooled (ZFC/FC) magnetization curves for (A) ZFNPs and (B) ZFMBs immobilized in epoxy matrices. ZFC/FC curves were measured between 80 and 300 K. The higher T_B of ~215 K and the magnetization reduction below the T_B in the FC curve for ZFMBs are indicative of strong interactions between the individual ZFNPs in the ZFMBs.

enhanced by the assembly formation when compared to the ZFNPs. Given that there are no phase or crystal structure changes evident in the seed ZFNPs upon colloidal assembly, the origin of the T_B shift is attributed to the strong dipole-dipole coupling taking place between neighboring ZFNPs when present in the ZFMBs. It is known that interparticle magnetic coupling can suppress the magnetic spin reversal due to thermal fluctuations and, therefore, increase the transition from ferromagnetism to superparamagnetism to a higher temperature.[13, 22, 39-40] Increases in T_B after the cluster/assembly formation have also been found in other systems.[13, 22-23, 41]

The FC magnetization curves of ZFNPs and ZFMBs in Figure 3.7 (red) also convey information on the magnetic coupling between nanoparticles. As temperature decreases from 300 K in the presence of $\boldsymbol{H}$, the net magnetization for both ZFNPs and ZFMBs increases. This behavior is due to a reduction in the thermal fluctuation of the magnetic moments as temperature decreases, leading to an increase in magnetization. However, there is one noticeable difference in the FC curves below 200 K. The FC magnetization of the

ZFMBs shows a maximum at ~200 K, while that of the ZFNPs continues to increase as temperature decreases. FC magnetization curves often have a plateau or a decrease below T_B when strong dipolar interactions between MNPs stabilize magnetic spins in their initial configuration and blocks the spins from aligning with the field.[14, 41-42] Therefore, the decrease in magnetization of the ZFMBs below ~200 K further indicates that there is a much stronger dipolar coupling between individual particles in the ZFMBs than with the ZFNPs.

The magnetic interactions (*i.e.*, types and strength of interaction) can be further examined using $\delta \boldsymbol{m}$ and irreversible susceptibility (χ_{irr}) plots based on IRM and DCD measurements. First, magnetic interactions were examined by $\delta \boldsymbol{m}$ plots (Figure 3.8A). A negative deviation from the non-interacting condition (gray linear line in Figure 3.8A) can be attributed to the dominance of magnetic dipolar interactions between particles, while a positive deviation arises from the exchange interactions between atoms at the surface of particles.[27] Thus, the negative deviation in $\delta \boldsymbol{m}$ plots in Figure 3.8A shows that magnetic dipolar interactions are dominant in both ZFNPs and ZFMBs. However, the minimum in

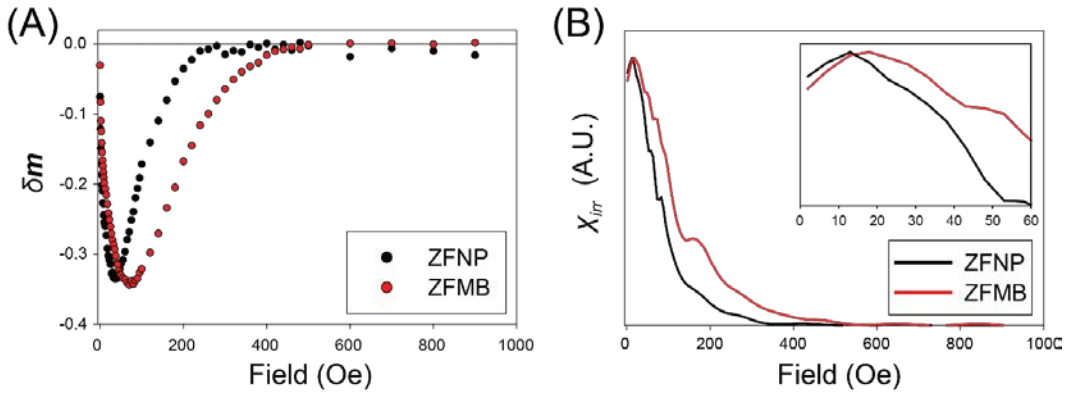

Figure 3.8 Investigation of magnetic interactions. (A) $\delta \boldsymbol{m}$ plot and (B) irreversible susceptibility (χ_{irr}) curves of ZFNPs and ZFMBs. The $\delta \boldsymbol{m}$ plot and χ_{irr} were derived from IRM/DCD measurements at 80 K.

the value of $\delta \boldsymbol{m}$ value shifts from 35 Oe for the ZFNPs to 70 Oe for the ZFMBs. $\delta \boldsymbol{m}$ for the ZFMBs also reaches a more negative value and decays slower than ZFNPs. This implies that the higher anisotropic energy barrier of the ZFMBs, produced by the stronger dipole-dipole interactions in ZFMBs, suppresses fast demagnetization of the ZFMBs.

The field-dependent irreversible susceptibility (χ_{irr}) is related to the distribution of coercive fields (*i.e.*, energy barrier distribution) in particle samples.[8, 43] As shown in Figure 3.8B, the χ_{irr} curve for the ZFMBs is broader than that for the ZFNPs, with the maximum shifting to a higher field. This indicates that the reversal processes of the magnetic moments in ZFMBs is slower than that of ZFNPs, which reflects a higher and broader energy barrier distribution in ZFMBs. It is known that magnetic dipolar interactions in nanoparticle assemblies are much stronger than that of individual MNPs and the magnetic dipolar interactions in the densely packed MNPs result in a ferromagnetic effect and coercivity enhancement.[18, 22] Therefore, the formation of spherical assemblies induces an increase in the anisotropic energy barrier, leading to an increase in $\boldsymbol{H_c}$. This observation is also consistent with a higher $\boldsymbol{H_c}$ for ZFMBs than that for ZFNPs in Figure 3.6.

The present results in the previous magnetic measurements demonstrate that the magnetic dipolar interactions among ZFNPs in a single ZFMB is an extra source of anisotropy. This leads to enhancement in the thermal stability of magnetic moments of ZFNPs in the ZFMBs, which was observed in a larger increase of T_B and $\boldsymbol{H_c}$ in ZFMBs. Increasing thermal stability of magnetic moments of MNPs (*i.e.*, delaying the transition from ferromagnetism to superparamagnetism to a higher temperature) is an important research topic in magnetic recording area. Although the system discussed in this study does not show a huge improvement of thermal stability, the approach present here provides an

interesting aspect in terms of designing new magnetic materials via magnetic interactions.

3.4 Conclusion

Even though magnetic properties of nanomaterials are strongly dependent on their size and shape, magnetic interactions can also play a significant role in the magnetic properties of nanoparticles. The strength and nature of magnetic interactions depend on the arrangement of MNPs and their interparticle distance. In this chapter, we have investigated the influence of nanoparticle arrangement on magnetic properties by comparing two different particles. At room temperature, both ZFNPs and ZFMBs are superparamagnetic. $\boldsymbol{M_s}$ values for both ZFNPs and ZFMBs increase with a decrease in temperature. It is, however, interesting that the difference in $\boldsymbol{H_c}$ between ZFNPs and ZFMBs increases with a decrease in temperature. ZFC/FC magnetization curves indicated that T_B of the ZFMBs is shifted to a higher temperature compared to that of the ZFNPs, indicating that the anisotropic energy barrier in the ZFMBs is increased. The increased energy barrier observed in the ZFMBs corresponds to a higher $\boldsymbol{H_c}$ of the ZFMBs than that of ZFNPs. Given that deformation of crystallinity and structure of ZFNPs upon assembly into ZFMBs has not been detected, as evidenced by TEM and Raman measurements, we believe that the arrangement of ZFNPs into spherical assemblies induces stronger magnetic dipolar interactions between the particles, which is responsible for the increase in the anisotropic energy barrier as well as $\boldsymbol{H_c}$. This assertion is supported by IRM and DCD measurements, revealing that stronger magnetic dipolar interaction in the ZFMBs is present.

In summary, this study shows that magnetic interparticle interactions are closely related to the geometrical arrangement of MNPs and affect magnetic properties, which

opens up the possibility for fine tuning magnetic properties. For example, while strong dipolar interaction in ZFMBs led to anisotropic energy barrier enhancement, ZFMBs still retain superparamagnetism, like ZFNPs, at room temperature. Since a single ZFMB consists of many individual ZFNPs, the magnetic moment of an individual ZFMB is on a par with a collective summation of magnetic moments of the individual ZFNPs clustered. Consequently, ZFMBs could be superior to individual MNPs for applications such as magnetic labels in biosensors, magnetically assisted drug delivery, and biomolecular separation. We believe that producing colloidal assemblies of MNPs could be an excellent way to develop new materials with desired magnetic properties for a specific application.

3.5 References

(1) Jun, Y.-w.; Seo, J.-w.; Cheon, J., *Acc. Chem. Res.* **2008,** *41*, 179-189.

(2) Itoh, H.; Sugimoto, T., *J. Colloid Interface Sci.* **2003,** *265*, 283-295.

(3) Noh, S.-h.; Na, W.; Jang, J.-t.; Lee, J.-H.; Lee, E. J.; Moon, S. H.; Lim, Y.; Shin, J.-S.; Cheon, J., *Nano Lett.* **2012,** *12*, 3716-3721.

(4) Stoner, E. C.; Wohlfarth, E., *Phil. Trans. R. Soc. A* **1948,** *240*, 599-642.

(5) Parkin, S.; Bhadra, R.; Roche, K., *Phys. Rev. Lett.* **1991,** *66*, 2152.

(6) Skumryev, V.; Stoyanov, S.; Zhang, Y.; Hadjipanayis, G.; Givord, D.; Nogues, J., *Nature* **2003,** *423*, 850-853.

(7) Meiklejohn, W. H.; Bean, C. P., *Phys. Rev.* **1957,** *105*, 904.

(8) Lavorato, G. C.; Peddis, D.; Lima Jr, E.; Troiani, H. E.; Agostinelli, E.; Fiorani, D.; Zysler, R. D.; Winkler, E. L., *J. Phys. Chem. C* **2015,** *119*, 15755-15762.

(9) Dormann, J.; Cherkaoui, R.; Spinu, L.; Nogues, M.; Lucari, F.; D'Orazio, F.; Fiorani, D.; Garcia, A.; Tronc, E.; Jolivet, J., *J. Magn. Magn. Mater.* **1998,** *187*, L139-L144.

(10) Lu, Z.; Yin, Y., *Chem. Soc. Rev.* **2012,** *41*, 6874-6887.

(11) Mørup, S., *EPL (Europhysics Letters)* **1994,** *28*, 671.

(12) Victora, R.; Peng, W.; Xue, J.; Judy, J., *J. Magn. Magn. Mater.* **2001,** *235*, 305-311.

(13) Kostopoulou, A.; Brintakis, K.; Vasilakaki, M.; Trohidou, K.; Douvalis, A.; Lascialfari, A.; Manna, L.; Lappas, A., *Nanoscale* **2014,** *6*, 3764-3776.

(14) Muscas, G.; Kumar, P. A.; Barucca, G.; Concas, G.; Varvaro, G.; Mathieu, R.; Peddis, D., *Nanoscale* **2016,** *8*, 2081-2089.

(15) Dai, Q.; Lam, M.; Swanson, S.; Yu, R.-H. R.; Milliron, D. J.; Topuria, T.; Jubert, P.-O.; Nelson, A., *Langmuir* **2010,** *26*, 17546-17551.

(16) Zeng, H.; Li, J.; Wang, Z. L.; Liu, J. P.; Sun, S., **2002**.

(17) Park, J.; Porter, M. D.; Granger, M. C., *Langmuir* **2015,** *31*, 3537.

(18) Gross, A. F.; Diehl, M. R.; Beverly, K. C.; Richman, E. K.; Tolbert, S. H., *J. Phys. Chem. B* **2003,** *107*, 5475-5482.

(19) Morales, M.; Munoz-Aguado, M.; Garcıa-Palacios, J.; Lázaro, F.; Serna, C., *J. Magn. Magn. Mater.* **1998,** *183*, 232-240.

(20) Bai, F.; Wang, D.; Huo, Z.; Chen, W.; Liu, L.; Liang, X.; Chen, C.; Wang, X.; Peng, Q.; Li, Y., *Angew. Chem. Int. Ed.* **2007,** *46*, 6650-6653.

(21) Zhuang, J.; Wu, H.; Yang, Y.; Cao, Y. C., *Angew. Chem. Int. Ed.* **2008,** *47*, 2208-2212.

(22) Peddis, D.; Cannas, C.; Musinu, A.; Ardu, A.; Orru, F.; Fiorani, D.; Laureti, S.; Rinaldi, D.; Muscas, G.; Concas, G., *Chem. Mater.* **2013,** *25*, 2005-2013.

(23) Qiu, P.; Jensen, C.; Charity, N.; Towner, R.; Mao, C., *J. Am. Chem. Soc.* **2010,** *132*, 17724-17732.

(24) Xing, R.; Wang, X.; Zhang, C.; Wang, J.; Zhang, Y.; Song, Y.; Guo, Z., *J. Mater. Chem.* **2011,** *21*, 11142-11149.

(25) Rruff Project. http://rruff.info/.

(26) Wohlfarth, E., *J. Appl. Phys.* **1958,** *29*, 595-596.

(27) Che, X.-d.; Bertram, H. N., *J. Magn. Magn. Mater.* **1992,** *116*, 121-127.

(28) Imagej (Image Processing and Analysis in Java). https://imagej.nih.gov/ij/.

(29) Hua, Q.; Huang, W., *J. Mater. Chem.* **2008,** *18*, 4286-4290.

(30) Fleet, M., *Acta Crystallogr. Sect. B* **1981,** *37*, 917-920.

(31) De Faria, D.; Venâncio Silva, S.; De Oliveira, M., *J. Raman Spectrosc.* **1997,** *28*, 873-878.

(32) Boucherit, N.; Hugot-Le Goff, A.; Joiret, S., *Corros. Sci.* **1991,** *32*, 497-507.

(33) Cullity, B. D.; Graham, C. D., *Introduction to Magnetic Materials*. John Wiley & Sons: 2011.

(34) Chien, C., *J. Appl. Phys.* **1991,** *69*, 5267-5272.

(35) Fannin, P.; Charles, S., *J. Phys. D: Appl. Phys.* **1994,** *27*, 185.

(36) Buschow, K. H. J., *Handbook of Magnetic Materials*. Elsevier: 2003; Vol. 15.

(37) Sahoo, Y.; Cheon, M.; Wang, S.; Luo, H.; Furlani, E.; Prasad, P., *J. Phys. Chem. B* **2004,** *108*, 3380-3383.

(38) Hansen, M. F.; Mørup, S., *J. Magn. Magn. Mater.* **1999,** *203*, 214-216.

(39) Béalle, G. l.; Di Corato, R.; Kolosnjaj-Tabi, J.; Dupuis, V.; Clément, O.; Gazeau, F.; Wilhelm, C.; Ménager, C., *Langmuir* **2012,** *28*, 11834-11842.

(40) Luis, F.; Petroff, F.; Torres, J.; García, L.; Bartolomé, J.; Carrey, J.; Vaurès, A., *Phys. Rev. Lett.* **2002,** *88*, 217205.

(41) Mamiya, H.; Ohnuma, M.; Nakatani, I.; Furubayashi, T., *Phys. Status Solidi A* **2004,** *201*, 3345-3349.

(42) Cannas, C.; Musinu, A.; Piccaluga, G.; Fiorani, D.; Peddis, D.; Rasmussen, H. K.; Mørup, S., *J. Chem. Phys.* **2006,** *125*, 164714.

(43) O'Grady, K.; El-Hilo, M.; Chantrell, R., *IEEE Trans. Magn.* **1993,** *29*, 2608-2613.

CHAPTER 4

COLLOIDALLY ASSEMBLED ZINC FERRITE MAGNETIC BEADS: SUPERPARAMAGNETIC LABELS WITH HIGH MAGNETIC MOMENTS FOR MAGNETORESISTIVE SENSOR

Reprinted with permission from Park, J.; Porter, M. D.; Granger, M. C., Colloidally Assembled Zinc Ferrite Magnetic Beads: Superparamagnetic Labels with High Magnetic Moments for MR Sensors. ACS Applied Materials & Interfaces 2017, 9 (23), 19569–19577.

4.1 Introduction

The design, synthesis, and surface functionalization of magnetic particles have been extensively researched due to their use in a number of technologies, including magnetic fluids,[1] data storage,[2] catalysis,[3] bioseparations,[4] biosensing,[5] and *in vivo/in vitro* theranostics.[6-7] With respect to the focus of this paper, magnetic particles are used as labels in solid-phase immunoassays that rely on magnetoresistive (MR) sensors for readout.[8-10] To serve as ideal labels, magnetic particles should have a high magnetic susceptibility, high magnetic moment per particle (***m***), and low degree of remanent magnetization and

coercivity. These particles should also be easily coated with antibodies and other molecular recognition element (MRE) to selectively tag the target analyte, while avoiding complications from aggregation and sedimentation.[7, 11] These characteristics are directly linked to metrics of analytical performance, including sensitivity, specificity, limits of detection, dynamic range, and measurement reproducibility.

There are two types of magnetic particles commonly used as labels: magnetic microbeads (μMBs) and magnetic nanoparticles (MNPs). μMBs consist of uniformly sized polymer spheres that are 1 to 5 μm in diameter and contain randomly dispersed nanometer-sized magnetic crystals, typically iron oxides (15-35% by weight).[9] Due to the large volume per μMB, a large $\boldsymbol{m}$ can be achieved, which translates to a large magnetic response. Values of $\boldsymbol{m}$ for μMBs typically range from 10^{-13} to 10^{-10} *emu*, and are much larger than those ($\leq 10^{-15}$ *emu*) of most MNPs.[12-14] Furthermore, a number of μMBs exhibit superparamagnetic behavior, which indicates that the likelihood of magnetic-induced aggregation under ambient conditions is low.[7] As a result, μMBs have been used in several studies on magnetic labeling and separations.[15-17] However, the high mass of a μMB can result in their ballistic deposition onto an assay surface, leading to an excessive level of nonspecific adsorption.[18-19] The large size of μMBs can also sterically screen neighboring binding sites on a capture surface, limiting the dynamic range of the assay.[20]

MNPs, which typically range from 5 to 100 nm in diameter, are an alternative to μMBs. Most of the studied MNPs are iron oxide nanoparticles (IONPs) (*e.g.*, Fe_3O_4 and γ-Fe_2O_3), ferrites (*e.g.*, MFe_2O_4, M = Co, Ni, Mn, and Zn), and metallic nanoparticles (*e.g.*, Fe, Co, and alloys thereof).[21] The size of MNPs more closely matches that of DNA, proteins, and other targets, which reduces the impact of steric screening.[10, 20, 22] However,

MNPs have a smaller ***m*** than µMBs, necessitating the use of a more sensitive detection system. There are two common approaches to increasing ***m*** of MNPs: increases in size and use of ferro- or ferrimagnetic materials. Larger MNPs have a larger ***m*** but have a size bound by the superparamagnetic limit (≤150 nm).[21] Above this size limit, the magnetic interactions between MNPs are strong enough to cause aggregation. MNPs synthesized from ferro-/ferrimagnetic materials can also have a high ***m***, but must be stabilized by surface coatings to combat strong magnetic interparticle coupling.[23-24]

Our interest in this area stems from the use of nanoparticles as labels in a diagnostic tool for the detection of disease markers that is based on giant-magnetoresistance (GMR).[25-29] In previous work, we demonstrated that streptavidin-coated µMBs (Dynabeads®) bound to biotinylated gold addresses can be quantitatively measured using a scanning GMR readout method which mimics that used for hard-disk drives.[27-28] In our approach, the separation distance between assay substrate and GMR sensor is on the order of micrometers (10 to 50 µm)[27, 30] as opposed to tens or hundreds of nanometers found in other GMR sensors.[7-9, 12] Since the magnetic dipole field of magnetic particles decreases rapidly with distance (*i.e.*, a decrease proportional to $1/r^3$, where r is the separation between particle and sensor),[29] this architecture places a heavy emphasis on the use of MNP labels with a large ***m*** for low level detection. We have also found that the ballistic settling of µMBs can complicate the assay by inducing a larger level of nonspecifically adsorbed µMBs than that found with MNPs. As evident, the synthesis and design of superparamagnetic nanoparticle labels with a high ***m*** stand as an on-going need in order to realize effective magnetic labeling.

One option for preparing superparamagnetic particles with a large ***m*** is to create

colloidally assembled magnetic beads (Coll-MBs). By Coll-MBs, we are referring nanoparticle clusters that, when assembled together to form a larger particle, have a much higher ***m*** than that of the individual MNPs and remain superparamagnetic at the same time.[31-37] Several different types of Coll-MBs have been successfully synthesized by using solvothermal methods,[36, 38-39] amphiphilic polymer encapsulation,[32] emulsion-based bottom-up assembly,[31] and controlled induction of solvophobic interactions.[37, 40] Among other methods, the emulsion-based assembly method allows to use small nanoparticles as building blocks and create larger particles to realize new physical/chemical properties for many applications. Recent work has shown the possibility of incorporating plasmonic or fluorescent nanoparticles into the assembly for use in magnetic resonance imaging agents, hyperthermic treatment, and other theranostic applications.[32-33, 41] Most of the Coll-MBs synthesized to date are composed of IONPs,[33-34, 41-42] which provides the opportunity for further increase in the ***m*** of Coll-MBs by using seed MNPs with a larger ***m***.

The work described herein takes an emulsion-based assembly tactic for the preparation of Coll-MBs with a higher ***m*** by using zinc ferrite nanoparticles (ZFNPs). To this end, ZFNPs, which have an inherently larger ***m*** than IONPs, were prepared via thermal decomposition and then used as seeds for forming colloidally assembled zinc ferrite magnetic beads (ZFMBs). The ZFMBs were subsequently functionalized with a layer of polyacrylic acid and conjugated with streptavidin by carbodiimide linking chemistry. The product at each step in the procedure was characterized by electron microscopy, energy-dispersive X-ray spectroscopy, infrared spectroscopy, magnetometry, and dynamic light scattering. The streptavidinated ZFMBs were also compared to two streptavidinated magnetic particles, Dynabeads® and Turbobeads®, in terms of their magnetic properties

and colloidal stability. Finally, the streptavidinated ZFMBs were used as magnetic labels in sandwich immunoassays for the detection of osteopontin (OPN), a potential pancreatic cancer marker, and compared assays carried out using Dynabeads. We believe that the approach and materials presented in this paper can potentially serve as the basis for a new class of superparamagnetic labels with a large ***m*** for magnetic immunoassays, as well as for other biological applications (*e.g.*, magnetic separation and theranostics).

4.2 Experimental Section

4.2.1 Materials

Iron acetylacetonate ($Fe(acac)_3$), zinc acetylacetonate ($Zn(acac)_2$), oleylamine, ethylene glycol, benzyl ether, and chloroform were acquired from Acros organics (USA). Oleic acid and poly(acrylic acid) (PAA, MW ~5.1 kDa) were purchased from Alfa Aesar (USA) and Fluka (Japan), respectively. Poly(vinylpyrrolidone) (PVP, MW ~50 kDa), poly(vinylalcohol) (PVA, MW 30−70 kDa), bovine serum albumin (BSA), sodium phosphate (monobasic and dibasic), 2-(N-morpholino)ethanesulfonic acid (MES), and dodecyltrimethylammonium bromide (DTAB) were obtained from Sigma Aldrich (USA). Streptavidin, 1-ethyl-3-(3-dimethylaminopropyl)carbodiimide (EDC), N-hydroxysuflosuccinimide (sulfo-NHS), dithiobis(succinimidyl propionate) (DSP), and modified Dulbecco's phosphate-buffered saline packs (10 mM PBS) were acquired from Thermo Scientific (USA). Dynabeads® (Streptavidin, MyOne C1) and FITC-avidin were purchased from Invitrogen (USA). Streptavidin-conjugated Turbobeads® were obtained from TurboBeads (Switzerland). Monoclonal human osteopontin (OPN) antibody (Catalog no. MAB14332, clone no. 22312), recombinant human OPN protein (32.9 kDa, catalog

no.1433-OP), and biotinylated polyclonal human OPN antibody (Catalog no. BAF1433) were acquired from R&D Systems (USA). Phosphate-buffered saline/casein block (5× concentrate) was purchased from Surmodics (USA).

4.2.2 Synthesis of MNP Seeds

ZFNPs and IONPs were synthesized by slight modifications to published procedures.[43-44] For ZFNPs, 1.3 mmol $Fe(acac)_3$, 0.3 mmol $Zn(acac)_2$, and 2.1 mL of neat oleic acid and oleylamine were added to 20 mL of benzyl ether; this mixture was then refluxed at 290 ˚C for 1 h under an inert atmosphere. IONPs were synthesized by using the same set of conditions, but without $Zn(acac)_2$. The resulting particles were then thoroughly cleaned with a mixture (3:1 v/v) of acetone and hexane by centrifugation (10200*g* and 10 min) and drying under vacuum. The dried particles were resuspended in 5.0 mL chloroform at ~20 mg/mL.

4.2.3 Synthesis of Coll-MBs of ZFNPs and IONPs

The procedure of Cao et al. was modified for the synthesis of the Coll-MBs of ZFNPs and IONPs, as shown in Figure 4.1.[37] Briefly, 1.0 mL of ZFNPs, suspended in chloroform, was added to 1.0 mL DTAB solution (aq., 20 mg/mL) in a 5 mL centrifuge tube and vortexed for 5 min. The emulsion was transferred to a round-bottom flask that was immersed in a 40 ˚C water bath, and chloroform was removed by purging with nitrogen. The DTAB-stabilized Coll-MBs were then injected into another round bottom flask that contained 5.0 mL PVP solution (0.55 g PVP dissolved in 5.0 mL ethylene glycol), and this suspension was magnetically stirred for 10 min and annealed at 80 ˚C for 6 h under nitrogen.

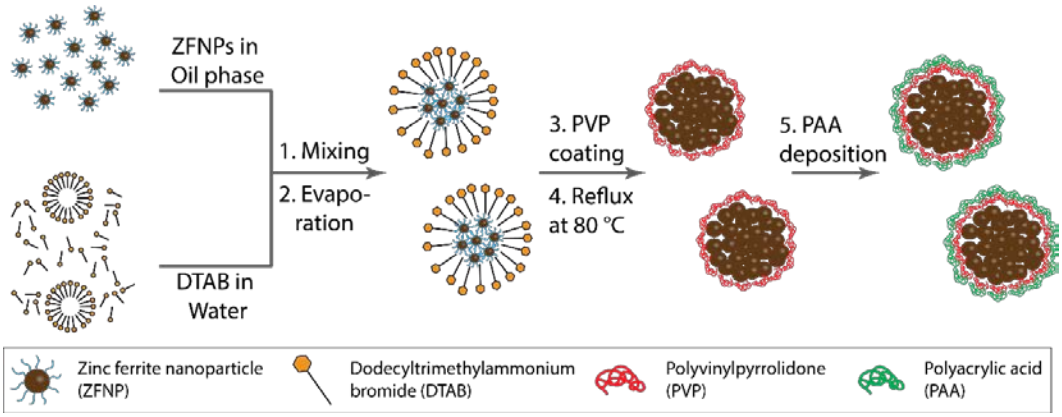

Figure 4.1 Schematic illustration of the synthesis of ZFMBs: (1) The oil-in-water emulsion was prepared by mixing ZFNPs with DTAB solution; (2) the oil phase was selectively evaporated; (3) DTAB-stabilized Coll-MBs coated with PVP; (4) refluxing at 80 °C for 6 h; and (5) PAA layer deposition.

The PVP-coated ZFMBs (ZFMBs@PVP) were centrifuged at 5500*g* for 30 min. Next, the precipitate was rinsed twice with ethanol, followed by centrifugation. The ZFMBs@PVP were resuspended in 10 mL EtOH at ~2 mg/mL. The same procedure was used in the synthesis of colloidal assemblies of IONPs (IOMBs@PVP).

4.2.4 Polymer Coating and Streptavidin Conjugation

The as-synthesized ZFMBs were also functionalized with a layer of PAA, followed by protein conjugation via carbodiimide linking chemistry. First, 0.5 mL of ZFMBs@PVP in ethanol were mixed with 1.0 mL of aqueous PAA solution (10 mg/mL). The mixture was sonicated for 10 min and mixed using an orbital mixer for 12 h. The PAA-coated ZFMBs (ZFMBs@PVP@PAA) were rinsed with deionized water (DI H_2O) three times, followed each time by centrifugation and resuspension in 1.0 mL DI H_2O.

Streptavidin conjugation was carried out using a two-step process with EDC/sulfo-NHS. First, 1.0 mL of ZFMBs@PVP@PAA was centrifuged at 5150 *g* for 3 min and

resuspended in 1.0 mL of 5 mM MES buffer (pH 6.5). EDC and sulfo-NHS solution (20 and 10 mg/mL, respectively) were prepared in 25 mM MES buffer (pH 6.5 and 4 ˚C). ZFMBs@PVP@PAA were reacted by adding 50 μL EDC and 100 μL sulfo-NHS and incubating for 30 min at room temperature. The particles were then confined to the wall of the centrifuge tube using with a 1-cm^3 neodymium magnet and the supernatant of unreacted EDC and sulfo-NHS was removed by decanting. This step was repeated once. The particles were then resuspended in 1.0 mL of 5 mM MES, followed by the addition of 60 μL streptavidin (2.5 mg/mL in DI H_2O). This suspension was agitated for 2 h, and residual streptavidin was removed by centrifugation (2400*g* and 2 min). Finally, the streptavidinated ZFMBs (ZFMBs@PVP@PAA@SA) were suspended in 1.0 mL of 10 mM phosphate buffer (pH 7.4) containing 70 mM NaCl and 0.2% (w/v) PVA as a blocking agent.

4.2.5 Assay Substrate Design, MR Sensor Configuration, and Signal Analysis

Detailed procedures for the fabrication of the assay substrate, the MR sensor configuration, substrate readout, and signal analysis are described in the Supporting Information and elsewhere.[27-28, 30]

4.2.6 Magnetic Sandwich Immunoassay for the Detection of a Potential Pancreatic Cancer Marker

4.2.6.1 Immobilization of capture antibody. Assay substrates shown in Figure C1.1D were created using photolithographic and metal lift-off processes.[27-28] Prior to the immobilization of the capture antibody, the substrates were etched in an oxygen plasma (Oxford 80 RIE) in order to remove residual photoresist. Etching was performed at 150 W for 6 min under 50 sccm O_2. The substrates were then sonicated in acetone for 10 min, and rinsed with ethanol. The next step immersed the substrates in an ethanolic 1 mM DSP solution for 1 h to modify the Au addresses. After DSP modification, the substrates were rinsed with ethanol and dried with a stream of nitrogen. Next, a 40 μL droplet of 20 μg/mL monoclonal human OPN antibody in 10 mM phosphate-buffered saline (PBS, pH 7.4) was applied on top of each substrate and stored in a humidified chamber for 2 h. Subsequently, each substrate was transferred into a well of a 12-well plate and blocked with 1.0 mL of 20% (v/v) casein blocking solution in PBS for 1 h to combat nonspecific adsorption.

4.2.6.2 Antigen capture and labeling steps. A dilution series of recombinant human OPN (0, 0.5, 1.0, 5.0, 10, and 50 ng/mL) was prepared in 10 mM PBS and 1.0% BSA. These antigen solutions (1.0 mL each) were applied to separate capture substrates, allowed to incubate for 2 h, and rinsed with 10 mM PBS three times. The next step added biotinylated polyclonal human OPN detection antibody (0.5 μg/mL in 10 mM PBS containing 1.0% BSA) to each well, and then incubated for 2 h, and rinsed with 10 mM PBS three times. For labeling, a small droplet (40 μL) of magnetic label suspension was applied onto each substrate, fully covering the top of the substrate. The average concentrations of Dynabeads and streptavidinated ZFMBs were estimated to be 5×10^8

and 7×10^{10} beads/mL, respectively, by using nanoparticle tracking analysis. The labeling step was allowed to continue for 1 h in a humidified chamber, and the unbound labels were subsequently rinsed three times with 5 mM borate buffer containing 150 mM NaCl, followed by a final rinse with DI H_2O.

4.3 Results and Discussion

4.3.1 Synthesis and Characterization of Seed MNPs

Most of the Coll-MBs studied to date were prepared using IONPs,[31-33, 37, 40] which suggests the possibility to further increase in ***m*** by replacing IONPs with other MNPs of different composition. Recent work has shown that the magnetization of Fe_3O_4 nanoparticles can be increased by introducing zinc in the interstices of the inverse spinel structure of Fe_3O_4.[23, 45] This inspired us to explore the synthesis of ZFNPs as a means to create Coll-MBs with a high ***m***. Shown in Figure 4.2A and Figure C.3 is electron micrographs of ZFNPs prepared as detailed in the experimental section. These ZFNPs shown in Figure 4.2A have an average diameter of 9.3 ± 1.6 nm. Most of the ZFNPs are spherical in shape, but some faceted ZFNPs are also evident upon closer inspection using TEM (Figure C.3). The EDS spectrum of as-synthesized ZFNPs (Figure C.3C) has the Kα and Lα peaks of Zn at 8.63 and 1.01 eV, respectively, which confirms the presence of Zn. An analysis of these EDS data yields a Zn:Fe molar ratio of 4.5:95.2 and agrees with the molar ratio determined by inductively coupled-plasma mass spectroscopy (ICP-MS) given in the inset of Figure C.3C (Zn:Fe = 5.5:94.5).

The magnetic hysteresis curves in Figure 4.2B show that ZFNPs and IONPs are

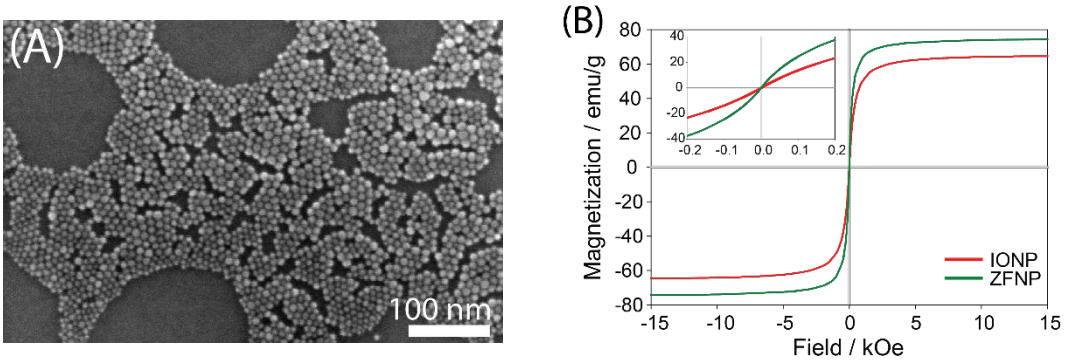

Figure 4.2 (A) SEM image of as-synthesized ZFNPs. (B) Hysteresis curves of IONPs and ZFNPs, measured at room temperature. The inset presents hysteresis curves at low fields.

superparamagnetic at room temperature (*i.e.*, remanent magnetization and coercivity of both particles are essentially zero). As expected, the saturation magnetization ($\boldsymbol{M_s}$) of ZFNPs (74 emu/g) is higher than that of IONPs (65 emu/g). The $\boldsymbol{M_s}$ value of our ZFNPs is comparable to those of MNPs of similar compositions, reported in literature.[46-48] More importantly, the magnetization of ZFNPs (24.5 emu/g) is almost twice that of the IONPs (13.4 emu/g) at an applied field of 100 Oe, the magnetic field we use to carry out measurement with.

4.3.2 Synthesis and Characterization of ZFMBs

Colloidal assemblies of ZFNPs were synthesized as described in Figure 4.1. Briefly, an oil-in-water emulsion is produced by mixing ZFNPs in chloroform with DTAB solution. The selective evaporation of chloroform produces spherical assemblies of ZFNPs. The resulting assemblies are subsequently coated with PVP. By changing the amount of DTAB for a fixed concentration of ZFNPs, the average diameter of the ZFMBs can be tuned as shown in Figure C.4. The as-synthesized ZFMBs (*i.e.*, ZFMBs@PVP) in Figure 4.3A are spherical in shape and have a diameter of 163 ± 46 nm (n=250), which is determined from

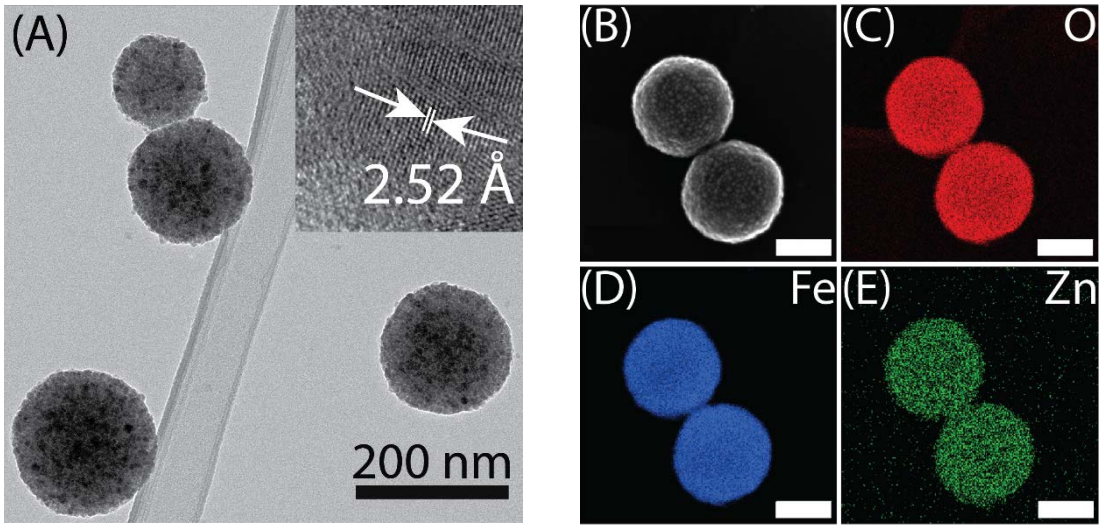

Figure 4.3 (A) TEM image of ZFMBs@PVP. Inset is a high resolution TEM image showing lattice spacing. (B) Image of as-synthesized ZFMBs obtained by using STEM mode. Scale bar is 100 nm. (C, D, and E) EDS mapping of ZFMBs@PVP, displaying the elemental distribution of oxygen, iron, and zinc. Scale bars are 100 nm.

SEM images (Figure C.4). The TEM lattice fringes for the ZFNPs that make up the ZFMBs are clearly evident, as shown in the inset of Figure 4.3A; this indicates that the ZFNPs are crystalline with a *d*-spacing of 2.52 Å, which corresponds to the (311) plane of the inverse spinel structure of magnetite (Fe_3O_4).[49]

ZFNPs. It is estimated that roughly 5,000 seed particles are clustered into a single assembly based on the average sizes of ZFNPs and ZFMBs (*i.e.*, the volume of a single ZFMB is divided by that of a single ZFNP, assuming that no dead volume is present between ZFNPs in a ZFMB). The EDS maps of the ZFMBs in Figures 4.3C, D, and E confirm that Zn is present in the inverse spinel structure of ZFNPs. The packing of ZFNPs in these ZFMBs@PVP was examined by electron microscopy and electron diffraction studies (Figure C.5). Unlike the superparticles reported in literature,[33-34, 37] the superlattice fringes of ZFNPs (like atomic lattice fringes) were not observed during SEM and TEM imaging for ZFMBs@PVP. Moreover, the electron diffraction data in Figure C.5B shows

a ring-pattern rather than exhibiting single-crystal-like electron diffraction patterns (*i.e.*, spots). We, therefore, conclude that ZFNPs are assembled randomly into a spherical bead rather than in an fcc superlattice of nanoparticles as has been found for other superparticles.

The magnetic hysteresis curves for the two Coll-MBs (ZFMBs@PVP and IOMBs@PVP) in Figure 4.4 were measured at room temperature using VSM. The $\boldsymbol{M_s}$ of the ZFMBs@PVP (72 emu/g) is not significantly different from that of the ZFNPs (74 emu/g). Over the field range of 100 to 150 Oe, the ZFMBs@PVP still demonstrate higher magnetization (21.5−27.4 emu/g) than IOMBs@PVP (9.3−12.7 emu/g) as shown in the inset of Figure 4.4. Interestingly, the ZFMBs@PVP remain superparamagnetic, which means that clustering of a large number of ZFNPs into a single ZFMB has little detectable impact on superparamagnetism of the individual particles at room temperature. More importantly the estimates in Table C.1 show that the ZFMBs have a much higher $\boldsymbol{m}$ (2.3×10^{-13} emu/bead at 100 Oe) than that of a single ZFNP (5.4×10^{-17} emu/particle at 100 Oe); this arises from the collective interaction of magnetic moments of ZFNPs in a single ZFMB@PVP.[32]

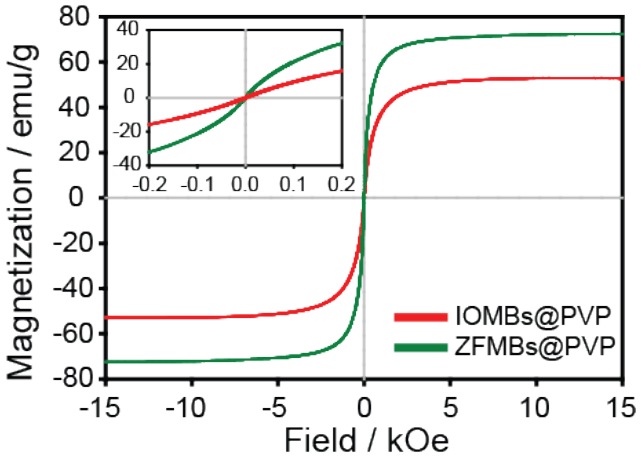

Figure 4.4 Magnetic hysteresis curves of IOMBs@PVP and ZFMBs@PVP.

4.3.3 Functionalization of ZFMBs@PVP with a Layer of PAA

The use of magnetic particles as labels relies on the ability of the labels to recognize and target an analyte of interest.[11] Moreover, particles with smaller sizes are more colloidally stable and have a higher label density on a surface (*i.e.*, a large number of labels bound on a surface), which leads to improved analytical sensitivity and dynamic range in an immunoassay.[20, 50] Therefore, we examined the use of ZFMBs@PVP (average size of ~160 nm) as magnetic labels, recognizing that there is always trade space between colloidal stability, the magnetic moment of magnetic labels, and assay performance.

For this purpose, the particles were first coated with a layer of PAA by incubating ZFMBs@PVP in a PAA solution.[23, 51] Evidence for deposition of PAA is presented by the IR spectra and ζ-potential measurements presented in Figure 4.5 and Figure 4.6A, respectively. A strong band at 580 cm^{-1} (not shown) was observed in all samples, and is associated with Fe−O phonon vibrations of the ZFNPs.[52] The features between 1664−1645 and 1462−1424 cm^{-1} in the ZFMBs@PVP spectrum are assigned to carbonyl (C=O) stretching mode of the pyrrolidone group and CH_2 scissor mode, respectively, in the PVP coating.[53] After PAA deposition, the presence of carboxylic acid was observed in theZFMBs@PVP@PAA spectrum: there are bands around 1413 cm^{-1} and 1710−1690 cm^{-1}, which are symmetric carboxylate (COO^-) stretching and carbonyl (C=O) stretching, respectively, of PAA.[54] In addition, the negative ζ-potential value, shown in Figure 4.6A, of the ZFMBs@PVP@PAA at pH 6.5 results from deprotonation of the carboxylic acid groups in the adsorbed PAA layer. These data support the successful coating of PAA on ZFMBs@PVP.

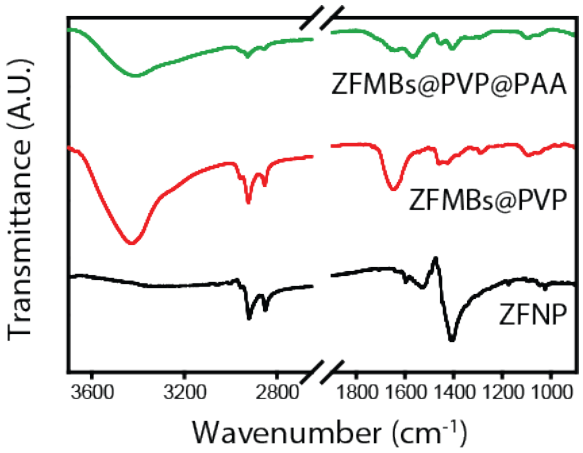

Figure 4.5 IR spectra of ZFNPs, ZFMBs@PVP, and ZFMBs@PVP@PAA.

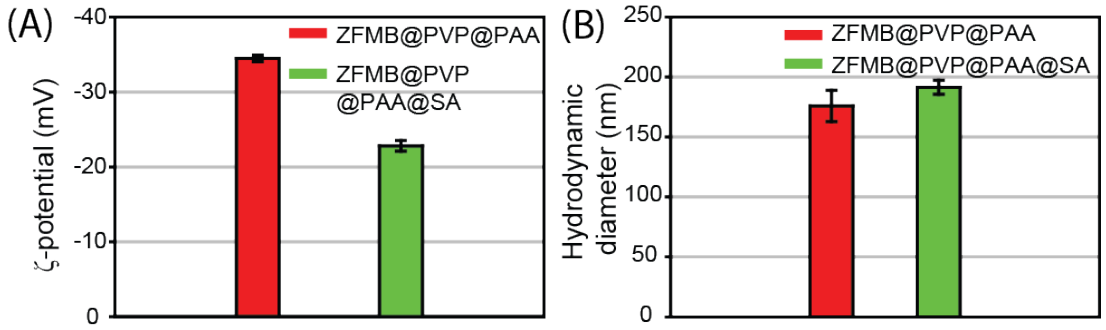

Figure 4.6 (A) ζ-potential and (B) hydrodynamic size changes before and after streptavidin immobilization. Note that all particle samples for the measurement were suspended in 5 mM MES (pH 6.5).

4.3.4 Streptavidin Conjugation via Carbodiimide Chemistry

Streptavidin (SA), a biotin-binding protein, was immobilized on ZFMBs@PVP@PAA by using carbodiimide chemistry (EDC and Sulfo-NHS). SA is frequently used as an MRE due to its high affinity for biotin with a dissociation constant ($\boldsymbol{K_D}$) in the range of 10^{-15} to 10^{-12} M.[55-57] We found that when EDC was used together with sulfo-NHS, the activated ZFMBs@PVP@PAA was more colloidally stable compared to when only EDC was used; one-step carbodiimide chemistry (*i.e.*, using EDC only) often led to particle aggregation and irreproducible SA conjugation. This is attributed to the

presence of the negatively charged sulfonate group (SO_3^-) in sulfo-NHS which combats particle aggregation by electrostatic repulsion.[58]

The conjugation of SA, a ~60 kDa tetramer, was characterized with DLS through changes in hydrodynamic sizes and ζ-potentials and by fluorescent microscopy. The ζ-potential of suspended particles corresponds to the electrical potential at the slipping plane around the surface of the particles.[59] As shown in Figure 4.6A, the ζ-potential of ZFMBs@PVP@PAA in 5 mM MES (pH 6.5) is −35 ± 1 mV. When SA was conjugated to the particles, the ζ-potential increases to −23 ± 1 mV. This change in ζ-potential is consistent with expectation based on the isoelectric point (pI ~6.5) of SA.[60] The change in hydrodynamic size in Figure 4.6B also follows expectations. The hydrodynamic size of the ZFMBs@PVP@PAA increased ~15 nm after SA conjugation. This change is consistent with the molecular volume of SA, which is ~105 nm^3.[61] Lastly, bright green fluorescence (Figure C.6) was observed when ZFMBs@PVP@PAA were conjugated with FITC modified-avidin using the same conjugation procedure. Taken together, these results indicate that SA was successfully immobilized on the surface of ZFMBs@PVP@PAA.

4.3.5 Comparison of Streptavidinated ZFMBs to Commercialized Magnetic Labels

Prior to performing assays with our new particles, the magnetic properties and colloidal stability of the streptavidinated ZFMBs (*i.e.*, ZFMBs@PVP@PAA@SA) were compared to two commercially available streptavidin-coated magnetic particles, Dynabeads and Turbobeads. Presented in Figure C.7 are SEM images for both particles. Dynabeads are 1.05-μm spherical polymer beads with ~35% embedded iron oxide

nanocrystals.[62] Turbobeads are composed of ferromagnetic cobalt@carbon core-shell metallic MNPs with an average diameter of 30 nm.[63-65] Magnetic hysteresis measurements in Figure 4.7A show that Turbobeads have high $\boldsymbol{M_r}$ and $\boldsymbol{H_c}$ (9.3 emu/g and 254 Oe, respectively) at room temperature, whereas the Dynabeads and ZFMBs@PVP@PAA@SA have both $\boldsymbol{H_c}$ and $\boldsymbol{M_r}$ near zero. The $\boldsymbol{M_s}$ values for the Dynabeads, Turbobeads, and ZFMBs@PVP@PAA@SA at a field of 15 kOe are 24, 45, and 67 emu/g, respectively. Note that our measured $\boldsymbol{M_s}$ for Turbobeads in Figure 4.7A is ~3× lower than that reported by the manufacturer (>150 emu/g). In conjunction with a recent report,[66] we attribute this observation, at least in part, to oxide formation on the surface of the cobalt nanoparticles, which leads to a decrease in $\boldsymbol{M_s}$. For magnetic label applications, a high $\boldsymbol{m}$ is more important than a high $\boldsymbol{M_s}$. While having the lowest $\boldsymbol{M_s}$ among three label candidates, Dynabeads, due to the large size, have the highest $\boldsymbol{m}$ (6.8×10^{-12} emu/bead at 100 Oe) when compared to the ZFMBs and Turbobeads of 2.4×10^{-13} emu/bead and 2.8×10^{-16} emu/particle, respectively (Table C.1). However, the steric hindrance from the larger size of Dynabeads can limit the number of labels that bind to a surface. This, in turn, affects the

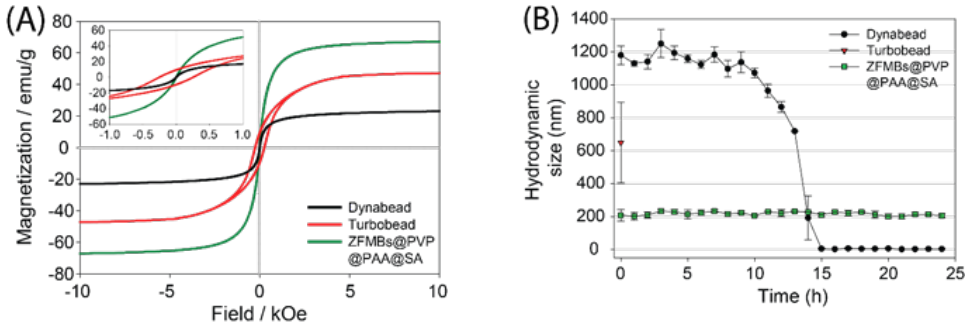

Figure 4.7 Comparison of (A) field-dependent magnetization, and (B) hydrodynamic size change of streptavidinated magnetic beads (Dynabeads, Turbobeads, and ZFMBs@PVP@PAA@SA). All particle samples for DLS measurement were suspended in 10 mM phosphate buffer at pH 7.4. Note that it was not possible to measure changes in hydrodynamic size of the Turbobeads due to aggregation.

attainable dynamic range.

To test colloidal stability, changes in the hydrodynamic size of the three magnetic labels were measured over 24 h by DLS. These results are presented in Figure 4.7B. The streptavidinated ZFMBs remained suspended over the entire 24 h period and held a constant hydrodynamic size, *i.e.*, no detectable aggregation. The hydrodynamic size of the Dynabeads also remained unchanged at ~1100 nm for ~8 h, but then dramatically decreased to near zero over the next 7 h. This implies that Dynabeads settle much faster than the streptavidinated ZFMBs. Note that the sedimentation of the Dynabeads resulted in incorrect measurements of the hydrodynamic size after ~10 h. Lastly, we were unable to measure a change in the hydrodynamic size of the Turbobeads, which rapidly aggregated due to strong magnetic forces between these ferromagnetic particles. Indeed, the as-received Turbobeads were aggregated upon arrival and they rapidly aggregated after sonication. Even when carrying out the very first measurement, the hydrodynamic size of the Turbobeads in Figure 4.7B is already much larger than its initial size. As a result, we only tested the utility of our streptavidinated ZFMBs and the Dynabeads as assay labels.

4.3.6 Magnetic Immunoassays for the Detection of a Potential Pancreatic Cancer Marker

To test the effectiveness of the Dynabeads and ZFMBs@PVP@PAA@SA, magnetic sandwich immunoassays for the detection of a potential pancreatic cancer marker, OPN, were carried out as illustrated in Figure 4.8 and analyzed using our MR sensor.

Presented in Figure 4.9 is the resulting dose-response curves. An MR response of ~3% of the sample blanks (*i.e.*, 0 ng/mL of OPN) was observed for both labels, which

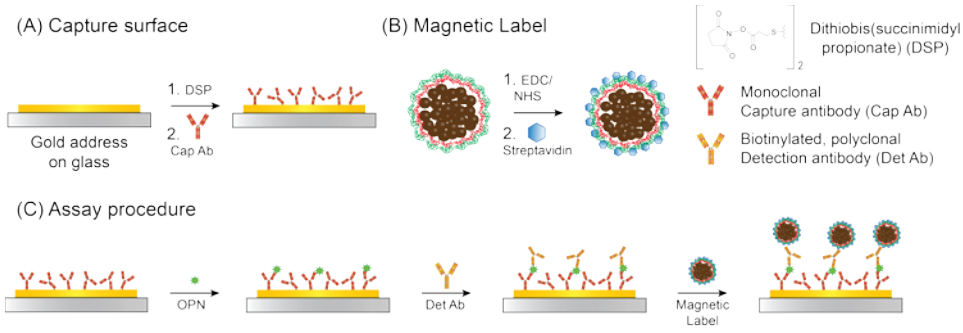

Figure 4.8 Schematic illustration of magnetic sandwich immunoassays: (A) Gold capture substrate preparation; (B) magnetic label preparation; and (C) major assay steps. The preparation of capture substrate and magnetic label were completed prior to the assay.

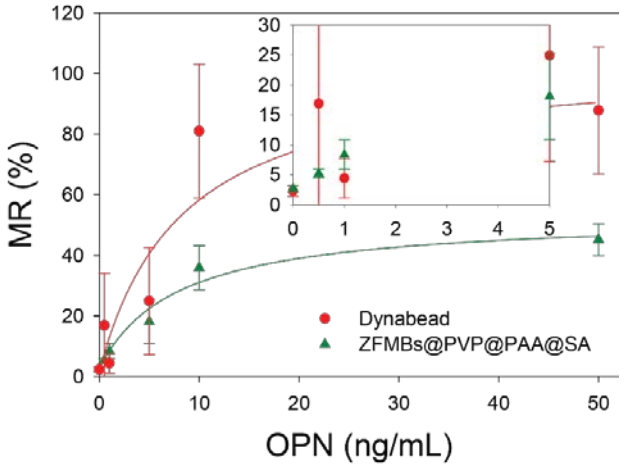

Figure 4.9 Dose-response curves of OPN assays performed with the Dynabeads and ZFMB labels. Each point represents the average of twelve MR responses from Au addresses in each substrate. The inset is the expanded dose-response curves at the concentration range of 0 to 5 ng/mL of OPN.

indicates that a degree of nonspecific adsorption for both magnetic labels exists. The MR responses for Dynabeads and ZFMB labels appear to level off at ~20 and 50 ng/mL of OPN, respectively. As shown in Figures 4.9, C.8, and C.9, the response using Dynabeads increases with OPN concentration. Due to the higher ***m*** for the Dynabeads, the MR responses are greater than those from the ZFMB labels. However, the use of the Dynabeads as magnetic labels in these assays suffers from two notable issues: (1) a more limited linear

dynamic range, and (2) a larger standard deviation in the MR responses. MR signals at the concentrations larger than 1 ng/mL then quickly increase, saturating at ~10 ng/mL. Similar dose-response curves with limited dynamic ranges have been observed when micron-sized beads were used as labels.[20, 67] In addition, the MR responses are not differentiable due to the large standard deviations when the OPN concentration is less than 5.0 ng/mL. As shown in the inset of Figure 4.9, the MR response at 0.5 ng/mL of OPN is higher than that at 1.0 ng/mL and shows a large standard deviation. This indicates that the number of the Dynabeads bound on assay surface significantly varies across address-to address (*i.e.*, inconsistent labeling between the gold addresses exists). Due to these limitations of Dynabeads, a calculation of the theoretical limit of detection (LoD, a signal at blank plus 3× standard deviation divided by the slope of the linear fit) was impossible. We speculate that a LoD is present between 5 to 10 ng/mL (80 to 160 pM) when the Dynabeads used as labels.

On the other hand, the MR response of the assay labeled with the ZFMB labels gradually increases with a OPN concentration up to ~50 ng/mL, as evident in Figure 4.9, C.10, and C.11. The average MR responses from the streptavidinated ZFMBs are smaller than those observed for the Dynabeads at the same OPN concentration, which is due to the ~30× lower ***m*** of the ZFMBs than that of the Dynabeads. However, MR responses increase with OPN concentration between 0 and 10 ng/mL; an OPN concentration less than 10 ng/mL can be evidently differentiated from each other. In addition, the ZFMB labels appear to be more uniformly distributed across the addresses, which is reflected in the smaller standard deviations of MR responses at all OPN concentrations. Given that the MR responses between 0 and 10 ng/mL of OPN are linear, the theoretical LoD of 0.5 ng/mL (8

pM) is calculated. The ZFMB labels, therefore, exhibit an improved detection limit for OPN and a wider linear dynamic range. De Palma et al. also reported that the performance of magnetic immunoassays in terms of dynamic range and analytical sensitivity can be improved by employing sub-micron sized magnetic labels.[20, 67]

We believe that the limited dynamic range, higher detection limit, and higher measurement deviation in the MR responses associated with the Dynabeads can be attributed to three possible factors. First, the analytes bound on an assay surface are tagged by larger particles (Dynabeads), which is screening neighboring binding sites and, subsequently, has a negative impact on labeling.[9, 20, 67] Second, the delivery of Dynabeads to the capture addresses is dominated by gravity-induced sedimentation, rather than by diffusion.[18-19] Third, the larger viscous drag forces exerted on the Dynabeads during rinsing steps can possibly detach a portion of the labels from the assay surface and, consequently, increase the measurement deviation.[59]

4.4 Conclusion

Magnetic labels play a critical role in determining the reproducibility and sensitivity of magnetic immunoassays. We utilized emulsion-based synthetic procedure to prepare colloidal assemblies of ZFNPs with a high ***m*** and superior colloidal stability. The colloidal assemblies (*i.e.*, ZFMBs@PVP) retain superparamagnetic, which prevents magnetically-induced aggregation in suspension. The ***m*** of ZFMBs@PVP (2.4×10^{-13} emu/bead at 100 Oe) is ~4,000× greater than their constituent ZFNPs (5.4×10^{-17} emu/particle at 100 Oe). The colloidal stability of the ZFMB labels is superior to the two commercial magnetic particles tested. Furthermore, the streptavidinated ZFMBs outperformed the Dynabeads in

an immunoassay for the detection of OPN in buffer, regarding dynamic range, LoD, and surface binding. We expect that the colloidally assembled ZFMBs developed herein will find uses beyond immunoassay labels, particularly in biological and theranostic applications where high ***m***, facile surface functionalization, and colloidal stability are needed.

As presented in this paper, creating nanoparticle assembly may allow to find new materials with desired chemical and physical properties. We, therefore, believe that novel multifunctional nanoparticle assemblies with new physiochemical properties can be developed by co-assembling different types of nanoparticles (*i.e.*, plasmonic, magnetic, and/or quantum dot nanoparticles). Currently, using the ZFMB labels and our MR sensor, we are working on the development of multiplexed immunoassays for the detection of potential pancreatic cancer markers in human serum.

4.5 References

(1) Berkovskiĭ, B.; Medvedev, V. F.; Krakov, M. S., Oxford University Press: USA, 1993.

(2) Ethirajan, A.; Wiedwald, U.; Boyen, H. G.; Kern, B.; Han, L.; Klimmer, A.; Weigl, F.; Kaestle, G.; Ziemann, P.; Fauth, K., *Adv. Mater.* **2007,** *19*, 406-410.

(3) Yoon, T.-J.; Lee, W.; Oh, Y.-S.; Lee, J.-K., *New J. Chem.* **2003,** *27*, 227-229.

(4) Aguilar-Arteaga, K.; Rodriguez, J.; Barrado, E., *Anal. Chim. Acta* **2010,** *674*, 157-165.

(5) Haun, J. B.; Yoon, T. J.; Lee, H.; Weissleder, R., *Wiley Interdiscip. Rev.: Nanomed. Nanobiotechnol.* **2010,** *2*, 291-304.

(6) Yoo, D.; Lee, J.-H.; Shin, T.-H.; Cheon, J., *Acc. Chem. Res.* **2011,** *44*, 863-874.

(7) Lee, H.; Shin, T.-H.; Cheon, J.; Weissleder, R., *Chem. Rev.* **2015,** *115*, 10690-10724.

(8) Baselt, D. R.; Lee, G. U.; Natesan, M.; Metzger, S. W.; Sheehan, P. E.; Colton, R. J., *Biosens. Bioelectron.* **1998,** *13*, 731-739.

(9) Graham, D. L.; Ferreira, H. A.; Freitas, P. P., *Trends Biotechnol.* **2004,** *22*, 455-462.

(10) Mulvaney, S. P., *Nat. Nanotechnol.* **2011,** *6*, 266-267.

(11) Laurentius, L. B.; Owens, N. A.; Park, J.; Crawford, A. C.; Porter, M. D., *Expert Rev. Mol. Diagn.* **2016,** *16*, 883-895.

(12) Ferreira, H.; Graham, D.; Freitas, P.; Cabral, J., *J. Appl. Phys.* **2003,** *93*, 7281-7286.

(13) Wang, W.; Wang, Y.; Tu, L.; Feng, Y.; Klein, T.; Wang, J.-P., *Sci. Rep.* **2014,** *4:5716*, 1-5.

(14) Häfeli, U. O.; Lobedann, M. A.; Steingroewer, J.; Moore, L. R.; Riffle, J., *J. Magn. Magn. Mater.* **2005,** *293*, 224-239.

(15) Berensmeier, S., *Appl. Microbiol. Biotechnol.* **2006,** *73*, 495-504.

(16) Borlido, L.; Azevedo, A.; Roque, A.; Aires-Barros, M., *Biotechnol. Adv.* **2013,** *31*, 1374-1385.

(17) Prestvik, W. S.; Berge, A.; Mørk, P. C.; Stenstad, P. M.; Ugelstad, J., Springer: 1997, pp 11-35.

(18) Senger, B.; Voegel, J.-C.; Schaaf, P., *Colloids Surf., A* **2000,** *165*, 255-285.

(19) Talbot, J.; Ricci, S., *Phys. Rev. Lett.* **1992,** *68*, 958.

(20) De Palma, R.; Reekmans, G.; Laureyn, W.; Borghs, G.; Maes, G., *Anal. Chem.* **2007,** *79*, 7540-7548.

(21) Lu, A. H.; Salabas, E. e. L.; Schüth, F., *Angew. Chem. Int. Ed.* **2007,** *46*, 1222-1244.

(22) De Palma, R.; Liu, C.; Barbagini, F.; Reekmans, G.; Bonroy, K.; Laureyn, W.; Borghs, G.; Maes, G., *J. Phys. Chem. C* **2007,** *111*, 12227-12235.

(23) Park, J.; Porter, M. D.; Granger, M. C., *Langmuir* **2015,** *31*, 3537-3545.

(24) Zeltner, M.; Grass, R. N.; Schaetz, A.; Bubenhofer, S. B.; Luechinger, N. A.; Stark, W. J., *J. Mater. Chem.* **2012,** *22*, 12064-12071.

(25) Melikhov, Y.; Lee, S.; Jiles, D. C.; Schmidt, D.; Porter, M. D.; Shinar, R., *J. Appl. Phys.* **2003,** *93*, 8438-8440.

(26) Millen, R. L.; Kawaguchi, T.; Granger, M. C.; Porter, M. D.; Tondra, M., *Anal. Chem.* **2005,** *77*, 6581-6587.

(27) Millen, R. L.; Nordling, J.; Bullen, H. A.; Porter, M. D.; Tondra, M.; Granger, M. C., *Anal. Chem.* **2008,** *80*, 7940-7946.

(28) Nordling, J.; Millen, R. L.; Bullen, H. A.; Porter, M. D.; Tondra, M.; Granger, M. C., *Anal. Chem.* **2008,** *80*, 7930-7939.

(29) Tondra, M.; Porter, M.; Lipert, R. J., *J. Vac. Sci. Technol., A* **2000,** *18*, 1125-1129.

(30) Young, C. C.; Blackley, B. W.; Porter, M. D.; Granger, M. C., *Anal. Chem.* **2016,** *88*, 2015-2020.

(31) Bai, F.; Wang, D.; Huo, Z.; Chen, W.; Liu, L.; Liang, X.; Chen, C.; Wang, X.; Peng, Q.; Li, Y., *Angew. Chem. Int. Ed.* **2007,** *46*, 6650-6653.

(32) Bigall, N. C.; Wilhelm, C.; Beoutis, M.-L.; García-Hernandez, M.; Khan, A. A.; Giannini, C.; Sánchez-Ferrer, A.; Mezzenga, R.; Materia, M. E.; Garcia, M. A., *Chem. Mater.* **2013,** *25*, 1055-1062.

(33) Chen, O.; Riedemann, L.; Etoc, F.; Herrmann, H.; Coppey, M.; Barch, M.; Farrar, C. T.; Zhao, J.; Bruns, O. T.; Wei, H., *Nat. Commun.* **2014,** *5:5093*, 1-8.

(34) Chen, O.; Tan, R.; Zhu, H.; Cao, C., *Nanoscale* **2016,** *8*, 9944-9961.

(35) Guo, J.; Yang, W.; Wang, C., *Adv. Mater.* **2013,** *25*, 5196-5214.

(36) Lu, Z.; Yin, Y., *Chem. Soc. Rev.* **2012,** *41*, 6874-6887.

(37) Zhuang, J.; Wu, H.; Yang, Y.; Cao, Y. C., *Angew. Chem. Int. Ed.* **2008,** *47*, 2208-2212.

(38) Ge, J.; Hu, Y.; Biasini, M.; Beyermann, W. P.; Yin, Y., *Angew. Chem. Int. Ed.* **2007,** *46*, 4342-4345.

(39) Liu, J.; Zhang, Y.; Nan, Z., *Mater. Res. Bull.* **2014,** *60*, 270-278.

(40) Wang, T.; Wang, X.; LaMontagne, D.; Wang, Z.; Wang, Z.; Cao, Y. C., *J. Am. Chem. Soc.* **2012,** *134*, 18225-18228.

(41) Chen, S.; Zhang, J.; Song, S.; Feng, R.; Ju, Y.; Xiong, C.; Dong, L., *Langmuir* **2016,** *32*, 611-618.

(42) Ge, R.; Li, X.; Lin, M.; Wang, D.; Li, S.; Liu, S.; Tang, Q.; Liu, Y.; Jiang, J.; Liu, L., *ACS Appl. Mater. Interfaces* **2016,** *8*, 22942-22952.

(43) Wang, L.; Luo, J.; Shan, S.; Crew, E.; Yin, J.; Zhong, C.-J.; Wallek, B.; Wong, S. S., *Anal. Chem.* **2011,** *83*, 8688-8695.

(44) Wang, L.; Wang, X.; Luo, J.; Wanjala, B. N.; Wang, C.; Chernova, N. A.; Engelhard, M. H.; Liu, Y.; Bae, I.-T.; Zhong, C.-J., *J. Am. Chem. Soc.* **2010,** *132*, 17686-17689.

(45) Jang, J. t.; Nah, H.; Lee, J. H.; Moon, S. H.; Kim, M. G.; Cheon, J., *Angew. Chem.* **2009,** *121*, 1260-1264.

(46) Beji, Z.; Hanini, A.; Smiri, L.; Gavard, J.; Kacem, K.; Villain, F.; Grenéche, J.-M.; Chau, F.; Ammar, S., *Chem. Mater.* **2010,** *22*, 5420-5429.

(47) Yang, Y.; Liu, X.; Yang, Y.; Xiao, W.; Li, Z.; Xue, D.; Li, F.; Ding, J., *J. Mater. Chem. C* **2013,** *1*, 2875-2885.

(48) Yao, C.; Zeng, Q.; Goya, G.; Torres, T.; Liu, J.; Wu, H.; Ge, M.; Zeng, Y.; Wang, Y.; Jiang, J., *J. Phys. Chem. C* **2007,** *111*, 12274-12278.

(49) Xing, R.; Wang, X.; Zhang, C.; Wang, J.; Zhang, Y.; Song, Y.; Guo, Z., *J. Mater. Chem.* **2011,** *21*, 11142-11149.

(50) Mulvaney, S.; Myers, K.; Sheehan, P.; Whitman, L., *Biosens. Bioelectron.* **2009,** *24*, 1109-1115.

(51) Borges, J.; Mano, J. F., *Chem. Rev.* **2014,** *114*, 8883-8942.

(52) Cornell, R. M.; Schwertmann, U., John Wiley & Sons: 2003.

(53) Workman Jr, J., Elsevier: 2000.

(54) Dong, J.; Ozaki, Y.; Nakashima, K., *Macromolecules* **1997,** *30*, 1111-1117.

(55) Bayer, E. A.; Wilchek, M., *Methods Enzymol.* **1989,** *184*, 49-51.

(56) Cui, Y.; Wei, Q.; Park, H.; Lieber, C. M., *Science* **2001,** *293*, 1289-1292.

(57) Wayment, J. R.; Harris, J. M., *Anal. Chem.* **2008,** *81*, 336-342.

(58) Moore, C.; Monton, H.; O'Kennedy, R.; Williams, D.; Nogues, C.; Crean, C.; Gubala, V., *J. Mater. Chem. B* **2015,** *3*, 2043-2055.

(59) Gijs, M. A., *Microfluid. Nanofluid.* **2004,** *1*, 22-40.

(60) Leckband, D.; Schmitt, F.-J.; Israelachvili, J.; Knoll, W., *Biochemistry* **1994,** *33*, 4611-4624.

(61) Neish, C. S.; Martin, I. L.; Henderson, R. M.; Edwardson, J. M., *Br. J. Pharmacol* **2002,** *135*, 1943-1950.

(62) Fonnum, G.; Johansson, C.; Molteberg, A.; Mørup, S.; Aksnes, E., *J. Magn. Magn. Mater.* **2005,** *293*, 41-47.

(63) Grass, R. N.; Athanassiou, E. K.; Stark, W. J., *Angew. Chem. Int. Ed.* **2007,** *46*, 4909-4912.

(64) Grass, R. N.; Stark, W. J., *J. Mater. Chem.* **2006,** *16*, 1825-1830.

(65) Herrmann, I. K.; Grass, R. N.; Stark, W. J., *Nanomedicine* **2009,** *4*, 787-798.

(66) Chaubey, G. S.; Barcena, C.; Poudyal, N.; Rong, C.; Gao, J.; Sun, S.; Liu, J. P., *J. Am. Chem. Soc.* **2007,** *129*, 7214-7215.

(67) De Palma, R.; Reekmans, G.; Liu, C.; Wirix-Speetjens, R.; Laureyn, W.; Nilsson, O.; Lagae, L., *Anal. Chem.* **2007,** *79*, 8669-8677.

CHAPTER 5

DEVELOPMENT OF GMR-BASED IMMUNOASSAYS FOR POTENTIAL PANCREATIC CANCER MARKERS: TOWARDS THE SIMULTANEOUS DETECTION OF MULTIPLE BIOMARKERS

5.1 Introduction

Despite the low prevalence (3.1%) of pancreatic ductal adenocarcinoma (PDAC) in new cancer diagnosis, PDAC has a high mortality rate (*i.e.*, 5-year survival rate of 5-8%), which makes it the fourth leading cause of cancer-related deaths for both men and women in the U.S.[1-4] Moreover, and in spite of the significant advances in medical care (*i.e.*, patient selection, surgical technique, and perioperative care), tumor resection is still the best curative option for PDAC. Effective resection requires the early stage detection of PDAC, which is linked to the likelihood of a more positive patient outcome.[2] It has been shown, for example, that patients diagnosed at stage 1 have a longer survival than those diagnosed in stages 2-4.[5]

Early diagnosis of PDAC, nonetheless, remains problematic because of several factors, including: (1) the asymptomatic development of the disease; (2) the lack of one or more markers with high diagnostic accuracy; and (3) the variation in markers expressed in

PDAC patients. At present, carbohydrate antigen 19-9 (CA 19-9) is the only marker recommended by the National Comprehensive Cancer Network (NCCN) with respect to the clinical diagnosis of PDAC, and its utility is limited to use as a recurrence marker.[4] Complications of diagnosis of PDAC using CA 19-9 arise because: (1) CA 19-9 is detected in only ~25% of PDAC patients[6]; (2) the level of CA 19-9 can be elevated by inflammatory processes such as pancreatitis[2]; and (3) ~10% of the healthy population in the U.S. are classified as nonsecretors and do not produce CA 19-9.[7-9] Indeed, studies have shown that the utility of CA 19-9 in screening asymptomatic patients is of little value because the probability that subjects with a positive screening test truly have PDAC (*i.e.*, positive predictive value) is less than 1%.[10-11] Thus, the low specificity of CA 19-9 for PDAC can lead to high numbers of false-positive results which, subsequently, result in further investigation and an increase in medical expenses.

It has been proposed that an appropriate panel of biomarkers for PDAC may increase sensitivity and specificity and, consequently, improve the early stage diagnosis of PDAC.[12-13] There are, nonetheless, a number of obstacles to address when attempting to develop a panel to screen asymptomatic PDAC patients, including the lack of a validated set of markers that can be used in such a panel. However, recent reports have identified several potential biomarkers that can successfully discriminate between PDAC and controls.[14-21] Carcinoembryonic antigen-related cell adhesion molecule 1 (CEACAM-1) and osteopontin (OPN) showed an improvement in diagnostic accuracy when compared with CA 19-9 only.[20-21] However, CEACAM-1 and OPN are unable to discriminate PDAC from pancreatitis. Matrix metallopeptidase 7 (MMP-7) is another potential marker that has successfully distinguished patients with PDAC against patients with chronic pancreatitis,

but no improvement in diagnostic accuracy was shown over CA 19-9 alone.[19] Tissue inhibitor of metallopeptidase 1 (TIMP-1) is a secreted protein upregulated in PDAC tumors.[22-23] These results suggest that the levels of OPN, CEACAM-1, TIMP-1, and MMP-7 may find utility in PDAC diagnosis. Again, while no single biomarker has been shown to accurately predict the presence of PDAC, screening multiple biomarkers in a panel may improve diagnostic accuracy.[13, 24] A study examining a panel of CA 19-9, TIMP-1, and carcinoembryonic antigen exhibited improved diagnostic accuracy over CA 19-9 alone.[24] It has been also reported that any panel of 7 biomarkers, among 40 non-correlated biomarkers characterized individually with thresholds of 32% sensitivity and 95% specificity, would achieve a sensitivity and specificity of 99% for the diagnosis of PDAC.[12]

As has been postulated, the ability to realize early diagnosis of PDAC may be made more probable by a multiplexed test that could readily be performed at regular intervals (*i.e.*, annual checkups) for screening every individual. The most well studied *in-vitro* immunoassays is the enzyme-linked immunosorbent assay (ELISA), which is a plate-based assay routinely used in clinical laboratories. However, screening a panel of PDAC markers using ELISA requires a large sample volume, which leads to increase in cost. Among many potential *in-vitro* diagnostic platforms for the early diagnosis of cancer, magnetoresistive (MR)-based detection combined with protein immunoassays is a promising technique. The high sensitivity of MR sensors is based on a phenomenon called giant magnetoresistance (GMR), which describes the large resistance change that occurs upon exposure to a magnetic field.[25] This high sensitivity of GMR sensors has been applied to the bioanalytical arena for the development of new diagnostic platforms over the past few years, with the first report in 1998 by a group at the Naval Research Laboratory.[26] Since then, many

research groups reported the development of GMR sensors with high sensitivity.[27-31] In addition, the GMR-based diagnostic platform is theoretically capable of simultaneous detection of a large number of analytes with small volumes of sample due to the advantage of a photolithographic fabrication technique.[32-33] Our group has developed a GMR-based detection system that separates the GMR sensor from the immunoassay substrate in a manner that imitates the working mechanism of hard disk drive readers.[34-36] Our approach, while taking advantage of chip-scale immunoassays with a small sample volume, also allows for reuse of the sensor, which potentially reduces costs.

Herein, we introduce the development of immunoassays for the detection of potential PDAC markers based on GMR sensor readout with in-house magnetic labels. We have shown that colloidally assembled magnetic beads are superparamagnetic, have a high magnetic moment, and can be employed as magnetic labels for our GMR sensor. First, immunoassays for four potential PDAC markers (*i.e.*, OPN, CEACAM-1, TIMP-1, and MMP-7) were developed in buffer. Furthermore, the cross-reactivity between these markers was also tested in buffer. To emulate GMR-based detection for patient diagnosis of PDAC, immunoassays and cross reactivity studies of OPN and MMP-7 spiked in human serum were also investigated. We believe that the findings described in this paper show a promise toward the development of a GMR-based detection platform for the early diagnosis of cancer.

5.2 Experimental Section

5.2.1 Materials

Iron acetylacetonate ($Fe(acac)_3$), zinc acetylacetonate ($Zn(acac)_2$), oleylamine, ethylene glycol, benzyl ether, and chloroform were purchased from Acros Organics (USA). Oleic acid and poly(acrylic acid) (PAA, MW ~15 kDa) were acquired from Alfa Aesar (USA) and Fluka (Japan), respectively. Poly(vinylpyrrolidone) (PVP, MW ~50 kDa), poly(vinylalcohol) (PVA, MW 30─70 kDa), bovine serum albumin (BSA), sodium phosphate (monobasic and dibasic), 2-(N-morpholino)ethanesulfonic acid (MES), and dodecyltrimethylammonium bromide (DTAB) were obtained from Sigma Aldrich (USA). Streptavidin, 1-ethyl-3-(3-dimethylaminopropyl)carbodiimide (EDC), N-hydroxysulfosuccinimide (sulfo-NHS), dithiobis(succinimidyl propionate) (DSP), and modified Dulbecco's phosphate-buffered saline packages (10 mM PBS) were purchased from Fisher Scientific (USA). All antibodies and markers were acquired from R&D systems, Inc. (USA): monoclonal human osteopontin (OPN) antibody (catalog no. MAB1433), recombinant human OPN protein (catalog no.1433-OP), biotinylated polyclonal human OPN antibody (catalog no. BAF1433), monoclonal human (α-CEACAM-1/CD66a) antibody (catalog no. MAB22441), recombinant human CEACAM-1 (catalog no. 2244-CM-050), biotinylated polyclonal human CEACAM-1 antibody (catalog no. BAF2244), monoclonal human TIMP metallopeptidase inhibitor 1 (TIMP-1) antibody (catalog no. MAB970), recombinant human TIMP-1 (catalog no. 907-TM), biotinylated polyclonal human TIMP-1 antibody (catalog no. BAF970), Duoset human metallopeptidase 7 (MMP-7) antibody, Duoset MMP-7 standard, and biotinylated Duoset MMP-7 antibody. Phosphate-buffered saline/casein block was acquired from Surmodics

(USA). Pooled human serum (HE1532) was obtained from Randox (UK).

5.2.2. Synthesis of Zinc Ferrite Nanoparticles and Zinc Ferrite Magnetic Beads

Zinc ferrite nanoparticles (ZFNPs) were synthesized using a slight modification to a published procedure.[37] For ZFNPs, 1.3 mmol $Fe(acac)_3$, 0.3 mmol $Zn(acac)_2$, 2.1 mL of neat oleic acid, and 2.1 mL of oleylamine were added to 20 mL of benzyl ether and refluxed at 290 ˚C for 1 h under an inert atmosphere. The as-synthesized ZFNPs were rinsed with a mixture (3:1 v/v) of acetone and hexane by centrifugation and dried under vacuum. The dried ZFNPs were resuspended in 5.0 mL of chloroform at a concentration of ~20 mg/mL.

The colloidally assembled zinc ferrite magnetic beads (ZFMBs) were prepared by following a recent procedure.[38-39] Briefly, 1.0 mL of ZFNPs in chloroform was added to 1.0 mL of DTAB solution (20 mg/mL) in a 5 mL centrifuge tube. This mixture was thoroughly vortexed for 5 min and the emulsion was transferred to a round-bottom flask. Next, chloroform was removed by placing the flask in a 40 ˚C water bath and purging with nitrogen for 30 min. The DTAB-stabilized particles were then injected in 5.0 mL of PVP solution (0.55 g PVP dissolved in 5.0 mL ethylene glycol), magnetically stirred for 10 min, heated to 80 °C, and refluxed for 6 h under nitrogen. The PVP-coated ZFMBs were centrifuged at 5500*g* for 30 min and the pellet was then resuspended in 10 mL of ethanol. This rinsing procedure was repeated twice and the rinsed PVP-coated ZFMBs were resuspended in 10 mL of ethanol.

5.2.3 Magnetic Label Preparation

In order to conjugate molecular recognition moieties on the ZFMBs, the as-synthesized ZFMBs were coated with a layer of PAA. First, 0.5 mL of ZFMBs in ethanol was mixed with 1.0 mL of aqueous PAA solution (10 mg/mL). The mixture was sonicated for 10 min and mixed over 12 h. The PAA-coated ZFMBs were rinsed three times by repeating centrifugation and resuspension in 1.0 mL deionized water (DI H_2O).

Streptavidin conjugation was carried out using carbodiimide chemistry (*i.e.*, EDC/sulfo-NHS). First, 1.0 mL of PAA-coated ZFMBs was centrifuged at 5200*g* for 3 min and resuspended in 1.0 mL of 5 mM MES buffer (pH 6.5). Then, 50 µL of EDC (20 mg/mL) and 100 µL of sulfo-NHS (10 mg/mL) in 25 mM MES buffer (pH 6.5) were added to the particle suspension. After 30 min, the particles were collected at the bottom of the centrifuge tube using a 1 cm^3 neodymium magnet and the supernatant was discarded. The collected particles were resuspended in 1.0 mL 5 mM MES, followed by the addition of 60 µL streptavidin (2.5 mg/mL in DI H_2O). This suspension was agitated for 2 h on an orbital mixer. The unbound streptavidin was removed by centrifugation (2400*g* for 2 min). The streptavidin-conjugated ZFMBs were suspended in 1.0 mL of 10 mM phosphate buffer (pH 7.4), which contained 70 mM NaCl and 0.2% (w/v) PVA to serve as a blocking agent.

5.2.4 Characterization

5.2.4.1 Scanning electron microscopy (SEM). SEM images of ZFMBs was obtained using SEM S4800 (Hitachi, Japan). A droplet of particle sample was drop casted on a silicon chip for imaging.

5.2.4.2 Vibrating sample magnetometry (VSM). Hysteresis curves were acquired at room temperature using VSM EZ7 (Microsense, MA).

5.2.4.3 Dynamic light scattering (DLS). A Zetasizer Nano (Malvern, United Kingdom) was used to measure a hydrodynamic size of ZFMBs. Three measurements per sample (n=3) were taken to determine an average value of hydrodynamic size.

5.2.4.4 Optical microscopy. An optical microscope (BX50WI, Olympus, Japan) with 12.8 megapixel CCD camera (DP72) was used to capture assay substrates.

5.2.5 Assay Substrate Configuration and Fabrication

The assay substrate was fabricated using photolithography/lift-off techniques. Briefly, the assay substrates were created by evaporating nickel (10-nm thick) and gold (200-nm thick) addresses on Pyrex wafers (2-mm thick) after a layer of chromium (10-nm thick) was deposited as an adhesion layer. A titanium layer (15-nm thick) was deposited on the top of the nickel addresses to prevent oxidation. The wafer was then diced into individual 0.3 × 2.0 cm rectangular sticks (the substrate). The layout of the assay substrate is shown in Figure 5.1A and consists of twelve gold addresses interspersed between thirteen nickel addresses. The nickel and gold addresses are 200 × 200 μm in size. Each gold address is spaced (edge to edge) 500 μm from its neighboring nickel addresses. The nickel addresses are used as internal reference signals. The gold addresses are used for the construction of the capture addresses.

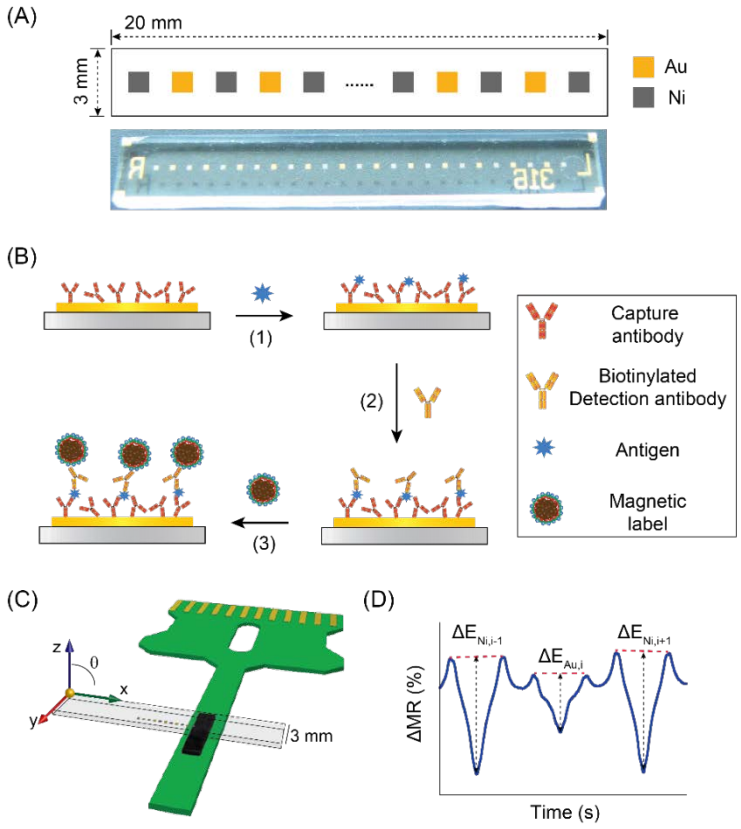

Figure 5.1 Schematic illustration of assay substrate layout, assay procedure, and MR analysis. (A) Schematic design and actual photograph of assay substrate. (B) Assay procedure starting with capture antibody-modified assay substrate, followed by (1) antigen incubation, (2) detection antibody incubation, and (3) labeling step. (C) Depiction of assay substrate scanning. (D) MR signal analysis.

5.2.6 Assay Procedure

5.2.6.1 Immobilization of capture antibody. An overview of the assay procedure is given in Figure 5.1B. Any residual photoresist from the fabrication process on the assay substrate is removed by an oxygen plasma (Oxford 80 RIE). The substrates were cleaned at a power of 150 W for 6 min under O_2 gas at 50 sccm. The substrates were then sonicated in acetone for 10 min, rinsed with methanol, and dried with nitrogen. The Au addresses were then functionalized by immersion in an ethanolic 1 mM DSP solution for 1 h. After DSP modification, the substrates were rinsed with ethanol and dried with nitrogen. Next, a

40 µL droplet of monoclonal human antibody (20 µg/mL) in 10 mM phosphate-buffered saline (PBS, pH 7.4) was applied to the top of each substrate, which was then stored in a humidified chamber. After 2 h, each substrate was transferred into a well of a 12-well plate and rinsed three times using 10 mM PBS. Then, the substrates were blocked by incubation with 1.0 mL of 20% (v/v) casein blocking solution in PBS for 1 h in a humidified chamber to combat nonspecific adsorption.

5.2.6.2 Antigen capture and labeling steps. A dilution series (0.5 to 50 ng/mL) of each marker was prepared by spiking in 10 mM PBS containing 1.0% BSA. For serum assays, each marker was first spiked in neat serum, and then diluted using neat serum. Note that the concentration range for rh-MMP-7 is 0 to 10 ng/mL in both buffer and serum. For the preparation of calibration standards for rh-MMP-7 in diluted (1:4 v/v pooled human serum/PBS) serum, rh-MMP-7 antigen was first spiked in neat serum, and then diluted with PBS buffer in 1:4 v/v pooled human serum/PBS to obtain the desired concentration. These solutions were applied to the substrates in separate wells, incubated for 2 h in a humidified chamber, and rinsed three times with 10 mM PBS. In the next step, 1 mL of biotinylated polyclonal detection antibody (0.5 µg/mL in 10 mM PBS containing 1.0% BSA) was added to each well, incubated for 2 h in a humidified chamber, and rinsed with 10 mM PBS four times.

For labeling, a droplet (~40 µL) of a magnetic label suspension was pipetted onto each coupon and incubated for 1 h in a humidified chamber. The average concentration of streptavidinated ZFMBs was estimated to be 7×10^{10} beads/mL by nanoparticle tracking analysis. Unbound labels were subsequently removed by rinsing four times with 5 mM borate buffer with 150 mM NaCl and finally washing once with DI H_2O.

5.2.7 Cross Reactivity Studies

For cross reactivity studies of the four markers (rh-OPN, rh-CEACAM-1, rh-TIMP-1, and rh-MMP-7) in buffer, each assay substrate was divided into two sections by placing a thin strip of parafilm in the middle of the substrate; note that each section in a substrate has five gold addresses. The two sections of the substrate were then each modified with different capture antibodies by applying a 20 µL droplet of monoclonal human antibody (20 µg/mL) in 10 mM PBS (pH 7.4). Therefore, testing of each antigen required two assay substrates to accommodate the four sections modified with four capture antibodies of OPN, CEACAM-1, TIMP-1, and MMP-7. Subsequently, the two assay substrates were placed in a well of a 12-well plate and blocked with 1.0 mL of 20% (v/v) casein blocking solution in PBS for 1 h. Next, the two substrates were exposed to either a single antigen solution at 10 ng/mL or a mixed antigen solution containing 10 ng/mL of each marker in PBS with 1% BSA, incubated for 2 h, and rinsed with 10 mM PBS three times. In the next step, 1 mL of a mixed detection antibody solution containing four detection antibodies (each at 0.5 µg/mL in 10 mM PBS with 1.0% BSA) was added to each well, incubated for 2 h, and rinsed with 10 mM PBS four times. The labeling step was followed in the same manner described above. The cross reactivity studies in serum were pursued in a similar way to those in buffer, except with the preparation of antigen solutions in diluted serum (1:4 v/v pooled human serum:PBS).

5.2.8 MR Data Analysis

A completed assay substrate was placed above our MR sensor as shown in Figure 5.1C. The separation distance (*d*) between the substrate and MR sensor was set at 10 ± 1.0

μm. To measure MR signals, the MR sensor was moved in the direction of *x* as shown in Figure 5.1C. The translational scanning speed of our MR sensor along the addresses on the assay substrate was 31.1 ± 0.1 μm/sec under a magnetic field of 100 Oe.

In order to quantitatively measure MR responses, we incorporate nickel addresses. The MR signals from nickel addresses not only account for any changes in *d*, but also enable normalization of the MR signal from each gold address. As described in Figure 5.1D, the normalized response ($\boldsymbol{MR}_{norm,i}$) from the *i*-th gold address with respect to the two adjacent Ni addresses can be written as follows,

$$\boldsymbol{MR}_{norm,i} = \frac{2\Delta E_{Au,i}}{\Delta E_{Ni,i-1}+\Delta E_{Ni,i+1}} \tag{5.1}$$

where ΔE_{Au} and ΔE_{Ni} represent the MR responses of gold and nickel addresses, respectively.

The MR response for each antigen concentration was obtained by averaging the MR responses from twelve replicates (gold addresses) in one substrate. Similarly, the standard deviation for each MR data point was determined from the twelve gold addresses on each substrate.

5.3 Results and Discussion

5.3.1 Magnetic Labels

Before use as immunoassay labels, the colloidally assembled magnetic beads (ZFMBs) were characterized using SEM, VSM, and DLS. Figure 5.2A shows a SEM image

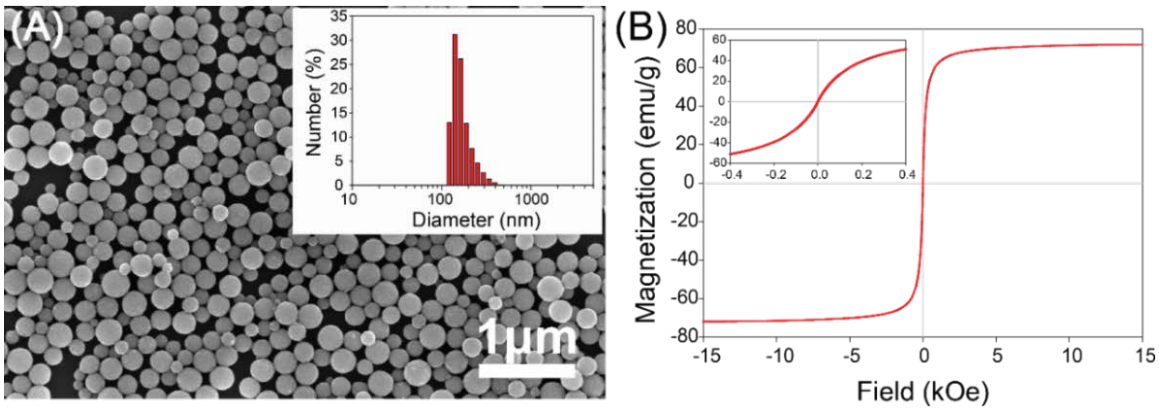

Figure 5.2 Characterization of as-synthesized ZFMBs. (A) SEM with the inset of hydrodynamic size of the as-synthesized ZFMBs. (B) Hysteresis curve at room temperature.

of the as-synthesized spherical ZFMBs. Hydrodynamic diameter of the ZFMBs in the inset of Figure 5.2A, obtained by DLS, is 170 ± 56 nm, which agrees with the diameter of the ZFMBs determined from the SEM image (169 ± 36 nm, n=125). The hysteresis curve of the ZFMBs in Figure 5.2B indicates that the as-synthesized ZFMBs exhibit a remanent magnetization near zero at room temperature (*i.e.*, superparamagnetism). Such a low level of residual magnetism ensures colloidal stability of the ZFMBs in suspension when prepared as labels. To use the ZFMBs as magnetic labels, ZFMBs were further coated with a PAA layer and, subsequently, conjugated with streptavidin via carbodiimide linking chemistry.

The specific targeting ability of the streptavidinated ZFMBs for captured biotin molecules is shown in Figure 5.3, which contains images of the magnetic label-modified gold addresses after exposure to PBS and to a solution with rh-OPN at 10 ng/mL. Any binding on the gold address (Figure 5.3A) for the blank buffer sample is due to the nonspecific adsorption of ZFMB labels. The estimated surface coverage of the ZFMB labels bound on gold addresses for the blank samples is less than 5% of the total surface

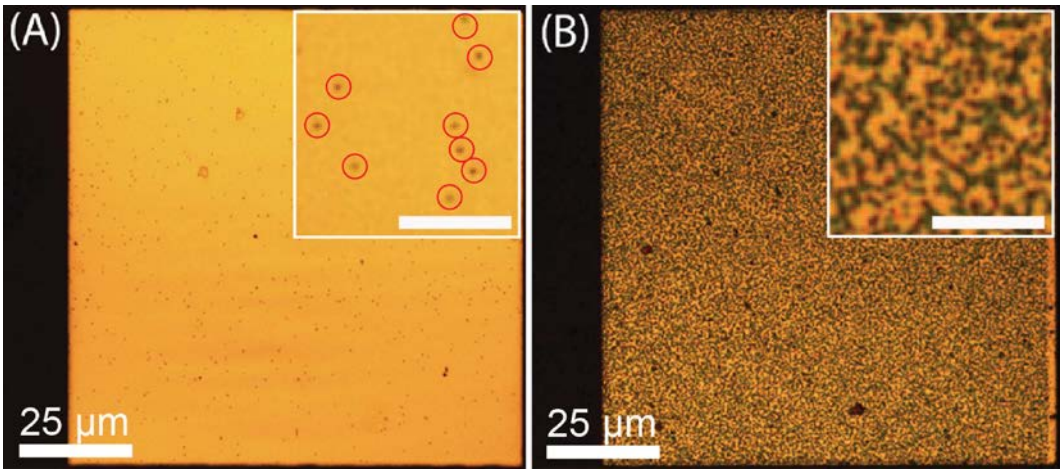

Figure 5.3 Representative optical microscope images of gold addresses bound with ZFMB labels from OPN assays exposed to (A) 0 ng/mL and (B) 10 ng/mL of rh-OPN. Note that some nonspecific adsorption of ZFMB labels (red-circled) in (A) was observed in the blank. The scale bar for the insets is 10 µm.

area of the address. At 10 ng/mL of rh-OPN, the increase in the amount of ZFMBs on the gold surface (Figure 5.3B) of ~50% of the total surface area reflects the more specific interaction between the captured antigens and recognition elements on magnetic labels.

5.3.2 Detection of rh-OPN, rh-CEACAM-1, rh-TIMP-1, and rh-MMP-7 Spiked in PBS

Immunoassays for the detection of four potential PDAC markers (rh-OPN, rh-CEACAM-1, rh-TIMP-1, and rh-MMP-7) were first developed and tested in buffer. Each assay was run as a singleplex. The dose response curves for the four markers spiked in PBS with 1% BSA are presented in Figure 5.4 as plots of MR response as a function of each marker concentration. In general, MR signals increase with the concentration of each marker. The blanks (*i.e.*, 0 ng/mL) for each assay show a level of nonspecific binding (~3% in ΔMR). The limit of detection (LoD) for each assay is calculated from the signal from

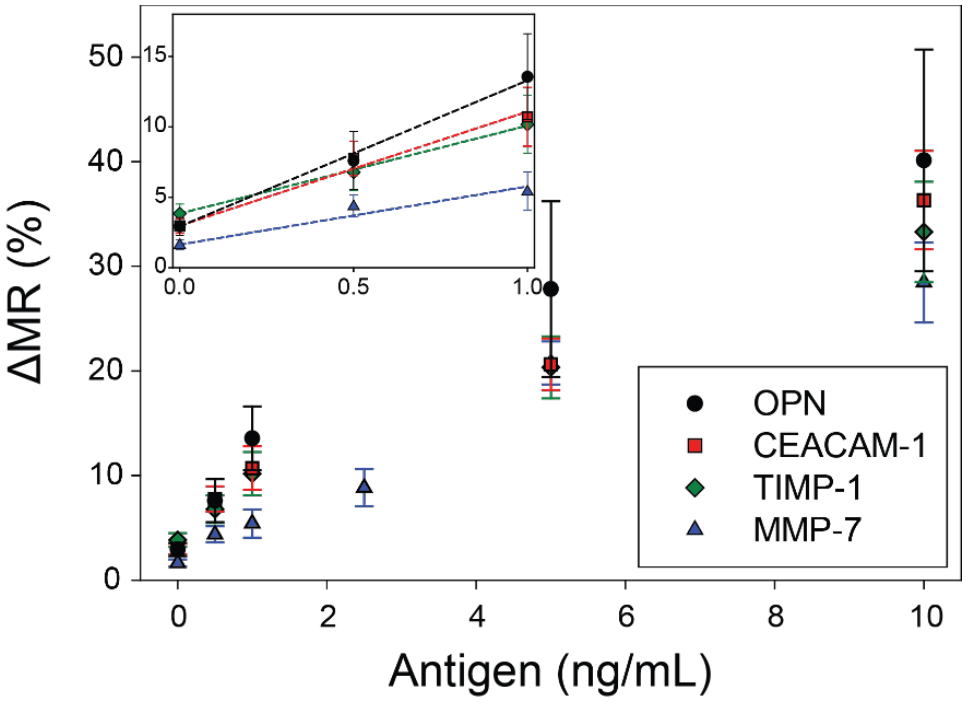

Figure 5.4 Representative dose response curves for four potential PDAC markers in PBS. All markers were spiked in and diluted with PBS containing 1% BSA. The immunoassay for each marker was performed singly. The resulting MR signals are the averages of MR responses from twelve gold addresses on each assay substrate.

the blank plus three times the standard deviation of the blank and the slope (*i.e.*, analytical sensitivity) from a least-squares linear fit of the responses up to 1 ng/mL. The LoDs for rh-OPN, rh-CEACAM-1, rh-TIMP-1, and rh-MMP-7 spiked in buffer are calculated to be 240, 190, 330, and 260 pg/mL (8, 5, 16, and 10 pM), respectively. These LoDs are lower than the clinically relevant cutoff levels in PDAC patients shown in Table 5.1 and, therefore, sufficient for use in a PDAC screening test.

Table 5.1 The cutoff levels of rh-OPN, rh-CEACAM-1, rh-TIMP-1, and rh-MMP-7 in PDAC patients. In general, the cutoff values correspond to the mean level for the control groups (*i.e.*, healthy control subjects and patients with chronic pancreatitis) plus two times the standard deviation of the mean level. Note that the mean levels of those markers in PDAC patients are higher than the cutoff values. All cutoff values were obtained using ELISA.

Marker	Method	Cutoff	Reference
rh-OPN	ELISA	25 ng/mL	19
rh-CEACAM-1	ELISA	4.8 ng/mL	20
rh-TIMP-1	ELISA	207 ng/mL	15
rh-MMP-7	ELISA	5.5 ng/mL	42

5.3.3 Cross Reactivity Studies for rh-OPN, rh-CEACAM-1, rh-TIMP-1, and rh-MMP-7 Spiked in PBS

Cross reactivity studies of the potential markers were performed both theoretically by Basic Local Alignment Search Tool (BLAST) analysis and experimentally by immunoassays in buffer. BLAST analysis is an algorithm for finding regions of similarity between biological sequences (*e.g.*, amino acid sequences of nucleotides or proteins),[41] and, thus, was used to examine the similarities in the amino acid sequences of the potential PDAC markers to theoretically determine potential cross reactivity. The information on amino acid sequences for BLAST analysis was obtained from the National Center for Biotechnology Information (NCBI) database by using gene ID numbers of the markers provided from the vendor. Presented in Figure 5.5 is an example of BLAST analysis of rh-OPN compared to rh-CEACAM-1, rh-TIMP-1, and rh-MMP-7. In Figure 5.5A, three blast hits of rh-OPN were found in rh-CEACAM-1 sequences (highlighted in yellow dashed box), but the alignment scores of the three hits are less than 40, indicating the similarities are not significant. None of the alignment scores of BLAST hits in Figures 5.5B and 5.5C

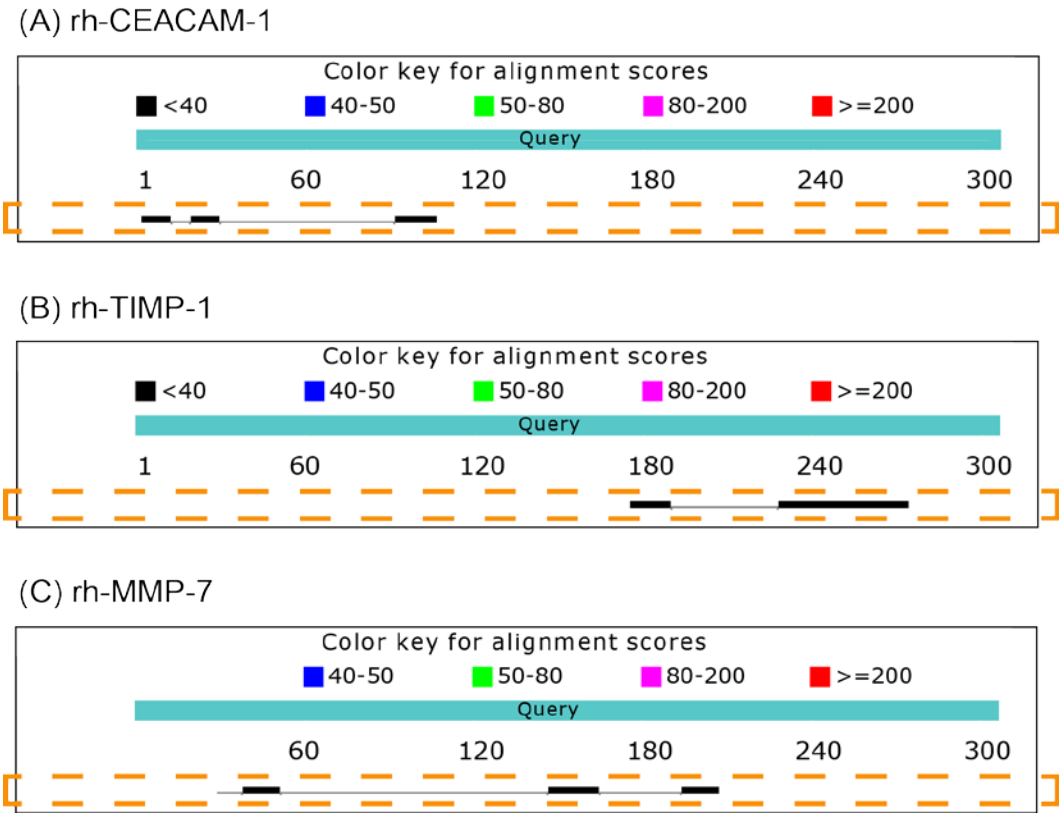

Figure 5.5 BLAST analysis of rh-OPN in comparison to (A) rh-CEACAM-1, (B) rh-TIMP-1, and (C) rh-MMP-7. A query sequence of rh-OPN was compared with subject sequences of rh-CEACAM-1, rh-TIMP-1, and rh-MMP-7.

are larger than 40. It should be noted that the alignment scores of possible combinations among the marker panel of rh-OPN, rh-CEACAM-1, rh-TIMP-1, and rh-MMP-7 had less than 40% similarity, which indicates that nonspecific binding of the markers to non-complimentary antibodies is unlikely.

Cross reactivity studies were also performed experimentally using immunoassays as depicted in Figure 5.6. A pair of two assay substrates had a total of four sections (each section containing a single antibody type) and was exposed to a sample containing either a single antigen or a mixed antigen solution that contained the four markers. Figure 5.7 shows the average MR responses from cross reactivity tests of the markers in buffer. The

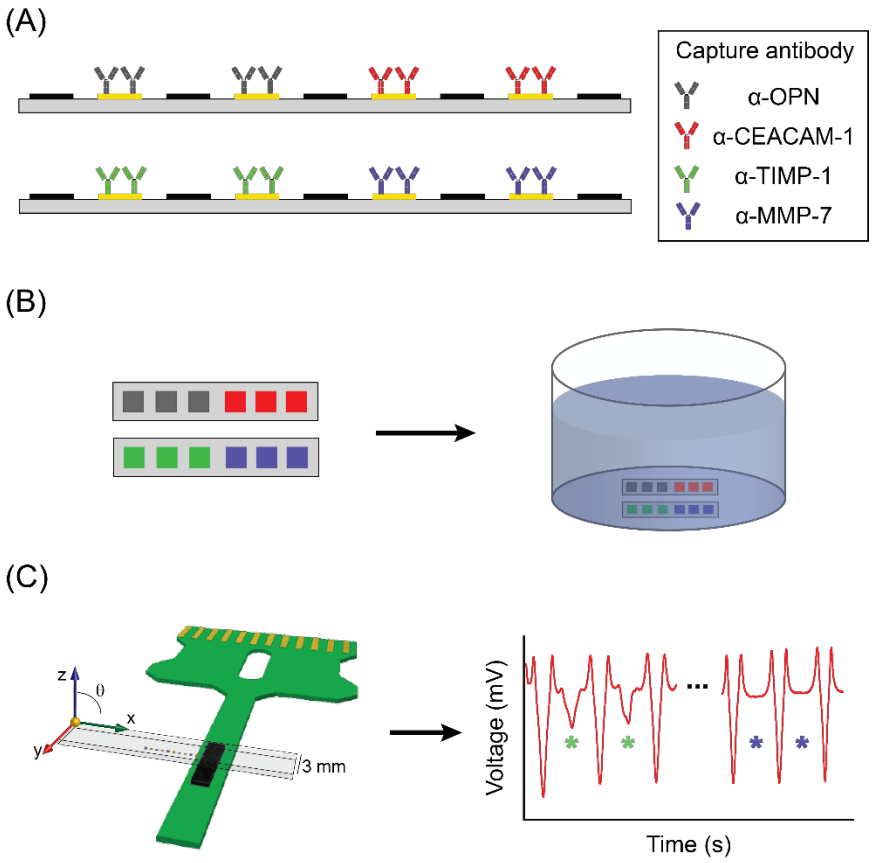

Figure 5.6 Schematic illustration of experimental cross reactivity study. (A) A pair of two assay substrates for cross reactivity study. Each substrate has two sections modified with two different capture antibodies. (B) Illustration of exposure of two substrates to a sample in a single well. (C) Description of assay substrate scanning and MR signal analysis. The signals labeled with asterisks represent MR responses from Au addresses modified with different capture antibodies.

results of these cross reactivity studies, shown in Figure 5.7, match that from the theoretical results predicted in the BLAST analysis with little to no cross reactivity among all four markers. As shown in the first set of columns of Figure 5.7, when a pair of two assay substrates was exposed to rh-OPN only, the gold addresses modified with the capture antibody for rh-OPN gave a positive MR response larger than 5%. Other sections with nonspecific antibodies for rh-OPN showed ~3% in ΔMR. For the other markers, the same patterns were observed with minimal cross reactivity (less than ~5% in ΔMR signal) with

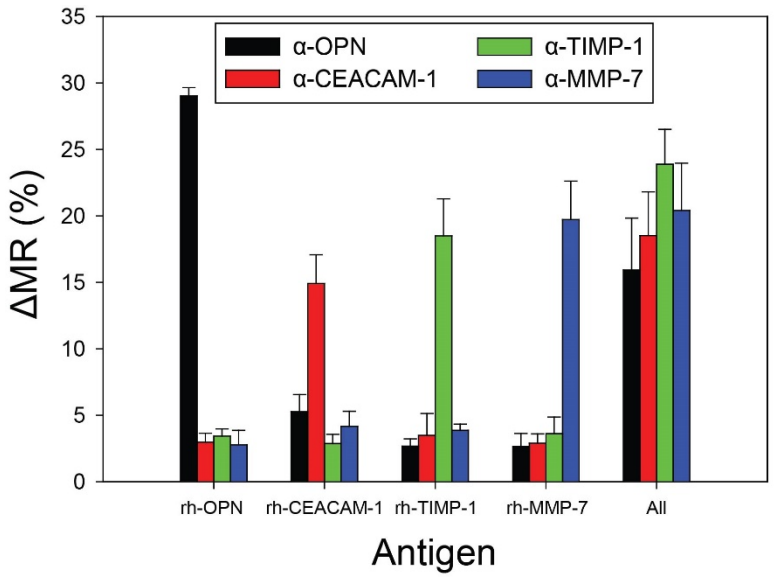

Figure 5.7 Cross reactivity studies of potential PDAC markers in PBS with 1% BSA. The marker concentration in all assays was 10 ng/mL. Note that, for all substrates, the detection antibody solution is the mixture of biotinylated polyclonal antibodies for all markers at 0.5 µg/mL. Error bars represent average of MR responses from five gold addresses.

nonspecific antibodies. When the mixed antigen solution (*i.e.*, containing four markers) was applied to the assay substrate, MR responses from all gold addresses were clearly observed, which indicates that the presence of multiple markers may not prevent each marker from binding to its respective capture antibody.

5.3.4 Detection of rh-OPN and rh-MMP-7 Spiked in Human Serum

To simulate patient diagnosis, immunoassays were performed with the four antigens (*i.e.*, rh-OPN, rh-CEACAM-1, rh-TIMP-1, and rh-MMP-7) spiked into neat human serum. Unfortunately, when rh-CEACAM-1 and rh-TIMP-1 are spiked in untreated human serum, the assays suffer from increased nonspecific adsorption of labels and low analytical sensitivity, as shown in Figure 5.8A. These interferences can result from a

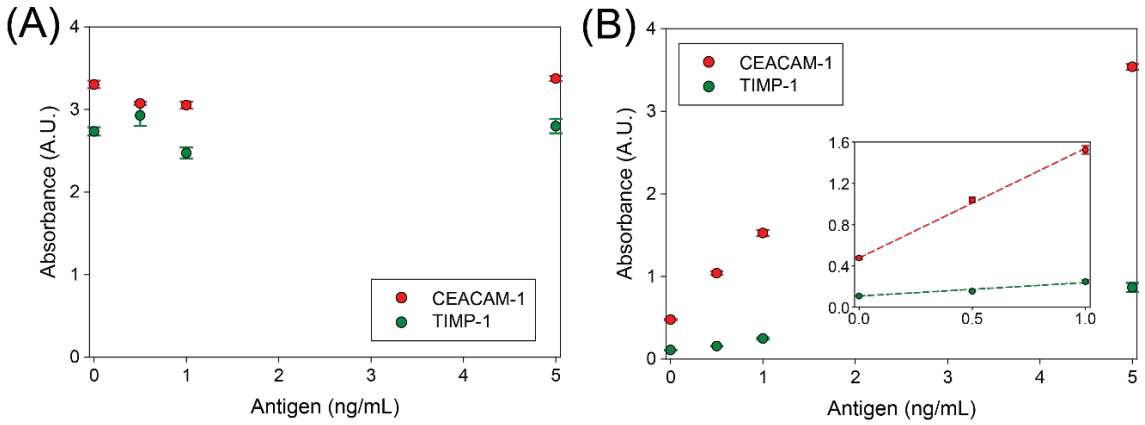

Figure 5.8 Dose response plots from ELISA for the detection of rh-CEACAM-1 and rh-TIMP-1 in (A) neat and (B) treated serum. The inset in (B) shows responses with a least-squares linear fit at concentrations less than 1.0 ng/mL of rh-CEACAM-1 and rh-TIMP-1.

number of different scenarios, including interactions with heterophilic antibodies, human anti-mouse antibody, and complexation of markers with serum constituents.[42-44] We suspect that the interference may arise from nonspecific interactions between endogenous heterophilic antibodies often found in human serum, and the capture and/or detection antibodies due to their poorly defined paratope regions.[43-44] Heterophilic antibodies, which usually form a bridging set of linkages between capture and detection antibodies in sandwich immunoassays, can lead to high signals for samples due to an increase in nonspecific adsorption. The situation can also result in a decrease in analytical sensitivity due to the competition between an antigen and heterophilic antibody for binding sites on the immobilized capture antibody.

To remove some of the proteins that may interfere with assay components, neat serum was treated with either a 100 or 50 kDa molecular-weight cutoff (MWCO) filter. The filtrate (*i.e.*, the serum fluid containing serum components with molecular weights lower than the cutoff value of MWCO filters) was subsequently used for antigen dilution:

rh-CEACAM-1 and rh-TIMP-1 were spiked in the filtrates collected by MWCO 100K and 50K, respectively. Dose response curves for rh-CEACAM-1 and rh-TIMP-1 in the neat and treated serum, obtained by ELISA, are shown in Figure 5.8. In neat serum (Figure 5.8A), both assays suffer from a high level of nonspecific adsorption in the blank and no appreciable signal difference as a function of antigen concentration was observed. These results indicate the likelihood that serum proteins, which have molecular weights larger than the MWCO cutoff values, are interfering with assay components in the rh-CEACAM-1 and rh-TIMP-1 assays. However, in the treated serum passed through the MWCO filters, dose response plots for rh-CEACAM-1 and rh-TIMP-1 were successfully obtained as shown in Figure 5.8B. It should be noted that, when rh-TIMP-1 spiked in the treated serum using MWCO 100K, the assay also suffered from poor analytical sensitivity due to the interference. This implies that rh-TIMP-1 may also interfere with serum components having a molecular weight between 50 and 100 kDa.

While rh-OPN showed little to no change in assay performance when moving into human serum, rh-MMP-7 assays in neat serum showed a slight increase in nonspecific binding in a blank. As a result, MMP-7 assays were carried out in diluted serum. Figure 5.9 shows the dose response plots of rh-OPN and rh-MMP-7 spiked in neat and diluted human serum (1:4 v/v pooled human serum:PBS), respectively. The LoDs of rh-OPN and rh-MMP-7, obtained from Figure 5.9, are 840 pg/mL (27 pM) and 500 pg/mL (18 pM), respectively. These LoDs are in the same order of magnitude with those obtained from samples spiked in PBS with 1% BSA, indicating that there is no significant complexation between assay components (*i.e.*, capture antibodies and markers) and serum constituents. Given that the assay for rh-MMP-7 was performed in diluted serum (1:4 v/v pooled human

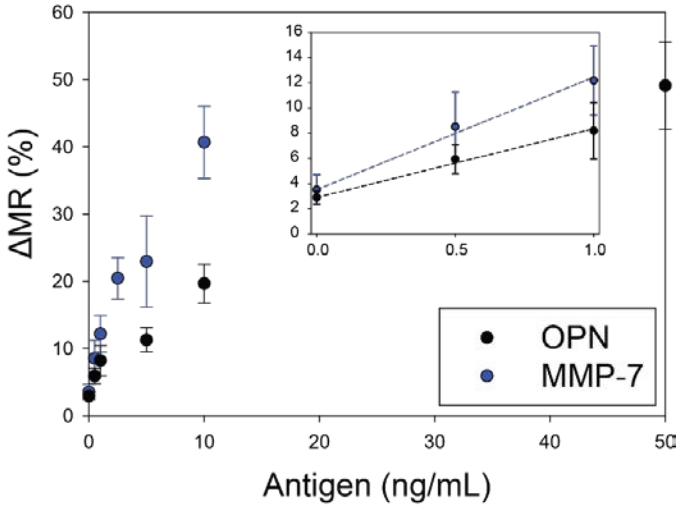

Figure 5.9 Dose response plots of rh-OPN and rh-MMP-7 spiked in neat and diluted serum (1:4 serum/PBS), respectively. The inset shows MR responses with a least-squares linear fit at concentrations less than 1.0 ng/mL of rh-OPN and rh-MMP-7. Error bars represent average of MR responses from twelve gold addresses.

serum : PBS), the relevant LoD of rh-MMP-7 in actual serum samples may increase to ~ 2 ng/mL. More importantly, the LoDs for rh-OPN and rh-MMP-7 in serum are below the cutoff levels found in PDAC patients (Table 5.1).

5.3.5 Cross Reactivity Studies of rh-OPN and rh-MMP-7 in Diluted Human Serum

Cross reactivity studies of rh-OPN and rh-MMP-7 in diluted human serum (1:4 v/v pooled human serum:PBS) were conducted in a fashion similar to those performed in buffer. Each marker was first spiked in neat serum and then diluted with PBS (1:4 v/v) to a concentration of 7.5 ng/mL. Figure 5.10 shows MR responses from duplexed assays of rh-OPN and rh-MMP-7 at 7.5 ng/mL in diluted human serum. When the assay substrate was exposed only to rh-OPN, a large MR response arises from the addresses modified with α-OPN in comparison to the small MR response (~ 3%) from the addresses modified with α-

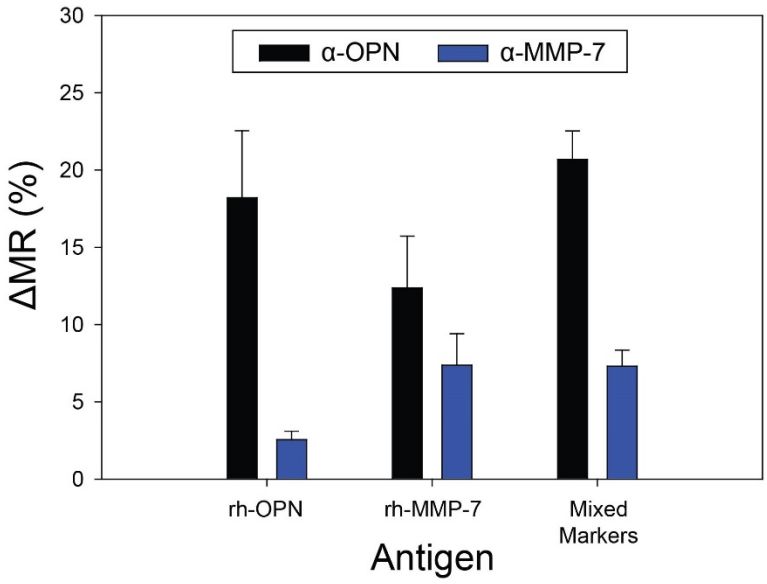

Figure 5.10 Cross reactivity of rh-OPN and rh-MMP-7 in diluted human serum (1:4 v/v pooled human serum:PBS). The final concentration of antigen solutions is 7.5 ng/mL after dilution. Error bars represent average of MR responses from five gold addresses.

MMP-7, as shown in the first set of columns of Figure 5.10. This result shows that rh-OPN in serum selectively binds to its respective capture antibody (*i.e.*, α-OPN) in the presence of α-MMP-7.

However, rh-MMP-7 in diluted serum appears to bind to addresses modified with α-OPN and α-MMP-7. When the assay substrate with two capture antibodies for rh-OPN and rh-MMP-7 was exposed only to rh-MMP-7, the average MR response from gold addresses modified with the capture α-OPN was higher than that from gold addresses with α-MMP-7. Given that the cross reactivity study in buffer (Figure 5.7) showed minimal cross reactivity between these two markers, we suspect that other components in human serum interact with rh-MMP-7, which arises in the nonspecific binding of rh-MMP-7 to the capture antibodies of rh-OPN. Thus, the translation of these immunoassays to clinical diagnostics requires further understanding of fundamentals regarding interactions between

biomarkers, antibodies, and serum components.

5.4 Conclusion

Many studies have suggested that earlier diagnosis of PDAC is critical in improving patient outcomes. In order to accurately diagnose pancreatic cancer in its early stages, screening a panel of markers simultaneously from small serum samples is required. This chapter described efforts toward the development of GMR-based immunoassays for the simultaneous detection of potential PDAC markers (rh-OPN, rh-CEACAM-1, rh-TIMP-1, and rh-MMP-7). Using in-house magnetic labels, the dose response curves for all four PDAC markers gave LoDs in sub-nanogram per milliliter levels when spiked in PBS with 1% BSA. Cross reactivity studies in buffer showed no significant interactions between the four markers, as predicted by the protein BLAST analysis. Upon dilution in untreated human serum, the dose response curves for rh-OPN and rh-MMP-7 gave LoDs of 840 and 499 pg/mL in neat and diluted human serum, respectively, which are lower than the clinically relevant marker levels of rh-OPN and rh-MMP-7 in PDAC patients. However, cross reactivity studies of rh-OPN and rh-MMP-7 in human serum revealed that, while rh-OPN does not show cross reactivity to MMP-7 capture antibody, rh-MMP-7 does bind nonspecifically to the OPN capture antibody, which limits the simultaneous detection of these markers in a sample. Thus, the detection of these markers in human serum poses some difficulties, such as possible complexation with unknown serum components. To this end, understanding the underlying biology in immunoassays (*e.g.*, interaction between antibodies, antigens, and serum components) may be pivotal in translating this platform to a more clinically relevant setting.

Overall, we have shown that our GMR platform can simultaneously detect four markers in buffer at relevant clinical levels. With our current format for the assay substrate, our MR immunoassays can multiplex up to 12 different markers in principle, given the 12 gold addresses present on each substrate. However, we anticipate that this format is easily scalable to hundreds of markers with the further development in the design of the assay substrate and GMR sensors. With the potential for high throughput and small required sample volumes, we foresee that this platform can be further used for new marker panel discovery and validation. Regardless, we believe that, with the improvement of biological aspects of immunoassays, a GMR-based diagnostic platform has great potential for early detection of disease in the clinical setting.

5.5 References

(1) Chen, R.; Crispin, D.; Pan, S.; Hawley, S.; McIntosh, M. W.; May, D.; Anton-Culver, H.; Ziogas, A.; Bronner, M. P.; Brentnall, T. A., *Pancreas* **2010,** *39*, 981.

(2) Poruk, K. E.; Firpo, M. A.; Adler, D. G.; Mulvihill, S. J., *Ann. Surg.* **2013,** *257*, 17.

(3) Siegel, R. L.; Miller, K. D.; Jemal, A., *CA Cancer J. Clin.* **2016,** *66*, 7-30.

(4) Swords, D. S.; Firpo, M. A.; Scaife, C. L.; Mulvihill, S. J., *Onco Targets Ther.* **2016,** *9*, 7459.

(5) Winter, J. M.; Cameron, J. L.; Lillemoe, K. D.; Campbell, K. A.; Chang, D.; Riall, T. S.; Coleman, J.; Sauter, P. K.; Canto, M.; Hruban, R. H., *Ann. Surg.* **2006,** *243*, 673-683.

(6) Bergquist, J. R.; Puig, C. A.; Shubert, C. R.; Groeschl, R. T.; Habermann, E. B.; Kendrick, M. L.; Nagorney, D. M.; Smoot, R. L.; Farnell, M. B.; Truty, M. J., *J. Am. Coll. Surg.* **2016,** *223*, 52-65.

(7) Kannagi, R., *Chang Gung Med. J.* **2007,** *30*, 189.

(8) Ørntoft, T. F.; Vestergaard, E. M.; Holmes, E.; Jakobsen, J. S.; Grunnet, N.;

Mortensen, M.; Johnson, P.; Bross, P.; Gregersen, N.; Skorstengaard, K., *J. Biol. Chem.* **1996,** *271*, 32260-32268.

(9) Ballehaninna, U. K.; Chamberlain, R. S., *J. Gastrointest. Oncol.* **2011,** *3*, 105-119.

(10) Homma, T.; Tsuchiya, R., *Int. J. Pancreatol.* **1991,** *9*, 119-124.

(11) Kim, J. E.; Lee, K. T.; Lee, J. K.; Paik, S. W.; Rhee, J. C.; Choi, K. W., *J. Gastroenterol. Hepatol.* **2004,** *19*, 182-186.

(12) Firpo, M. A.; Boucher, K. M.; Mulvihill, S. J., *Theor. Biol. Med. Modell.* **2014,** *11*, 34.

(13) Firpo, M. A.; Gay, D. Z.; Granger, S. R.; Scaife, C. L.; DiSario, J. A.; Boucher, K. M.; Mulvihill, S. J., *World J. Surg.* **2009,** *33*, 716-722.

(14) Gold, D. V.; Modrak, D. E.; Ying, Z.; Cardillo, T. M.; Sharkey, R. M.; Goldenberg, D. M., *J. Clin. Oncol.* **2006,** *24*, 252-258.

(15) Grote, T.; Logsdon, C. D., *Curr. Opin. Gastroenterol.* **2007,** *23*, 508-514.

(16) Joergensen, M. T.; Brünner, N.; De Muckadell, O. B. S., *Anticancer Res.* **2010,** *30*, 587-592.

(17) Köklü, S.; Yilmaz, F. M.; Başar, Ö.; Yilmaz, G.; Yüksel, O.; Yildrim, E.; Öztürk, Z. A., *Pancreatology* **2007,** *7*, 526-530.

(18) Koopmann, J.; Fedarko, N. S.; Jain, A.; Maitra, A.; Iacobuzio-Donahue, C.; Rahman, A.; Hruban, R. H.; Yeo, C. J.; Goggins, M., *Cancer Epidemiol. Biomarkers Prev.* **2004,** *13*, 487-491.

(19) Kuhlmann, K. F.; Van Till, J. O.; Boermeester, M. A.; De Reuver, P. R.; Tzvetanova, I. D.; Offerhaus, G. J. A.; Ten Kate, F. J.; Busch, O. R.; Van Gulik, T. M.; Gouma, D. J., *Cancer Epidemiol. Biomarkers Prev.* **2007,** *16*, 886-891.

(20) Poruk, K. E.; Firpo, M. A.; Scaife, C. L.; Adler, D. G.; Emerson, L. L.; Boucher, K. M.; Mulvihill, S. J., *Pancreas* **2013,** *42*, 193.

(21) Simeone, D. M.; Ji, B.; Banerjee, M.; Arumugam, T.; Li, D.; Anderson, M. A.; Bamberger, A. M.; Greenson, J.; Brand, R. E.; Ramachandran, V., *Pancreas* **2007,** *34*, 436-443.

(22) Bloomston, M.; Shafii, A.; Zervos, E. E.; Rosemurgy, A. S., *J. Surg. Res.* **2002,** *102*, 39-44.

(23) Harsha, H.; Kandasamy, K.; Ranganathan, P.; Rani, S.; Ramabadran, S.; Gollapudi, S.; Balakrishnan, L.; Dwivedi, S. B.; Telikicherla, D.; Selvan, L. D. N., *PLoS Med.* **2009,** *6*, e1000046.

(24) Zhou, W.; Sokoll, L. J.; Bruzek, D. J.; Zhang, L.; Velculescu, V. E.; Goldin, S. B.; Hruban, R. H.; Kern, S. E.; Hamilton, S. R.; Chan, D. W., *Cancer Epidemiol. Biomarkers Prev.* **1998,** *7*, 109-112.

(25) Grünberg, P. A., *Rev. Mod. Phys.* **2008,** *80*, 1531.

(26) Baselt, D. R.; Lee, G. U.; Natesan, M.; Metzger, S. W.; Sheehan, P. E.; Colton, R. J., *Biosens. Bioelectron.* **1998,** *13*, 731-739.

(27) De Boer, B.; Kahlman, J.; Jansen, T.; Duric, H.; Veen, J., *Biosens. Bioelectron.* **2007,** *22*, 2366-2370.

(28) Edelstein, R.; Tamanaha, C.; Sheehan, P.; Miller, M.; Baselt, D.; Whitman, L.; Colton, R., *Biosens. Bioelectron.* **2000,** *14*, 805-813.

(29) Srinivasan, B.; Li, Y.; Jing, Y.; Xu, Y.; Yao, X.; Xing, C.; Wang, J. P., *Angew. Chem., Int. Ed.* **2009,** *48*, 2764-2767.

(30) Tondra, M.; Porter, M.; Lipert, R. J., *J. Vac. Sci. Technol., A* **2000,** *18*, 1125-1129.

(31) Wang, S. X.; Bae, S.-Y.; Li, G.; Sun, S.; White, R. L.; Kemp, J. T.; Webb, C. D., *J. Magn. Magn. Mater.* **2005,** *293*, 731-736.

(32) Gaster, R. S.; Hall, D. A.; Nielsen, C. H.; Osterfeld, S. J.; Yu, H.; Mach, K. E.; Wilson, R. J.; Murmann, B.; Liao, J. C.; Gambhir, S. S., *Nat. Med.* **2009,** *15*, 1327-1332.

(33) Gaster, R. S.; Xu, L.; Han, S.-J.; Wilson, R. J.; Hall, D. A.; Osterfeld, S. J.; Yu, H.; Wang, S. X., *Nat. Nanotechnol.* **2011,** *6*, 314-320.

(34) Millen, R. L.; Nordling, J.; Bullen, H. A.; Porter, M. D.; Tondra, M.; Granger, M. C., *Anal. Chem.* **2008,** *80*, 7940-7946.

(35) Nordling, J.; Millen, R. L.; Bullen, H. A.; Porter, M. D.; Tondra, M.; Granger, M. C., *Anal. Chem.* **2008,** *80*, 7930-7939.

(36) Young, C. C.; Blackley, B. W.; Porter, M. D.; Granger, M. C., *Anal. Chem.* **2016,** *88*, 2015-2020.

(37) Noh, S.-h.; Na, W.; Jang, J.-t.; Lee, J.-H.; Lee, E. J.; Moon, S. H.; Lim, Y.; Shin, J.-S.; Cheon, J., *Nano Lett.* **2012,** *12*, 3716-3721.

(38) Bai, F.; Wang, D.; Huo, Z.; Chen, W.; Liu, L.; Liang, X.; Chen, C.; Wang, X.; Peng, Q.; Li, Y., *Angew. Chem., Int. Ed.* **2007,** *46*, 6650-6653.

(39) Zhuang, J.; Wu, H.; Yang, Y.; Cao, Y. C., *Angew. Chem., Int. Ed.* **2008,** *47*, 2208-2212.

(40) Leelawat, K.; Narong, S.; Wannaprasert, J.; Ratanashu-Ek, T., *World J. Gastroenterol.* **2010,** *16*, 4697-4703.

(41) Johnson, M.; Zaretskaya, I.; Raytselis, Y.; Merezhuk, Y.; McGinnis, S.; Madden, T. L., *Nucleic Acids Res.* **2008,** *36*, W5-W9.

(42) Ismail, A. A., *Clin. Chem.* **2005,** *51*, 25-26.

(43) Selby, C., *Ann. Clin. Biochem.* **1999,** *36*, 704-721.

(44) Sturgeon, C. M.; Viljoen, A., *Ann. Clin. Biochem.* **2011,** *48*, 418-432.

CHAPTER 6

CONCLUSION

6.1 Research Overview

The development of a diagnostic platform for early disease detection remains challenging. This reflects the need to integrate a sensitive detection system, a panel of reliable disease markers, bioanalytical techniques, and effective labeling strategies. Furthermore, an effective diagnostic tool for early disease detection should have a short turnaround time, low cost, multiplexing capability, and processes for sample pretreatment/purification if needed. The recent progress and advancements in nanoparticle synthesis, microfabrication, and molecular diagnostics have enabled the development of novel diagnostic platforms for the detection of disease markers with increased performance, including a high level of sensitivity, rapid analysis, and multiplexing. Among many technologies, one such diagnostic tool is based on giant magnetoresistance (GMR). Due to its high sensitivity and potential in rapid and multiplexed detection, a GMR sensing device has shown promise in early detection of disease. This dissertation focused on the development of magnetic labels and their usage in GMR-based immunoassays, especially for the detection of potential pancreatic cancer markers. The body of this work included: (1) stabilization of magnetic nanoparticles (MNPs) using silica coating; (2) synthesis and

magnetic characterization of MNP assemblies; (3) preparation of magnetic labels with high magnetic moment (***m***) and colloidal stability using MNP assemblies; and (4) validation of the utility of GMR-based immunoassays for the simultaneous detection of potential pancreatic cancer markers.

Stable suspensions of MNPs with high ***m*** have widespread utility in biological applications. It is challenging, however, to stabilize ferro-/ferrimagnetic nanoparticles with high ***m*** in solution due to the strong magnetic forces that facilitate aggregation of the MNPs. Chapter 2 describes the preparation of stable, discrete silica-coated ferrimagnetic zinc ferrite nanocubes (ZFNCs) with high ***m***. These results show that successful creation of discrete silica-coated ZFNCs is realized only after depositing multiple polyelectrolyte layers prior to silica coating. The intermediate polyelectrolyte layers play a significant role in preventing ZFNCs from aggregating during silica encapsulation. This encapsulation method can be implemented to easily prepare individual silica-coated MNPs with high ***m*** for use in various biological applications.

To use MNPs as labels in GMR-based immunoassays, the MNPs must be superparamagnetic and have a high ***m***. In addition, the MNPs should be easily conjugated with molecular recognition elements to tag a specific target, while avoiding aggregation and sedimentation. Chapter 3 describes the fabrication of colloidal assembly of zinc ferrite nanoparticles (ZFNPs) to design a new magnetic material with superparamagnetism and a high ***m*** for label application. Furthermore, this chapter includes an investigation of the effect of nanoparticle assembly on magnetic properties. This study revealed that assembling ZFNPs into zinc ferrite magnetic beads (ZFMBs) led to an enhancement in the anisotropic energy barrier, due to an increase in the magnitude of magnetic dipolar

interactions. Interestingly, ZFMBs remain superparamagnetic at room temperature. More importantly, a single ZFMB can produce ~4,000 times larger ***m*** than that of a single ZFNP. This demonstrates the utility of superparamagnetic ZFMBs as magnetic labels for magnetic immunoassays. To this end, Chapter 4 describes the preparation of superparamagnetic ZFMB as magnetic labels. The primary steps for ZFMB labels consist of surface functionalization of ZFMBs with polyacrylic acid, and streptavidin conjugation via carbodiimide chemistry. The streptavidin ZFMBs are superior to commercially available magnetic beads (Dynabeads and Turbobeads) with respect to colloidal stability and assay performance. The work presented in Chapters 3 and 4 can be extended to other biological applications, where superparamagnetic particles with a high ***m*** and colloidal stability are needed.

Lastly, Chapter 5 focuses on the utilization of ZFMBs as magnetic labels in GMR-based immunoassays for the detection of potential pancreatic cancer markers (rh-OPN, rh-CEACAM-1, rh-TIMP-1, and rh-MMP-7). The immunoassays showed a sub-nanogram limit of detection for each marker spiked in buffer. Cross reactivity studies among these markers in buffer showed a low degree of cross reactivity among all markers, which corresponds with the results predicted by BLAST analysis. In addition, the limits of detection for rh-OPN and rh-MMP-7 in human serum was comparable to those of these markers in buffer solutions. Unfortunately, the remaining two markers, rh-CEACAM-1 and rh-TIMP-1, showed assay interferences (*i.e.*, low analytical sensitivity and high nonspecific adsorption in blanks) when spiked in human serum. Cross reactivity study of rh-OPN and rh-MMP-7 in human serum revealed that rh-MMP-7 nonspecifically binds to the OPN capture antibody, which hampered the simultaneous detection of rh-OPN and rh-

MMP-7 in human serum. Nonetheless, along with the further understanding in biological aspects of immunoassays, this GMR-based diagnostic platform is believed to be a promising tool for multiplexed detection of disease markers.

6.2 Future Directions

The development of a GMR-based multiplexing diagnostic platform for disease detection is an active and attractive subject in bioanalytical areas. Many ongoing and future efforts aim at translating the GMR-based detection platform to a point-of-care (PoC) format (*i.e.*, rapid, field deployable, and easy to use). To realize a GMR-based PoC test, further optimization of magnetic labels, instrumentation, and assays would be needed, as described below.

The development of MNP labels with a high $\boldsymbol{m}$ should be ongoing. As magnetic characteristics and target specificity of the labels are closely related to the performance of a GMR-based test, finding the optimal balance between magnetic characteristics and particle binding behavior would improve detection limits and aid in the utilization of a GMR-based detection system.

To realize a GMR-based PoC test, GMR instrumentation needs to become smaller to be more portable. Due to the advances in fabrication methods (*e.g.*, microfabrication and lithography), it is anticipated that portable GMR systems may soon be available. Combining a GMR readout with paper-based immunoassays (*e.g.*, lateral flow assays) may be a good candidate for rapid and field-deployable, GMR-based testing.

Most importantly, multiplexed detection of analytes, which remains a big hurdle for molecular diagnostics, should be extensively explored. To this end, understanding the

underlying biology in immunoassays (*e.g.*, interactions between antibodies, antigens, and serum components) will be critical to achieving multiplexed detection and, subsequently, translating this platform to clinical and PoC settings.

APPENDIX A

SUPPORTING INFORMATION FOR CHAPTER 2

A.1. Experimental Details

A.1.1. Dynamic Light Scattering (DLS)

For hydrodynamic size measurements, the back-scattered mode was used at an angle of 174˚. Diffusion coefficients of MNP samples were obtained by fitting the correlation function with the cumulants analysis algorithm.[1] The Stokes-Einstein equation was then utilized to convert the diffusion coefficient to the hydrodynamic diameter. The measurement duration was set to 2 min and three measurements were made for each sample to quantify measurement reproducibility.

The Smoluchowski approximation was used to calculate the ζ-potential from the measured electrophoretic mobility of the particles (U_E), which is given as:

$$\zeta = \frac{\eta}{\varepsilon} U_E \qquad \text{(A.1)}$$

where η and ε are the viscosity and the dielectric constant of water (η = 0.8872 cP and ε = 78.5), respectively. The Smoluchowski approximation is applicable when the particle size is larger than the Debye length of the electrical double layer in a polar medium. The reported ζ-potential values are an average of three measurements per sample, where each

measurement is an average of 15 sub-runs.

A.1.2. Remanent Magnetization Measurements

The interparticle interactions of magnetic samples were investigated by IRM and DCD. For the IRM analysis, samples were ac-demagnetized and then exposed to a magnetic field ($\boldsymbol{H}$). The remanence magnetization, $\boldsymbol{M_{IRM}(H)}$, was measured at $\boldsymbol{H} = 0$. This cycle was repeated by increasing $\boldsymbol{H}$ to the point in which the saturation field, $\boldsymbol{H_{MAX}}$, is reached ($\boldsymbol{H_{MAX}}$ = 2,000 Oe for the ZFNC samples) and $\boldsymbol{M_{IRM}(H)}$ is the correspoding saturation value, $\boldsymbol{M_{IRM}}(\infty)$. The DCD experiment was carried out in a similar manner, but the sample was first saturated at $-\boldsymbol{H_{MAX}}$ and $\boldsymbol{M_{DCD}(H)}$ was obtained by stepping $\boldsymbol{H}$ in the opposite direction to $+\boldsymbol{H_{MAX}}$. The $\boldsymbol{M_{DCD}(H)}$ measured at field saturation is termed $\boldsymbol{M_{DCD}}(\infty)$. We note that $\boldsymbol{H_{MAX}}$ is the field at which saturation magnetization, $\boldsymbol{M_s}$, of the specimen is reached.

The IRM and DCD data were used to construct Henkel and delta-$\boldsymbol{m}$ (δm) plots. These plots are generally used to examine the type and strength of interactions between magnetic particles. For an assembly of single-domain ferromagnetic particles with uniaxial anisotropy, the relationship between $\boldsymbol{M_{IRM}(H)}$ and $\boldsymbol{M_{DCD}(H)}$ is given by the Wohlfarth relation:[2]

$$m_d(H) = (1 - 2m_r(H)) \qquad \text{(A.2)}$$

where m_r and m_d denote the reduced terms of $\boldsymbol{M_{IRM}(H)}/\boldsymbol{M_{IRM}}(\infty)$ and $\boldsymbol{M_{DCD}(H)}/\boldsymbol{M_{DCD}}(\infty)$, respectively. A method to assess the type of interactions (*e.g.*, dipole-

dipole) between particles consists of plotting $m_d(H)$ vs. $m_r(H)$, the so-called Henkel plot.[3] In an assembly of non-interacting particles, the Henkel slope is -2 and is termed the Wohlfarth line. Negative deviations from the Wohlfarth line indicate that demagnetizing interactions predominate the system (*e.g.*, dipole-dipole interaction that stabilize the demagnetized state),[4] while a positive deviation is attributed to interactions promoting a magnetized state (*e.g.*, interparticle super-exchange interactions or RKKY-like coupling).[5] In order to retain field information, a further term, δm, was introduced into the relationship[6] by Kelly et al.:

$$\delta m = m_d(H) - (1 - 2m_r(H)) \qquad \text{(A.3)}$$

where δm can conceptually be viewed to be twice the difference between the fraction of particles whose dipole orientation is switched at a particular field in IRM mode and DCD mode.

A.2. Estimation of Magnetic Moment per Particle

Virgin magnetic curves of demagnetized magnetic samples were measured by applying a magnetic field from 0 to 10,000 Oe. Figure A.5 is the representative virgin curve of the ZFNCs and Turbobeads®. It is assumed that the mass of surface capping molecules are negligible compared to that of the MNPs and the densities of the ZFNCs and Turbobeads are equal to those of bulk magnetite and cobalt. Basis for the calculation of magnetic moment per particle is 1 g of the sample. For example, the calculation of magnetic moment per particle of the ZFNCs is described below.

- Basis: 1 g of the MNPs
- Average edge length of the MNPs: 129 nm = 1.29×10^{-5} cm
- Volume of one cubic MNP

$$V_{MNP} = L^3 = (1.29\times10^{-5})^3 = 2.15 \times 10^{-15}\ cm^3/particle$$

- Density of the MNPs: 5.175 cm^3
- Total volume of the basis (V_{total}): 0.193 cm^3
- The number of the ZNFCs in the basis

$$N_{MNP,1g} = \frac{V_{total}}{V_{MNP}} = \frac{0.193\ cm^3}{2.15\times10^{-15}cm^3/particle} = 9.00 \times10^{13}\ particles$$

- Magnetic moment of one MNP at 150 Oe

$$M_{150\ Oe} = \frac{m_{150\ Oe}}{N_{MNP,1g}} = \frac{37.7\ emu}{9.00\times10^{13}\ particles} = 4.19\times10^{-13}emu/particle$$

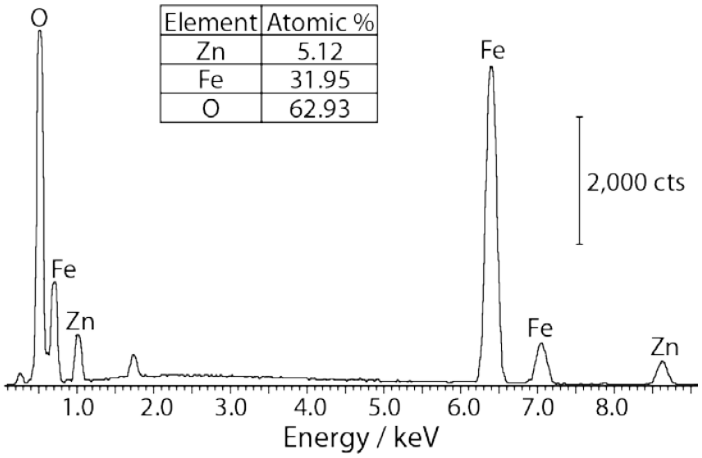

Figure A.1. EDX spectrum of as-synthesized ZFNCs by SEM.

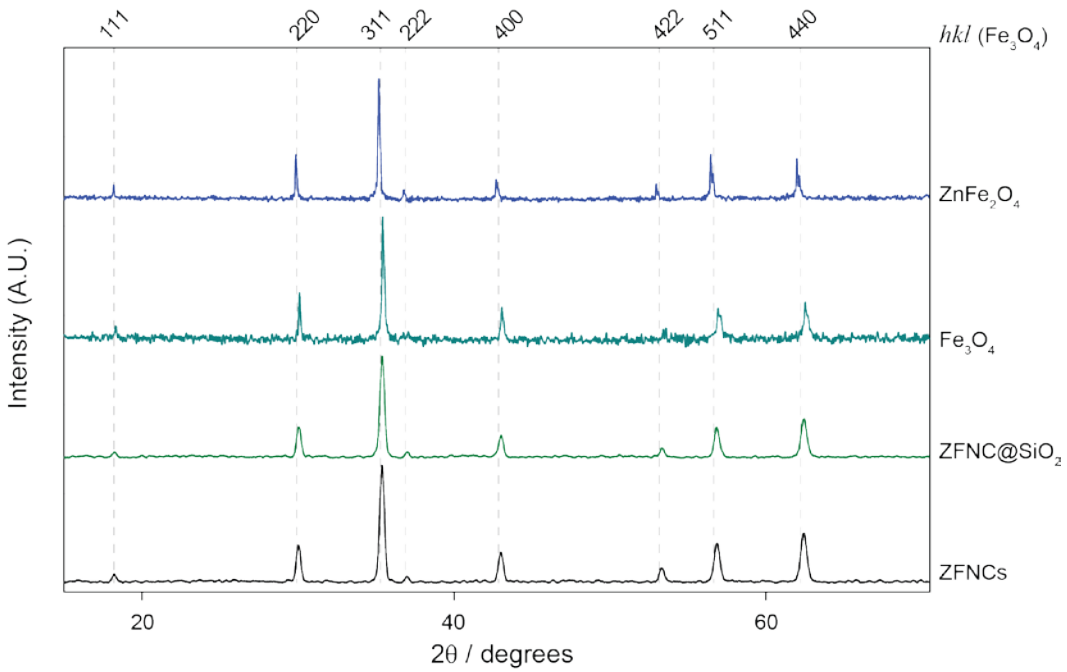

Figure A.2. XRD diffractograms of as-synthesized ZFNCs and ZFNC@SiO_2 particles. Magnetite (Fe_3O_4) and zinc ferrite ($ZnFe_2O_4$) library diffractograms are shown for comparison.

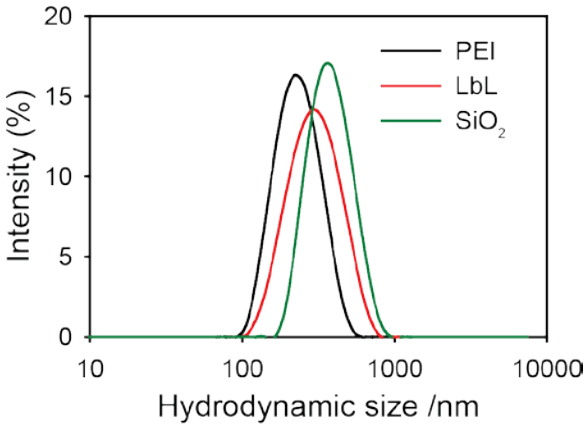

Figure A.3. Particle size distributions from DLS measurement for (black) PEI-, (red) multiple polyelectrolyte-, and (green) silica-coated ZFNCs.

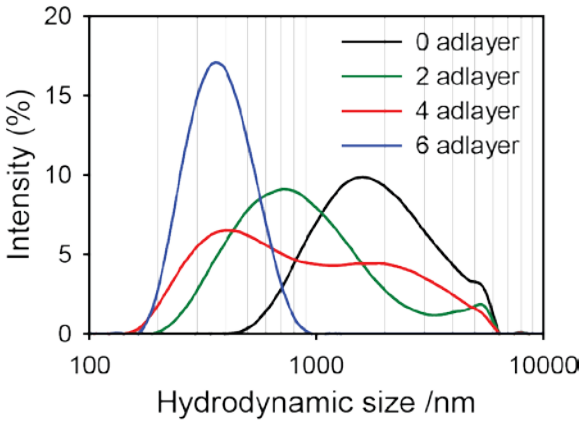

Figure A.4. Hydrodynamic sizes of the silica-coated ZFNCs. Prior to the silica coating, the ZFNCs had different number of polyelectrolyte layers; (black) 0, (green) 2, (red) 4, and (blue) 6 layers. The size of silica-coated ZFNCs, appearing above 1000 nm, are due to large aggregates and/or the linear chaining of the ZFNCs when the seed ZFNCs are coated with fewer than six polyelectrolyte layers.

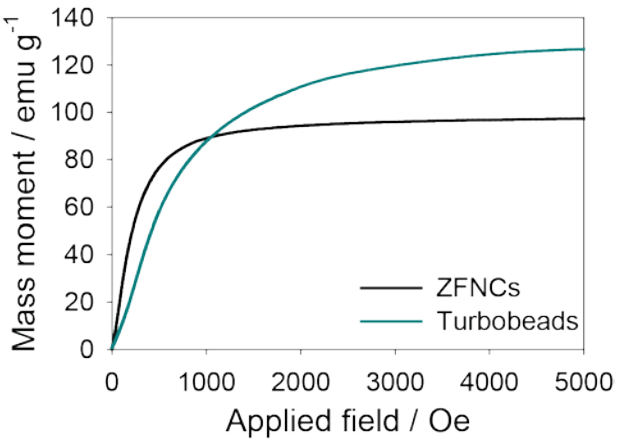

Figure A.5. Virgin magnetic curves of demagnetized samples; (black) ZFNCs and (red) Turbobeads.

Table A.1. Comparison of particle sizes measured using SEM and DLS. Note that the corner-to-corner length of particles was obtained by multiplying $\sqrt{3}$ to the edge length measured by SEM.

	SEM		**DLS**
Size (nm)	$\boldsymbol{l}$	$\boldsymbol{l\times\sqrt{3}}$	$\boldsymbol{D_{h,int}}$ **with FWHM**
PEI-coated ZFNCs	129 ± 15	224 ± 26	242 ± 80.2
Polyelectrolyte-coated ZFNCs	N.A.	N.A.	316 ± 120.1
Silica-coated ZNFCs	220 ± 17	381 ± 30	394 ± 126.5

Table A.2. The magnetic moment per particle for different MNPs.

Source	Catalog number	Size (nm)	$M_{30\ Oe}$ (emu)	$M_{150\ Oe}$ (emu)	M_s (emu)	Reference
Ocean NanoTech	SHS-10	10	0.02×10^{-16}	-	0.82×10^{-16}	[7]
Ocean NanoTech	SHS-20	20	1.1×10^{-16}	-	7.8×10^{-16}	[7]
Ocean NanoTech	SHS-30	30	1.05×10^{-16}	-	10.8×10^{-16}	[7]
Miltenyi Biotech	MACS 130-048-102	50	23×10^{-16}	-	81×10^{-16}	[7]
Ademtech	ADM03210	100	18×10^{-16}	-	368×10^{-16}	[7]
Turbobeads	Turbobeads Carboxy	30	4.06×10^{-16}	19.7×10^{-16}	1.63×10^{-14}	-
In-house	ZFNCs	130	706×10^{-16}	4.2×10^{-13}	1.09×10^{-12}	-

A.3. References

(1) Malvern Instruments, Dynamic Light Scattering: An Introduction in 30 Minutes, Document No. MRK656-01; Malvern Instruments: Malvern, United Kingdom, 2015.

(2) Wohlfarth, E., Relations between different modes of acquisition of the remanent magnetization of ferromagnetic particles. *J. Appl. Phys.* **1958**, 29, 595-596.

(3) Henkel, O., Remanenzverhalten und Wechselwirkungen in hartmagnetischen Teilchenkollektiven. *Phys. Status Solidi B* **1964**, 7, 919-929.

(4) Laureti, S.; Varvaro, G.; Testa, A.; Fiorani, D.; Agostinelli, E.; Piccaluga, G.; Musinu, A.; Ardu, A.; Peddis, D., Magnetic interactions in silica coated nanoporous assemblies of CoFe2O4 nanoparticles with cubic magnetic anisotropy. *Nanotechnology* **2010**, 21, 315701.

(5) Binns, C., Nanomagnetism: Fundamentals and Applications. Elsevier: Amsterdam, 2014; Vol. 6.

(6) Kelly, P.; O'Grady, K.; Mayo, P.; Chantrell, R., Switching mechanisms in cobalt-phosphorus thin films. *IEEE Trans. Magn.* **1989**, 25, 3881-3883.

(7) Wang, W.; Wang, Y.; Tu, L.; Feng, Y.; Klein, T.; Wang, J.-P., Magnetoresistive performance and comparison of supermagnetic nanoparticles on giant magnetoresistive sensor-based detection system. *Sci. Rep.* **2014**, 4, 1-5.

APPENDIX B

SUPPORTING INFORMATION FOR CHAPTER 3

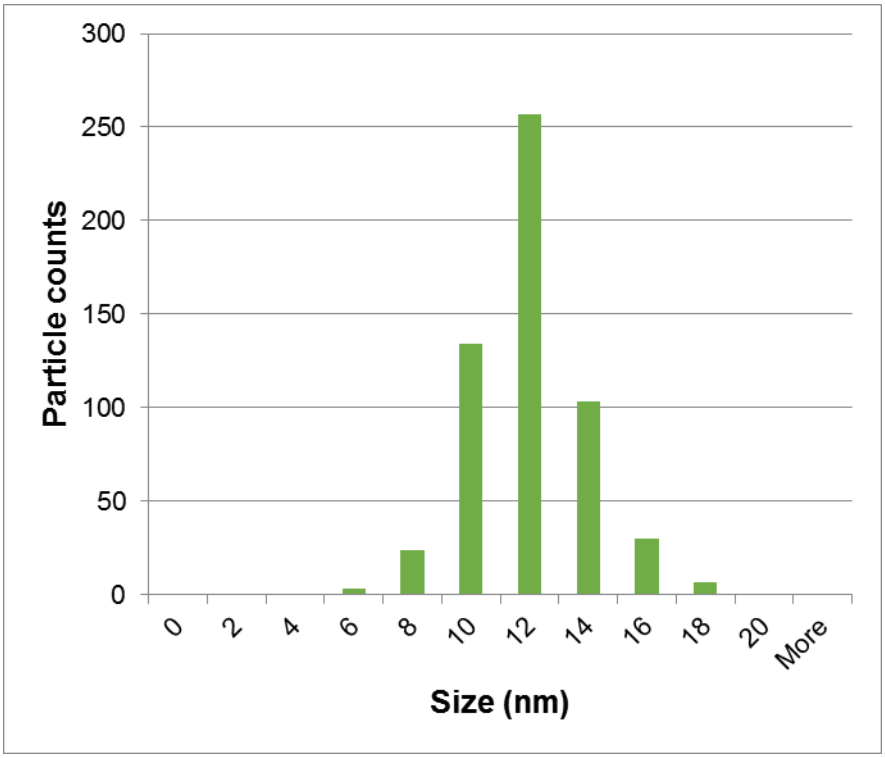

Figure B.1 Histogram of the diameter of as-synthesized ZFNPs.

APPENDIX C

SUPPORTING INFORMATION FOR CHAPTER 4

C.1. Experimental Details

C.1.1. Assay Substrate Configuration and Fabrication

The design and layout of the assay substrates, which consist of alternating nickel and gold addresses, are shown in Figure C.1D. Figure C.1D shows the entire substrate: twelve gold addresses are interspersed between thirteen nickel addresses. Both nickel and gold addresses are 200 × 200 μm in size. Each gold address is spaced (edge to edge) 500 μm from its neighboring nickel addresses. The nickel and gold addresses are used for reference magnetic signals and assay areas, respectively.[1-3]

The assay substrate was created using photolithographic and lift-off techniques. The detailed preparation of the assay substrate can be found elsewhere.[1-3] Briefly, the assay substrates were fabricated by evaporating nickel (10-nm thick) and gold (200-nm thick) addresses on Pyrex wafers (2-mm thick). Prior to the evaporation of nickel and gold, a 10-nm thick chromium layer was deposited as an adhesion layer. To prevent possible oxidation of nickel addresses, a 15-nm thick titanium layer was overlaid on the nickel addresses. In the next step, the entire wafer was coated with parylene, which was then removed from the gold addresses by plasma etching. The wafer was then diced into

individual 0.3 × 2.0 cm rectangular sticks (the substrate).

C.1.2. MR Sensor and Station

The MR sensor was provided by NVE Corp., the details of which have been described elsewhere, along with those for the magnetics test station.[2-4] The sensor (Figure C.1C) is designed as an integrated circuit of four resistors in a Wheatstone bridge configuration. The two interdigitated resistors function as a sense pad (200 × 200 μm in size). The other two resistors act as reference resistors, which have 30-μm offsets from the sense pad. The MR sensors are coated with a 250-nm protective layer of silicon nitride (Si_3N_4).

The MR station provides for relative motion between the assay substrate and MR sensor in the directions of *x*-, *y*- and *z*-axes as described in Figure C.2. For readout, the sensor was placed between two electromagnetic coils (Nicollet Technologies Corp., Minneapolis, MN) in a Helmholtz configuration. Once an assay substrate was placed inverted above the sensor, the separation distance (*d*, *z*-axis) between the sensor and assay substrate was adjusted by a four-phase stepper motor (STMicroelectronics L298N). Because the MR signal magnitude is dependent on *d*, it is critical to maintain a constant *d* throughout the substrate scanning. Also, the tilt angle of the assay substrate in the *z*-axis was manipulated by an Oriel controller, which has a resolution of $(2.0 \pm 0.1) \times 10^{-3}$ degree per step, in order to prevent a change in *d* across the assay substrate while scanning. This process of changing the tilt angle was used to adjust the assay substrate until the plane of the substrate was parallel to the *x*-*y* plane of the MR sensor pad. Tilt in *y*-axis was manually aligned. To measure MR signals, the translation of the sensor across the

assay substrate in the *x*-axis was controlled by a micromanipulator (Model 6000, Micromanipulator Co., Carson City, NV) with a second four-stage stepper motor.

C.1.3. MR Signal Analysis Method

To measure MR signals, an applied field of 100 Oe was chosen after careful characterization of the transfer curve and noise of the MR sensor. The *d* between the substrate and MR sensor was set at 10 ± 1.0 μm. The translational scanning speed of the assay substrate along the addresses was 31.1 ± 0.1 μm/sec.

In order to quantitatively measure MR responses, we incorporate magnetic reference addresses (*i.e.*, nickel addresses).[1-2] The MR signals from nickel addresses not only account for any change in *d*, but also provides for normalization of the MR signal from each gold address. As illustrated in Figure C.2B, the normalized response ($\boldsymbol{MR}_{norm,i}$) from the *i*th gold address with respect to the two Ni addresses in closest proximity can be written as follows,

$$\boldsymbol{MR}_{norm,i} = \frac{2\Delta E_{Au,i}}{\Delta E_{Ni,i-1} + \Delta E_{Ni,i+1}} \qquad \text{(B1.1)}$$

where ΔE_{Au} and ΔE_{Ni} represent the responses (voltage changes) of gold and nickel addresses, respectively.

The MR response for each antigen concentration was determined by averaging the MR responses from twelve replicates gold addresses on one substrate. Similarly, the standard deviation for each MR data point was obtained from the twelve gold addresses

on each substrate.

C.1.4. Sample Characterization and Measurements

Scanning electron microscope (SEM) images were collected using a Hitachi S-4800 (Japan), which was equipped with an energy dispersive X-ray spectroscopy module (EDS, INCA Inc.). Particle samples were prepared by dropcasting onto a 1×1 cm silicon chip for SEM imaging and EDS. For transmission electron microscopy (TEM), samples were prepared by dropcasting onto a 3-mm lacey carbon grid and images were obtained using JEM-2800 (JEOL, Japan). For the estimation of average particle size, ImageJ was used and at least 250 particles were measured for each sample.

Infrared (IR) transmission spectra were obtained using a Nicolet Magna 850 Fourier transform IR spectrometer. The particle samples were dispersed in a KBr pellet at the concentration of ~1% (w/w). Spectra were collected using 512 scans at a resolution of 1 $cm.^{-1}$

Hydrodynamic size and zeta (ζ)-potential measurements were obtained by dynamic light scattering. A Zetasizer Nano (Malvern Instruments, United Kingdom) with a disposable folded capillary cell was used to measure the zeta (ζ)-potential and hydrodynamic sizes of the suspended particles. At least three measurements per sample (n=3) were taken to calculate average values of hydrodynamic size and ζ-potential.

A system of nanoparticle tracking analysis (NanoSight LM10, Malvern Instruments, United Kingdom) was used to measure the concentration of magnetic labels. At least three aliquots per magnetic label were measured to estimate the average concentration of magnetic labels.

Magnetic hysteresis measurements were performed with a vibrating sample magnetometer (VSM EZ7, MicroSense, Lowell, MA) at room temperature.

A fluorescent microscope (BX50WI, Olympus, Japan) equipped with a fluorescent cube (U-N41012) and a 12.8 megapixel CCD camera (DP72) was used to capture fluorescent images of FITC-avidin tagged ZFMB labels. A droplet of the FITC-avidin tagged ZFMB labels was sandwiched between a microscope glass slide and cover slip for imaging.

Inductively coupled plasma collision cell quadrupole mass spectrometer (Agilent 7500ce) was used to determine the composition of Zn and Fe in the ZFNPs. Dried ZFNPs were digested in 3 mL concentrated HCl and 1 mL concentrated HNO_3 (trace metal grade) and diluted with 5% HNO_3 to about 200 ppb Fe and 10 ppb Zn. A calibration solution containing 200 ppb Fe and 10.0 ppb Zn was prepared using single element standard solutions (Inorganic Ventures). Diluted sample and calibration solution were run together using a double-pass spray chamber, quartz injector, and platinum cones. Collision cell flushed with He (8 mL/min) was used in order to decrease the $^{40}Ar^{16}O$ interference at mass 56.

C.2. Estimation of Magnetic Moment per Particle

To estimate magnetic moment per particle, $\boldsymbol{m}_{particle}$, two main assumptions were used: (1) surface capping molecules are negligible; and (2) the densities of the ZFNPs, Turbobead®, and Dynabead® are equal to magnetite, cobalt, and the value given by the vendor, respectively. The $\boldsymbol{m}_{particle}$ is calculated based on 1 g of the sample. The calculation for $\boldsymbol{m}_{particle}$ of the Dynabeads is given as an example. The diameter (D) and density (ρ) of

the Dynabeads provided by the vendor are 1.05 μm and 1.8 g/cm^3, respectively. Assuming the particle is spherical, the volume per particle ($V_{particle}$) is given by:

$$V_{particle} = \frac{1}{6}\pi D^3 = 6.06\times10^{-12}\ cm^3 \qquad \text{(B1.2)}$$

Using the density, the mass per particle ($W_{particle}$) can also be estimated as:

$$W_{particle} = V_{particle}\times \rho = 1.09\times10^{-12}\ g/particle \qquad \text{(B1.3)}$$

The mass magnetization at 100 Oe ($\sigma_{s,100\ Oe}$, emu/g) for Dynabeads, determined by our VSM, is 6.21. Therefore, the $\boldsymbol{m}_{particle}$ of Dynabead at 100 Oe can be obtained by multiplying $W_{particle}$ and $\sigma_{s,100\ Oe}$:

$$\boldsymbol{m}_{particle} = W_{particle}\times\sigma_{s,100Oe} = 6.77\times10^{-12}\ emu/particle \qquad \text{(B1.4)}$$

The values of $\boldsymbol{m}_{particle}$ for the ZFNPs and ZFMBs were estimated in a similar fashion. For the $\boldsymbol{m}_{particle}$ for Turbobeads, the field-dependent magnetization (***M*-*H*** curve) was obtained after the AC demagnetization procedure, due to their magnetic hysteresis.

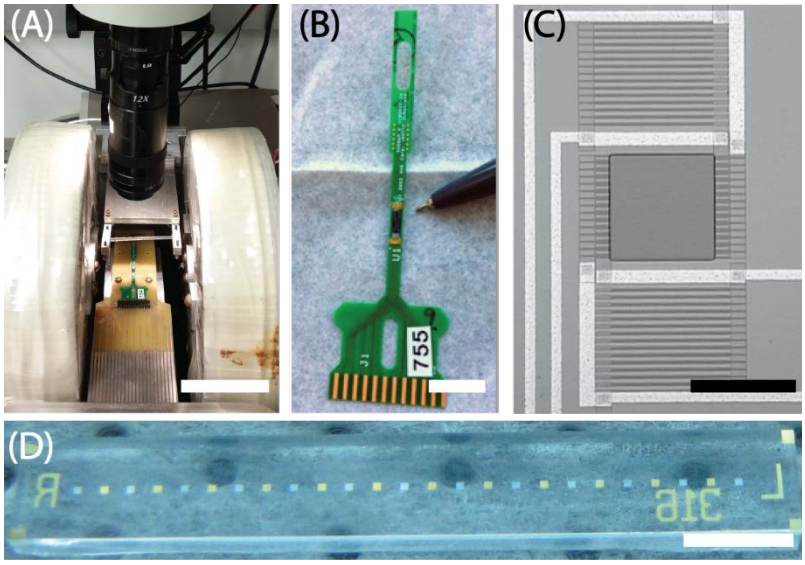

Figure C.1 MR station, MR sensor, and assay substrate. (A) Image of actual MR station. Scale bar is 6 cm. (B) Image of MR sensor mounted on the green PCB board. The ink pen points to the sensor. Scale bar is 1 cm. (C) Image of MR sensor pad. The active sensing area is the square area in the middle. Scale bar is 200 μm. (D) Image of the assay substrate showing alternating nickel and gold addresses. Scale bar is 3 mm.

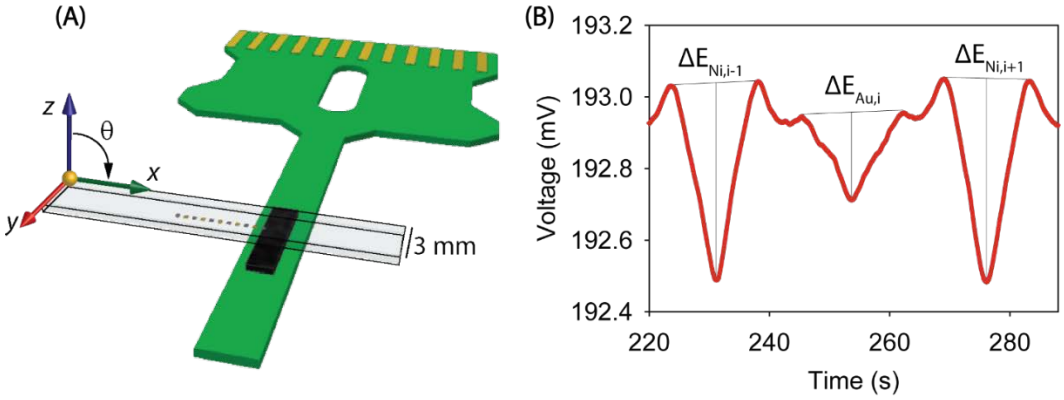

Figure C.2 Schematic illustration of (A) substrate scanning above MR sensor, and (B) MR signal processing.

Table C.1 Calculation of $\boldsymbol{m_{particle}}$.

Particles	$\boldsymbol{m_{particle}}$ **at 100 Oe (emu/particle)**
Dynabeads	6.77×10^{-12}
Turbobeads	2.82×10^{-16}
ZFNP	5.35×10^{-17}
ZFMB	2.36×10^{-13}

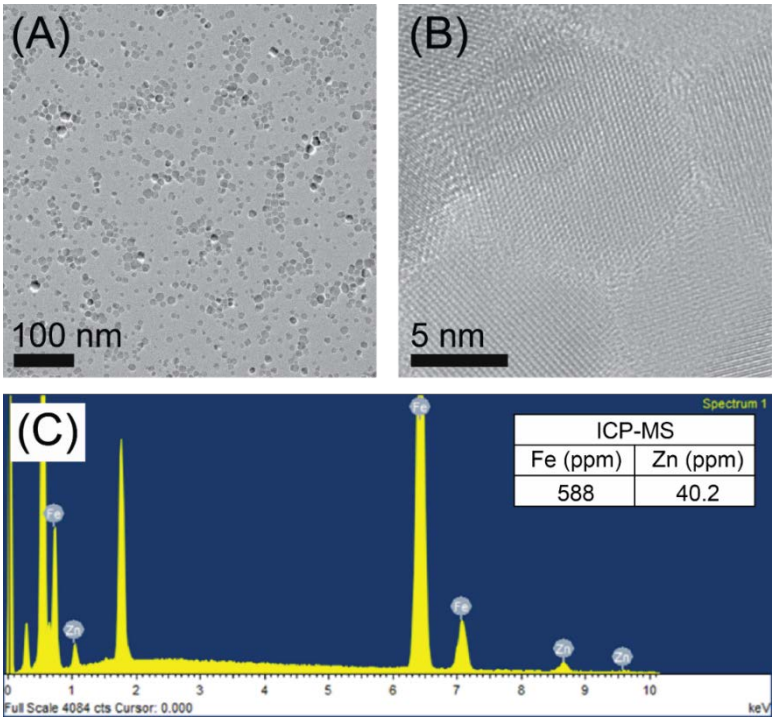

Figure C.3 TEM and elemental analysis of of the as-synthesized ZFNPs. High-resolution TEM image in (B) shows a lattice fringe pattern of the ZFNPs. EDS spectrum clearly shows the presence of Zn in the ZFNPs. The relative molar ratio of Zn to Fe in the as-synthesized ZFNPs, confirmed by inductively coupled plasma mass spectroscopy (ICP-MS), is 5.5:94.5 with 1% precision. This result agrees well with that from the analysis of the EDS data: the atomic ration of Zn/Fe is 4.8/95.2.

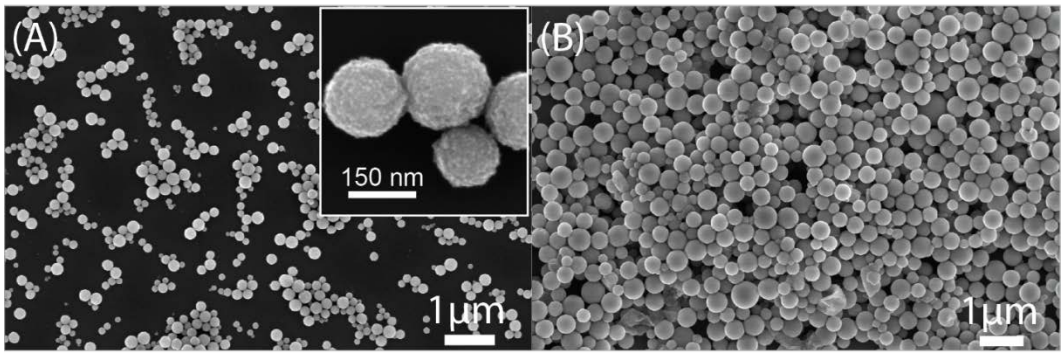

Figure C.4 SEM images of as-synthesized ZFMBs with different sizes. The average diameters of (A) small and (B) large ZFMBs are 163 ± 46 and 378 ± 95 nm, respectively. Note that the average diameter was determined from SEM images by using ImageJ. The inset in (A) is a high-resolution SEM image, showing the distribution of ZFNPs at the surface of ZFMBs.

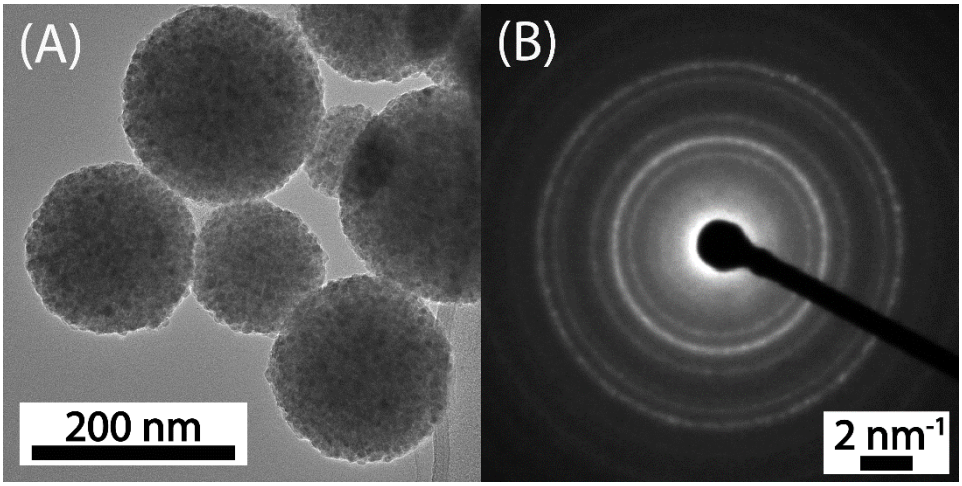

Figure C.5 (A) TEM image and (B) electron diffraction pattern of the as-synthesized ZFMBs. Note that the TEM image (A) was acquired under an objective-lens defocus and that the superlattice fringe pattern with other types of superparticles is not evident in our data.[5-7]

Table C.2 IR peak positions and band assignments of ZFNP and ZFMB particles.

Mode assignment	Description	Band position (cm^{-1})
ν (Fe−O)	ferrite Fe−O lattice vibration	580−590
ν (C=O)	carbonyl stretching in PVP	1631−1664
δ (CH_2)	scissor bending in PVP, PAA, OA	1424−1462
ν (C−N)	carbon nitrogen stretching in PVP	1290
ν_a (COO^-)	asymmetric carboxylate stretching in PAA	1560−1562
ν_s (COO^-)	symmetric carboxylate stretching in PAA	1408−1413
ν (C=O)	carbonyl stretching in PAA	1690−1710
ν_a (CH_2)	asymmetric methylene stretch	2920
ν_s (CH_2)	symmetric methylene stretch	2850

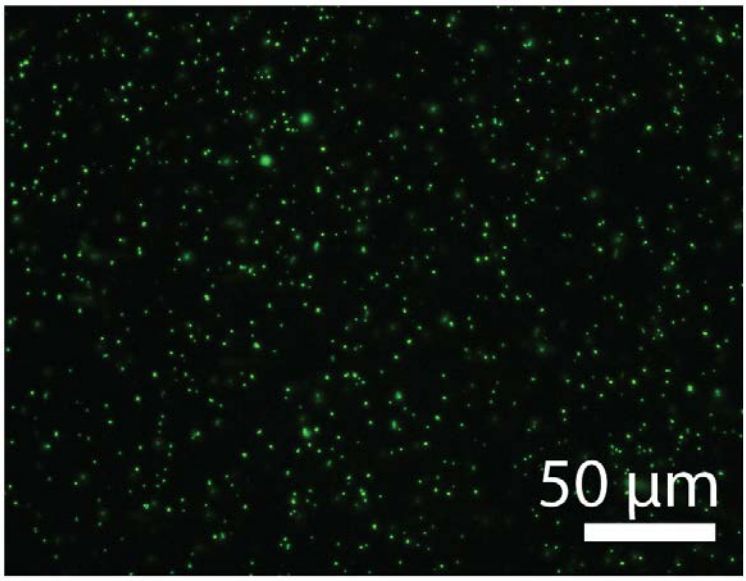

Figure C.6 Fluorescent microscope images of the ZMBs conjugated with fluorescent molecule-tagged avidin (FITC-avidin). Scale bar is 20 µm. FITC-avidin molecules were conjugated to the ZFMBs@PVP@PAA using the same EDC/sulfo-NHS chemistry. A droplet of FITC-avidin conjugated ZFMBs in 5 mM MES (pH 6.5) was sandwiched between a microscope glass slide and a cover slip.

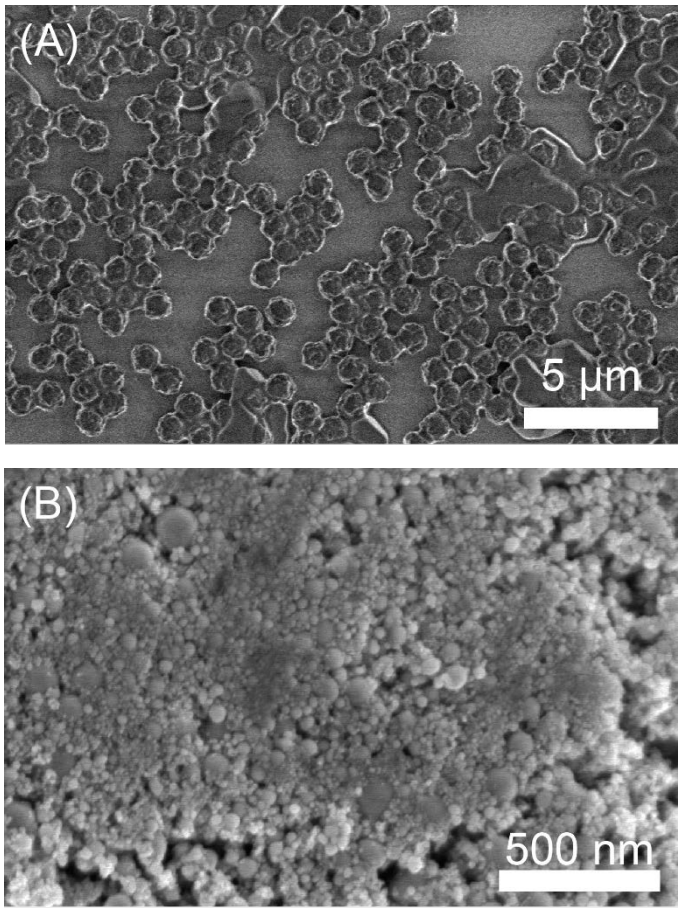

Figure C.7 SEM images of commercially available streptavidinated magnetic beads: (A) Dynabeads and (B) Turbobeads. Dynabeads have a much higher uniformity in size than Turbobeads.

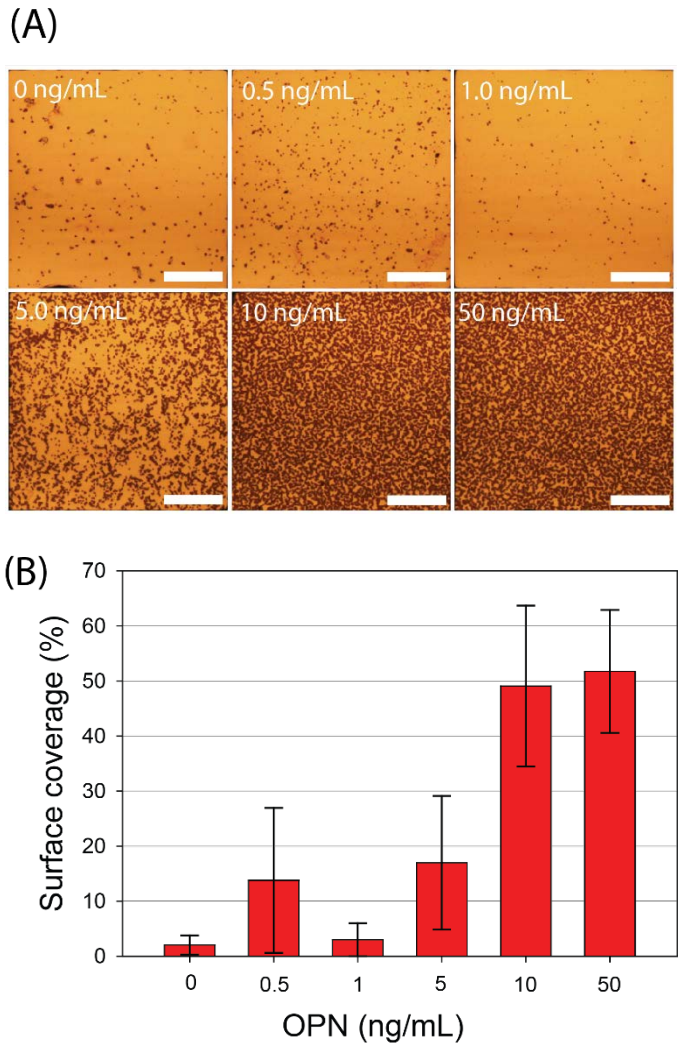

Figure C.8 (A) Representative optical microscope images of gold addresses of OPN assays labeled with Dynabeads. Scale bar is 50 µm. (B) Average surface coverage of the Dynabeads as a function of OPN concentration. The average surface coverage was measured using ImageJ and calculated by averaging 12 gold addresses.

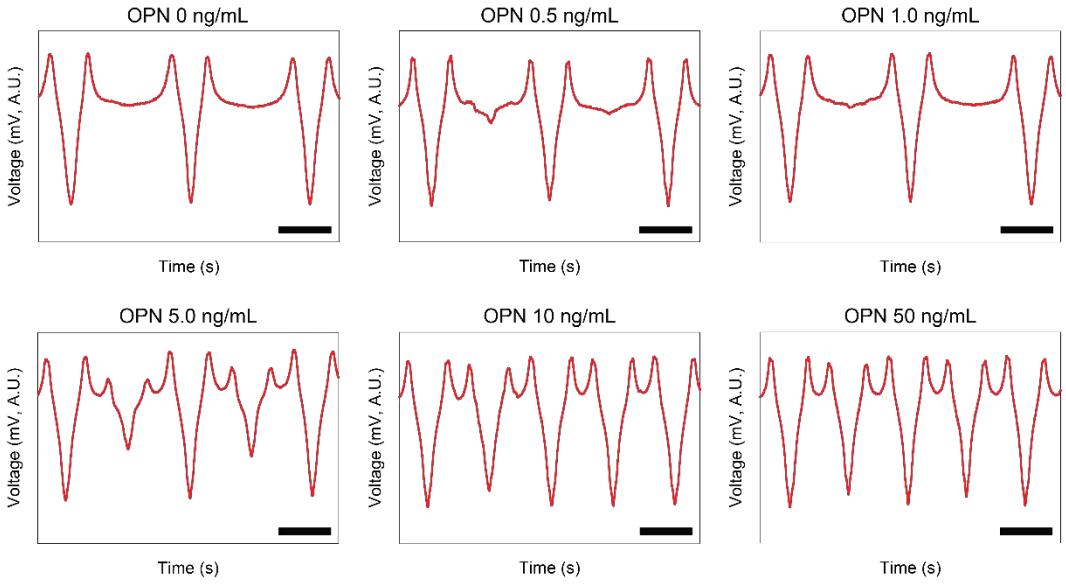

Figure C.9 Representative MR signals of OPN assays labeled with Dynabeads. For simplicity, only two MR signals from gold addresses were plotted. Scale bar is 20 s.

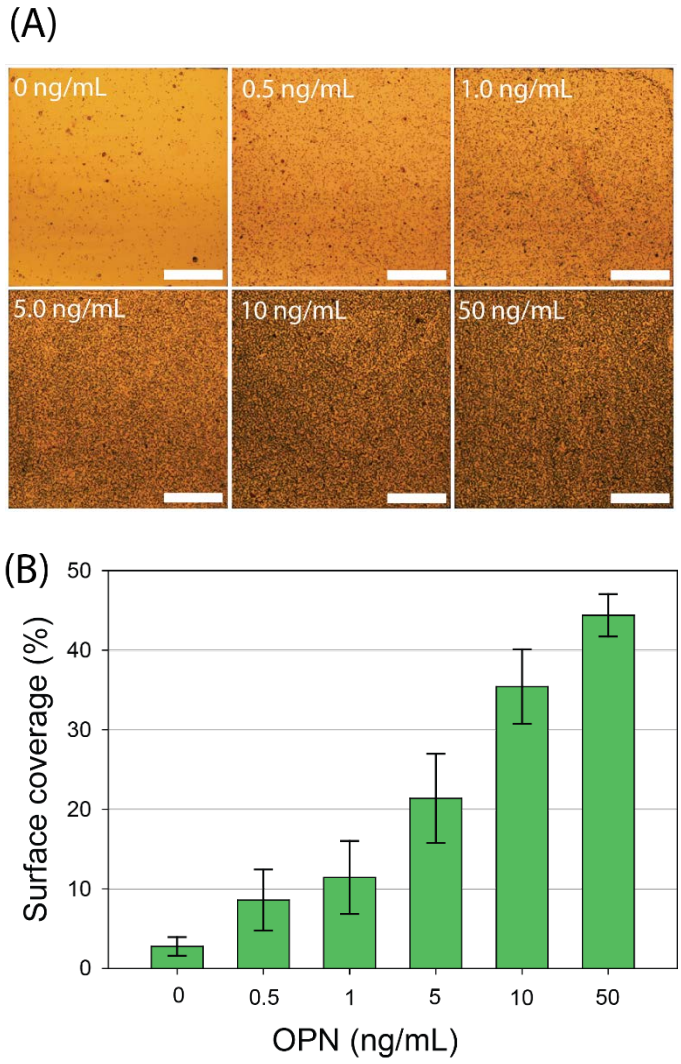

Figure C.10 (A) Representative optical microscope images of gold addresses of OPN assays labeled with the streptavidinated ZFMBs. Scale bar is 50 µm. (B) Average surface coverage of the ZFMB labels as a function of OPN concentration. The average surface coverage was measured using ImageJ and calculated by averaging 12 gold addresses.

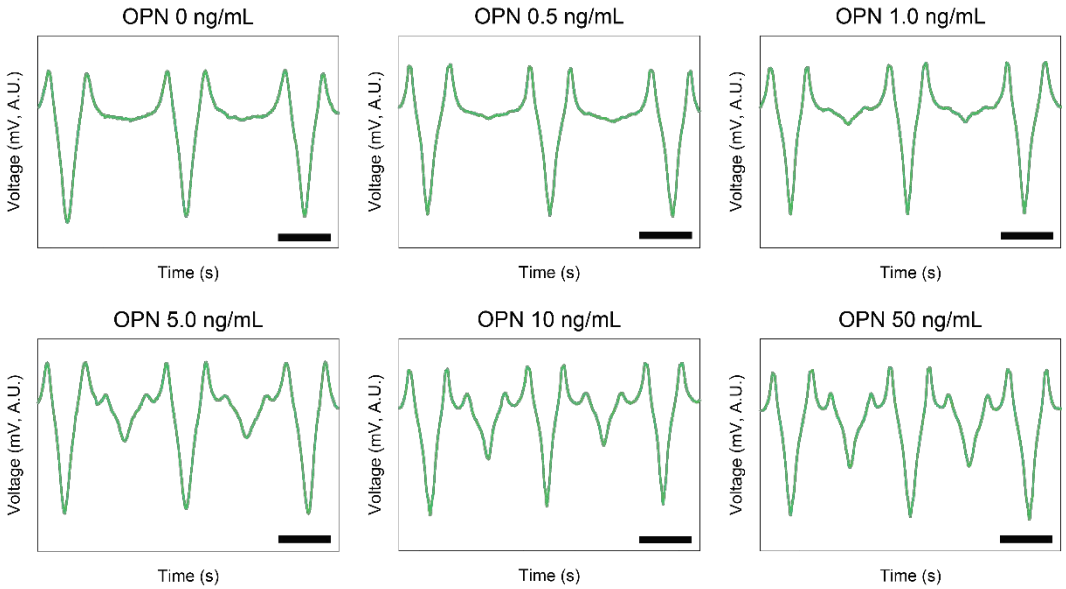

Figure C.11 Representative MR signals of OPN assays labeled with the streptavidinated ZFMBs. For simplicity, only two MR signals from gold addresses were plotted. Scale bar is 20 s.